Tunable Optical Microresonators with Micro-Electro-Mechanical-System (MEMS) Integration

Jin Yao

Electrical Engineering and Computer Sciences
University of California at Berkeley

Technical Report No. UCB/EECS-2007-102

http://www.eecs.berkeley.edu/Pubs/TechRpts/2007/EECS-2007-102.html

August 17, 2007

Tunable Optical Microresonators with Micro-Electro-Mechanical-System (MEMS) Integration

by

Jin Yao

B.Eng. (Tsinghua University) 2000
M.Eng. (Tsinghua University) 2002

A dissertation submitted in partial satisfaction of the

requirements for the degree of

Doctor of Philosophy

in

Engineering – Electrical Engineering and Computer Sciences

and the Designated Emphasis

in

Nanoscale Science and Engineering

in the

Graduate Division

of the

UNIVERSITY of CALIFORNIA, BERKELEY

Committee in charge:

Professor Ming C. Wu, Chair
Professor Constance Chang-Hasnain
Professor Xiang Zhang

Fall 2007

The dissertation of Jin Yao is approved:

Professor Ming C. Wu, Chair　　　　Date

Professor Constance Chang-Hasnain　　　　Date

Professor Xiang Zhang　　　　Date

University of California, Berkeley

Fall 2007

Tunable Optical Microresonators with Micro-Electro-Mechanical-System (MEMS) Integration

by Jin Yao

ABSTRACT

Tunable Optical Microresonators with Micro-Electro-Mechanical-System (MEMS) Integration

by

Jin Yao

Doctor of Philosophy in Engineering – Electrical Engineering and Computer Sciences

and the Designated Emphasis in Nanoscale Science and Engineering

University of California, Berkeley

Professor Ming C. Wu, Chair

Optical microresonators are key enabling elements for many photonic integrated circuits (PICs) areas. Their applications include modulators, optical filters, optical delay lines, nonlinear optical devices, and optical sensors. In previous demonstrations, the coupling of the resonator and its input/output is generally fixed, or tuned using non-integrated alignment system. The ability to control and vary the optical coupling is highly desirable in the areas of emerging adaptive optical circuits as well as in ultra-compact tunable, switchable, and reconfigurable optical components and systems.

In this study, a tunable microresonator achieved by MEMS actuation is proposed on silicon platform. Compared with III-V or II-VI compound semiconductors, silicon has the advantages of low cost, mature fabrication technology, and potential monolithic integration with CMOS devices. Previously, microdisk-based resonators with tunable coupling have been demonstrated. One drawback of the microdisk-based devices is the lack of radial mode control, which could produce additional resonances due to high order

modes. In this research, a novel tunable silicon microtoroidal resonator is proposed and demonstrated for the first time. Microtoroidal resonators offer tighter confinement of the optical mode and eliminate multiple radial modes observed in microdisks. By combining the hydrogen annealing and the wafer bonding processes, very compact and high-Q (quality factor) resonators are monolithically integrated with optical waveguides. The integrated micro-electro-mechanical-system (MEMS) actuators enable the coupling gap spacing to vary from 0 to 1 μm. Use hydrogen assisted surface tension induced annealing, smooth surface is created and high optical performance is attained.

We have achieved an unloaded Q of 110,000 for a 39-μm-diameter resonator with a toroidal radius of 200 nm. The device is able to operate in all three coupling regimes: under-, critical, and over-coupling. The loaded Q is continuously tunable from 110,000 to 5,400. Using this type of microtoroidal resonators we have successfully demonstrated several applications, including bandwidth-tunable filters and add-drop multiplexers. A 21.8 dB extinction ratio is attained for a dynamic add-drop multiplexer. Bandwidth is tuned from 2.8 to 78.4 GHz by voltage control, the highest bandwidth tuning range for this type of filter reported up to date.

The resonators can also be decoupled from the waveguide, enabling them to be cascaded without loading the waveguides. This device can be used as a building block for reconfigurable photonic integrated circuits.

Professor Ming C. Wu, Chair

TABLE OF CONTENTS

LIST OF FIGURES

LIST OF TABLES

ACKNOWLEDGEMENT

I would like to firstly thank my advisor, Professor Ming Wu, for his great guidance and mentoring throughout the whole period of my PhD life. His encouragement and faith in my abilities have inspired me in both academic activities and daily life. Without his guidance, this work would not have come to fruition. I would also like to show my gratitude to other committee members, Professor Constance Chang-Hasnain, and Professor Xiang Zhang for evaluating this dissertation and their support during my PhD study.

I would like to thank the other members of the Integrated Photonics Lab for their discussion and input in all kinds of occasions through my PhD study. Specifically, I would like to thank Prof. Ming-chang Lee, Dr. Sagi Mathai, Dr. David Leuenberger for hands-on experimental training, valuable brainstorming and sparkling discussion. In addition, I would like to thank Ming-Chun Tien, Erwin Lau, Hyuk-kee Sung, Makoto Fujino, Kihun Jeong, Li Fan, Aaron Ohta, Peiyu Chiou, Ted Tsai, Wibool Piyawattanametha, Dooyoung Hah, Hung Nugyen, Josh Chi, Chenlu Hou, Tony Hsu, Arash Jamshidi, Justin Valley and many other group members for many great suggestions and instructions on measurement setups, processing and cleanroom equipments tips and recipes.

I am also very grateful and delighted that I have a very close day-to-day collaboration with Prof. Constance Chang-Hasnain's group. I would like to thank Mike Huang, Xiaoxue Zhao, Elaine Wang, Linus Chuang, Ye Zhou, Bala Pasala, Michael Moewe and other Chang-Hasnain group members for inspiring discussions and help on the experiments.

I have been working in several micro- and nano-fabrication facilities; I am obligated to thank many of the staff members being my wafer savers or life savers in UC Berkeley, Stanford and UCLA cleanrooms. Especially, I would like to thank Mr. Maurice Stevens, Ms. Mahnaz Mansourpour, and Dr. Xiaofan Meng. Their skills and experiences in and out of the lab have been always impressive and beneficial to all the lab members.

On more personal grounds, I would like to thank my beloved wife, and my family, for putting up with my stress and support me endlessly and whole-heartily.

Chapter 1 Introduction

1.1 Introduction to Optical Microresonators

In many aspects of the modern integrated photonic applications, optical microresonators have played an important role and have been continuously investigated as enabling building blocks. They can be utilized to realize many optical functions in terms of generation, amplification, switching, multiplexing/demultiplexing, reshaping, and detection of optical waves on a single chip.

Figure 1.1 has illustrated an optical microresonator in terms of general physical structures. Essentially an optical microresonator is an optical cavity that resonates at some specific wavelengths. These wavelengths are defined as resonant wavelengths. The optical microresonator can be in the form of microsphere, microdisk, microring, microtoroid, or other types of optical micro-cavities. As shown in Figure 1.1, when properly excited, optical waves can propagate to circulate around the periphery of the circular cavity made with high index materials. Optical waves are coupled evanescently to the resonator through optical waveguides.

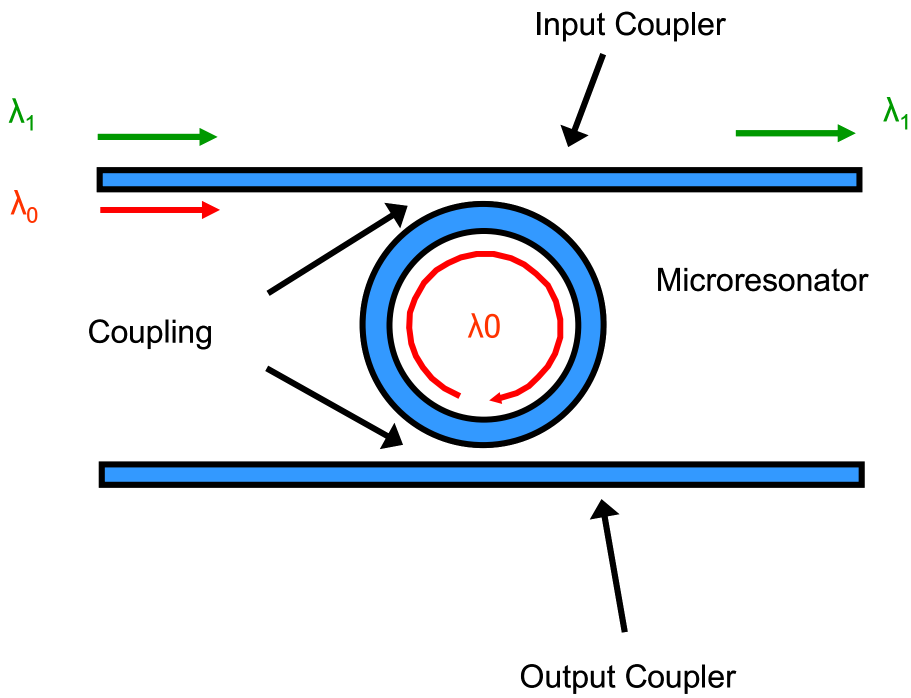

Figure 1.1 Schematic view of an optical microresonator and its input and output couplers. λ_0 represents one of the resonant wavelengths, λ_1 represents one of the non-resonant wavelengths, which directly propagate through the input coupler with no energy coupling into the microresonator.

The optical characteristics of the optical microresonator are similar to that of a Fabry-Perot optical resonator. As shown in Figure 1.2(a), a Fabry-Perot optical resonator is illustrated as a standing-wave resonant cavity formed by two parallel reflecting mirrors separated by media such as air or dielectric materials. Similar to the aforementioned traveling-wave microresonator, the optical waves resonate at some specific wavelengths when they interfere constructively. There is a one-to-one correspondence between the microresonator and the Fabry-Perot cavity. Figure 1.2(b) shows a typical spectrum of the optical microresonator within one free spectral range (FSR).

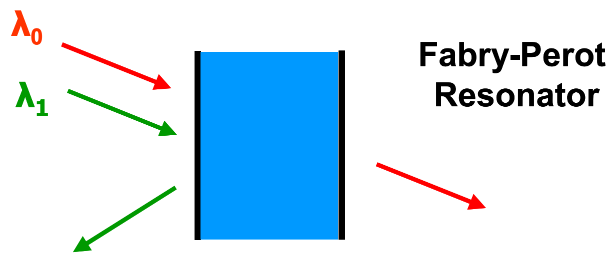

(a)

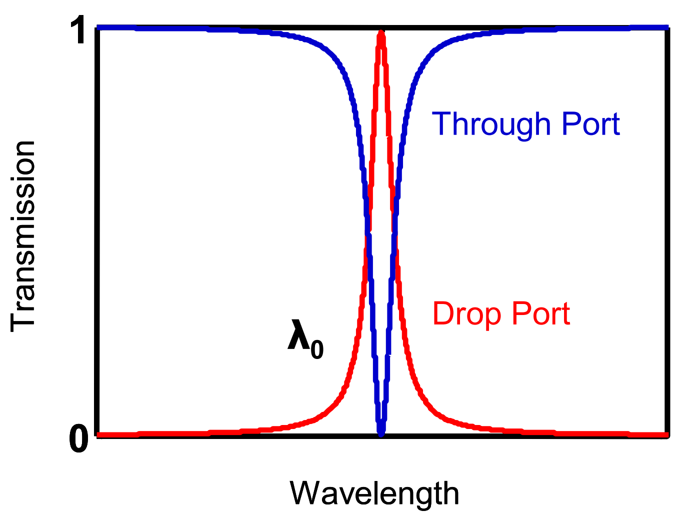

(b)

Figure 1.2 (a) Schematic of a Fabry-Perot resonator. (b) Typical spectrum of the optical microresonator within one free spectral range (FSR). Here λ_0 represents one of the resonant wavelengths, λ_1 represents one of the non-resonant wavelengths.

1.2 Optical Microresonator Applications

In many modern photonic integrated applications, microresonators have continuously drawn much attention as enabling building blocks because of their performance, compact size, scalability, and integration compatibility with planar optical circuits.

Various optical components such as compact optical filters [1-5], optical modulators [6-9], add-drop multiplexers [3], optical dispersion compensators [10-12] and delay lines [13, 14], nonlinear optical devices [15] and Quantum Electrodynamics (QED) cavities [16, 17], and optical sensors [18, 19], have been demonstrated. Using active microresonators as cavities, compact laser sources have also be realized [20-22].

The applications listed here are only a selected group of the many application aspects in which microresonators have been used. Thanks to recent advances of integrated optical and electronic circuits, silicon-based microresonators have been an active research area. With high refractive index, silicon provides tight optical confinement necessary for high-density optoelectronic integration and nonlinear optics. Extremely compact optical components [23, 24] and low-power nonlinear phenomena have been demonstrated [15].

Compared with compound semiconductors [20, 22] or glass-based planar lightwave circuits (PLCs) [25, 26], silicon offers the advantages of low cost, mature fabrication technology and potential monolithic integration with complementary metal-oxide-semiconductor (CMOS) devices. In addition, silicon-on-insulator (SOI) wafers widely used in electronic integrated circuits also provide an ideal platform for optical and optoelectronic integrated circuits. The underlying thermal oxide provides simultaneous high-quality optical and electrical isolation. In this dissertation, effort will be mainly focused on silicon-based microresonator investigation.

1.3 Tuning of Optical Microresonators

The performance of optical microresonators mainly depends on three parameters: resonator loss, coupling ratio between the resonator and the waveguides, and resonant wavelengths. The resonator loss depends on the optical power dissipation in the resonator cavity. The resonant wavelength is determined by the refractive index and the optical path length of the cavity. And the coupling ratio depends on how the energy transfers through the evanescent fields between the coupler and the microresonator. Detailed parametric modeling will be discussed in the following chapter of this dissertation.

Altering any of the three parameters can change the microresonator properties. Tuning the resonator loss or coupling ratio can vary the transmission power and bandwidth. Tuning the resonant wavelengths shifts the transmission spectrum. These tuning properties are illustrated in Figure 1.3. With the increasing demand of dynamic optical devices and systems, tunability is desirable for reconfigurable wavelength-division-multiplexing (WDM) networks.

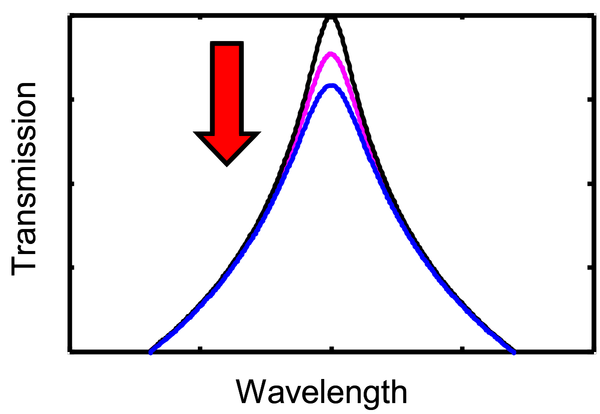

(a)

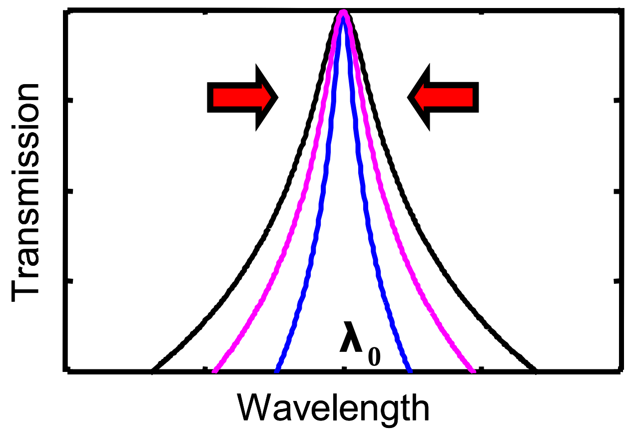

(b)

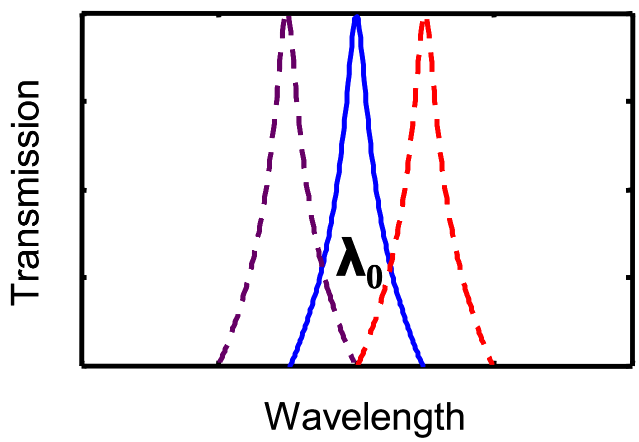

(c)

Figure 1.3 The transmission spectra of the microresonator with (a) tunable resonator loss, (b) tunable coupling ratio, and (c) tunable resonant wavelength. Tuning the resonator loss or coupling ratio varies the transmission intensity and transmission bandwidth. Tuning the resonant wavelengths shifts the transmission spectrum.

1.3.2 Tuning of Resonant Wavelengths and Resonator Loss

Most of the tuning mechanisms reported in literature focused on varying the resonant wavelengths and the resonator loss. The resonant wavelength can be tuned by changing refractive index through local heating [27-29], electro-optical effect [30], or electrical carrier injection [31, 32]. It can also be tuned by direct change of cavity length with applied strain [17, 33, 34].

These devices have applications in tunable filters. The resonator loss can be controlled by attaching a lossy metal to spoil the Q to achieve switching function [35]. In III-V compound microresonator systems, resonator loss can also be tuned by electroabsorption [36] and gain trimming [37, 38]. The loss tuning generally can be used in applications for reconfigurable optical add-drop multiplexers and switches.

1.3.3 Tuning of Resonator Coupling Ratio

Most of the microfabricated resonators reported to date have fixed power coupling ratios. In microresonators with integrated waveguides, the coupling ratio is determined by the fabrication process [39]. The value of coupling ratio, or perhaps more importantly, its relation with the resonator cavity loss, cannot be controlled precisely. Some trimming processes have been proposed to control the resonance frequency but not coupling ratio [40, 41].

However, it is always desirable to precisely control the coupling ratio to achieve optimum performance [42]. During early studies, prism couplers with frustrated total internal reflection were the main methods to couple light in and out of optical resonators. Prism coupling to resonator modes were studied and demonstrated in [43-47]. It is shown that efficient coupling requires optimum gap spacing between the prism and the waveguide to control coupling [48, 49]. Prism coupling has been demonstrated with an efficiency of more than 90 percent to waveguides [50, 51] and 80 percent to resonators [45]. By physically moving prism couplers, control of coupling ratio has been achieved in fused silica microsphere resonators [52]. However, prism couplers are not ideal for mode control because of the large number of output modes.

Alternatively, coupling ratio can be controlled by varying the physical gap distance between the fiber-based coupler and the optical resonator. Side-polished fiber couplers have limited efficiency due to residual phase mismatch [53-55]. Pigtailed couplers using angle-polished tapered fiber tips can adjust the coupling through total internal reflection [56], thus achieving up to almost 100% coupling [57-60]. With piezo-controlled micropositioners, moving tapered fiber couplers have also achieved excellent coupling ratio control. [57, 58, 61]. However, both the prism and the tapered fiber coupling setups are bulky and not easily integratable.

Recently, control of the coupling ratios of microresonators in integrated system have been reported [62-64]. A Mach-Zehnder interferometer (MZI) has been integrated with a racetrack resonator [62]. The resonator can operate in all coupling regimes (uncoupled, under-, critical, or over-coupled). An unloaded Q of 1.9×10^4 and an ON-OFF ratio of 18.5 dB have been achieved. However, the circumference of the resonator is as large as 1430 μm due to the long MZI structure, which limits the free spectral range and the smallest footprint it can achieve. Microfluidic approach has also been employed to tune both the resonance wavelength and the coupling ratio of low-index microring resonators made in SU8 [65]. The refractive index of the surrounding media was varied by mixing two different liquids. Critical coupling with an extinction ratio of 37 dB have been attained. However, index variation is small (~ 0.04), which limits the tuning range of the coupling ratio. In addition, and the tuning speed is slow (~ 2 sec) and the fluidic packaging is cumbersome.

With the advances in fabrication technologies, mechanical actuation has become a viable and effective means to control the gap spacing between the microresonator and the waveguide coupler. Micro-electro-mechanical system (MEMS) has been showing to be one of the key enabling technologies for dynamically tunable optical components. Using MEMS technology, many applications employing mechanical actuation for optical control have been demonstrated [66], including micromirror switches [67-72], MEMS scanning mirrors [73], optical scanners [74-76], as well as the projectors with digital micromirror device (DMD). MEMS-actuated optical coupling has been demonstrated utilizing either evanescent coupling [77] or butt coupling [78] of waveguides. In a high-index-contrast silicon-based microresonator with sub-micron waveguide coupler, the coupling coefficient can be varied over many orders of magnitude by changing the physical gap distance within less than 1 μm [64].

MEMS actuation can control the gap spacing precisely. The device has a small footprint, and can be monolithically integrated. Compared with the tuning mechanism using current injection, MEMS actuation with electrostatic actuation mechanism has much lower power consumption and a larger tuning range.

1.4 Organization of Dissertation

Motivated by the benefits of silicon-based platform, and integrated controllability via MEMS technology, in this dissertation we have investigated the design, simulation, experimental demonstration of silicon-based tunable optical microresonators and their applications.

In Chapter 2, we first introduce a generic model of the optical microresonators and discuss the important parameters. We then analyze the optical modes in the microresonator and the waveguide coupler. In Chapter 3, we explain the limitations of microdisk resonators, and introduce a new microtoroidal resonator. Detailed design and theoretical analysis of the new device will be described. With the design, in Chapter 4 we talk about the device fabrication challenges and how we optimize the process flow to realize the integrated device. In Chapter 5, we characterize the microresonator devices, and establish a model to extract critical device parameters. In Chapter 6, we show the experimental data of high performance devices for a variety of applications, and compare experiments with the theory. Chapter 7 summarizes our work in this dissertation. The appendices provide the supporting program scripts and the detailed process that were used for design, analysis, and process optimization in this dissertation.

Chapter 2 Theory of Optical Microresonators

2.1 Parametric Modeling of Microresonators

Generally optical microresonators can have cylindrical, spherical, spheroidal, toroidal, ring, and other shapes and topologies to form the optical cavity. Propagating waves are coupled in or out of the optical resonator through optical couplers. The optical waves circulate around the periphery of the resonator cavity by total internal reflection. A generic optical microresonator can be mainly characterized by three parameters: resonant wavelength (denoted as λ_0), power coupling ratio (denoted as κ), and resonator loss (denoted as α). A schematic of the microresonator model is shown in Figure 2.1.

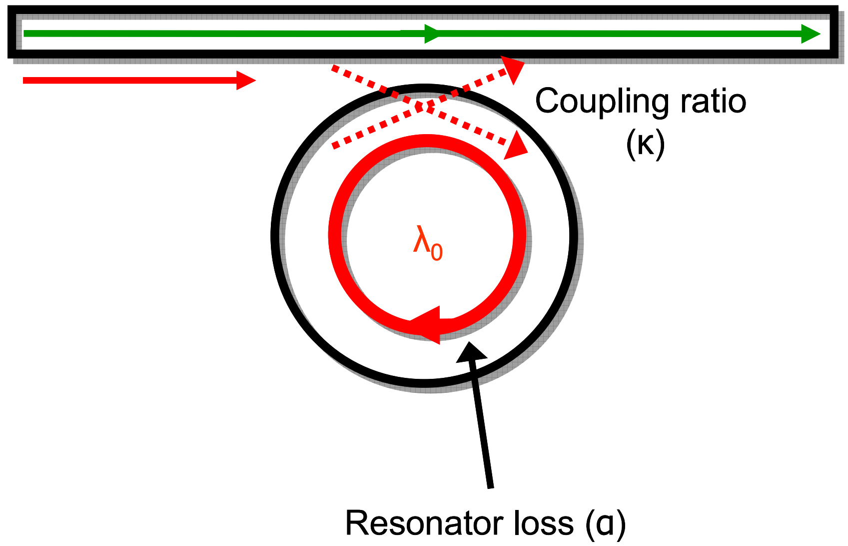

Figure 2.1 Schematic of the microresonator with the key parameters: λ_0 is one of the resonant wavelengths, κ is the power coupling ratio between the waveguide and microresonator, and α is the resonator loss.

The resonant wavelength λ_0 is determined by the optical path length inside the cavity. λ_0 can be tuned by either changing the index of refraction of the microresonator via local heating [27-29], or electrical carrier injection [31, 32], or the physical length of the cavity [17, 33, 34]. The power coupling ratio κ is the percentage of power transferred from the waveguide coupler to the microresonator. In this dissertation, power coupling ratio is also describe as coupling ratio. The power coupling ratio is determined by the coupler and gap geometry. Similar to waveguide-to-waveguide coupling, κ can be derived using coupled mode theory based on the geometry and the index distribution [64, 79]. Resonator loss, α, represents the power dissipation rate inside the microresonator. It plays a critical role in the optical properties of the resonator. Equivalently, the resonator loss α can be represented by another parameter: quality factor (Q), which is also commonly used to describe the characteristics of optical resonators.

These parameters are important to target the appropriate wavelength range, to realize expected optical performance, and to achieve tunable functions. In chapter 1, we have qualitatively described these parameters; detailed analysis will be expanded in a later section of this dissertation.

2.2 Analysis of Whispering Gallery Modes of the Microresonators

To better understand the properties of microresonators and to model their performance, in this chapter we first analyze the optical modes of the microresonators and the couplers.

As illustrated in the previous sections, the optical wave propagating inside the microresonator is combined with the optical wave coupled from the input waveguide. At resonance, they interference constructively, and form a particulate intensity pattern, or a resonant mode. This resonant mode is called a whispering gallery mode (WGM).

The study of whispering-gallery modes was firstly introduced around a century ago by Lord Rayleigh, who studied the propagation of sound over the cylindrical wall in St. Paul's Cathedral, London [80, 81]. Previously, WGMs of microwave resonances in dielectric spheres were firstly investigated [82, 83]. The first observations of WGMs in optics were in the studies for solid-state WGM lasers [84]. The size of the resonators was in the millimeter range. For theoretical investigation of the WGMs, Debye first derived equations for the resonant eigenfrequencies of free dielectric and metallic spheres in 1909 [85]. The mode profile in a circular dielectric rod was derived by Wait and it was indicated that the energy is mainly confined to the region near the boundary [86]. This model is based on an infinite dielectric circular cylinder. Using effective index method, microresonators with finite slab thicknesses can be modeled as cylinders and will be analyzed here.

Figure 2.2 shows the schematic model of a microresonator with the parameters for WGM analysis. In this plot, a represents the radius of the microresonator, t is the slab thickness. n_1 and n_2 are effective indices of refraction of the microresonator and the surrounding medium, respectively. n_1 can be determined by the index of refraction of the microresonator and the thickness t. n_2 can be 1 if surrounding medium is air.

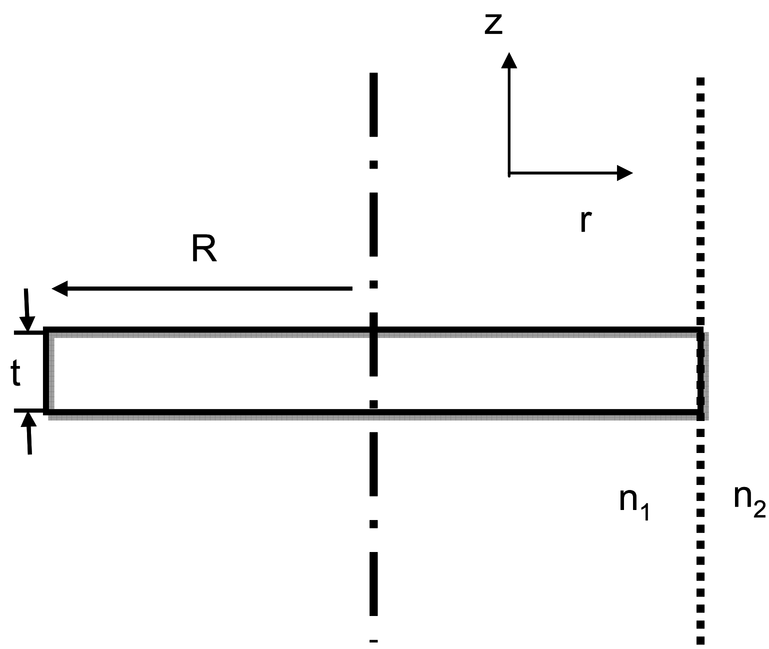

Figure 2.2 Cross section view of the schematic microresonator model for WGM analysis with the parameters. a represents the radius of the microresonator, t represent the slab thickness. n1 and n2 are effective indices of refraction of the microresonator and air, respectively.

The mode with the polarization of the electric field parallel to the radial direction is defined as TE mode; the one with the polarization perpendicular to it is defined as TM mode. The fields for the TE and TM mode are expressed as [87, 88].

$$\Psi_I = C \cdot \cos(hz) \cdot J_l(I_{lm} \cdot \frac{r}{R}) \cdot e^{jl\phi} \cdot e^{j\omega t} \tag{2.1}$$

when r < R; and

$$\Psi_O = C \cdot \cos(hz) \cdot H_l^{(2)}(O_{lm} \cdot \frac{r}{R}) \cdot e^{jl\phi} \cdot e^{j\omega t} \tag{2.2}$$

when r > R. Where J_l and $H_l^{(2)}$ are Bessel and Hankel functions of the first and second kind, respectively, *m* is the radial mode number, *l* is the azimuthal mode number. h, I_{lm}, Q_{lm} above are all wave vectors as in

$$\begin{aligned}
V &= \frac{2\pi R}{\lambda}\sqrt{(n_1^2 - n_2^2)} \\
\Delta &= \frac{n_1^2 - n_2^2}{n_1^2} \\
h &= \frac{1}{R}\sqrt{\frac{V^2}{\Delta} - I_{lm}^2} \\
V^2 &= I_{lm}^2 + O_{lm}^2
\end{aligned} \tag{2.3}$$

In the z-direction, we can design the thickness t so that it would only support one guided mode in the z-direction. Using the effective index method, the wave vectors I_{lm} and O_{lm} can be expressed as

$$\begin{aligned}
I_{lm} &= \frac{2\pi R}{\lambda / n_1} = \frac{2\pi R n_1}{\lambda} \\
O_{lm} &= \frac{2\pi R}{\lambda / n_2} = \frac{2\pi R n_2}{\lambda}
\end{aligned} \tag{2.4}$$

where λ_{lm} is the resonant wavelength with azimuthal mode number l and radial mode number m.

The eigenvalue equation for these modes can be transformed to

$$\frac{H_l^{(2)}{}'(O_{lm})}{O_{lm} \cdot H_l^{(2)}(O_{lm})} - n_{eff}^2 \frac{J_l'(I_{lm})}{I_{lm} \cdot J_l'(I_{lm})} = 0 \tag{2.5}$$

for TM mode and

$$\frac{H_l^{(2)}{}'(O_{lm})}{O_{lm} \cdot H_l^{(2)}(O_{lm})} - \frac{J_l{}'(I_{lm})}{I_{lm} \cdot J_l{}'(I_{lm})} = 0 \tag{2.6}$$

for TE mode.

By solving the eigenvalue equations, the field distribution inside and outside the radius of this model can be derived. Here, we first use an initial guessed value for the resonator wavelength. The result is evaluated in Equations (2.5) and (2.6), and iterated until it converged so that the accurate resonant wavelengths are calculated.

It is noted that for each eigenfunction with an azimuthal mode number (l), there are multiple solutions λ_{lm} (m = 1, 2 …). m = 1 represents the fundamental radial mode and gives the best mode confinement inside the microresonator, which is generally what we are most interested in.

With the calculated resonant wavelength, the mode profile of each WGM is shown as the following:

$$E_z(r) = \frac{J_l(I_{lm} \cdot \frac{r}{R})}{J_l(I_{lm})} \tag{2.7}$$

when r < R; and

$$E_z(r) = \frac{H_l^{(2)}(O_{lm} \cdot \frac{r}{R})}{H_l^{(2)}(O_{lm})} \tag{2.8}$$

when r > R.

Figure 2.3 plots the fundamental whispering gallery mode profile in the radial direction for a silicon-based microresonator model. It has a radius of 19.5 μm and and a silicon thickness of 250 nm. We focus on resonant wavelengths (λ_0) around 1550 nm range for telecommunication and networking applications. Figure 2.3 shows the electric field intensity for WGMs with the same azimuthal mode number but different radial mode numbers. The fundamental radial mode, the 2nd and the 3rd higher order radial modes are shown here. The number of peaks is proportional to the radial mode number. With the same azimuthal mode number, high-order radial modes have shorter resonant wavelengths.

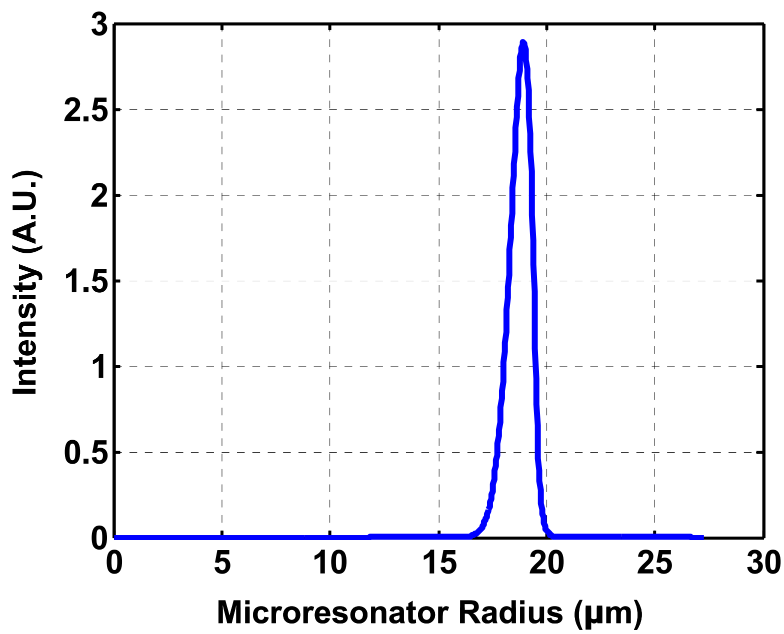

(a)

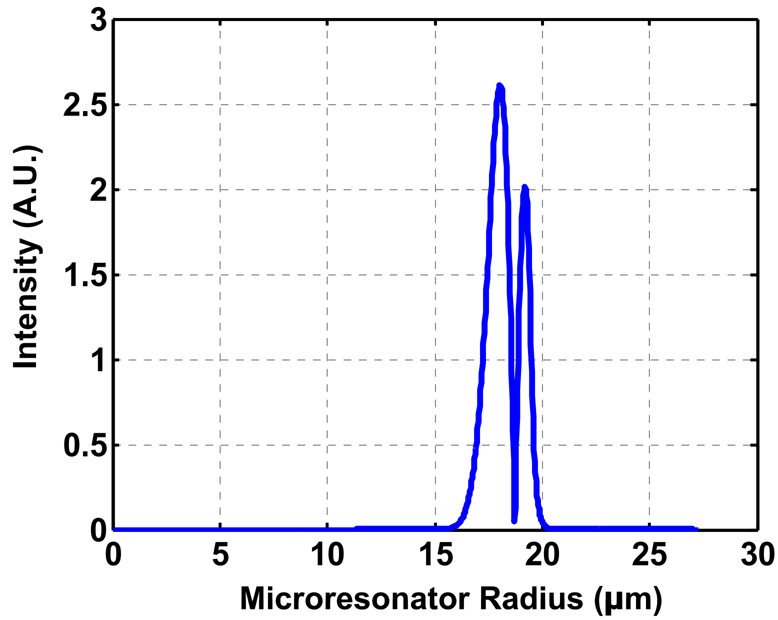

3
2.5
2
1.5
1
0.5
0
Intensity (A.U.)
0
5
10
15
20
25
30
Microresonator Radius (μm)

(b)

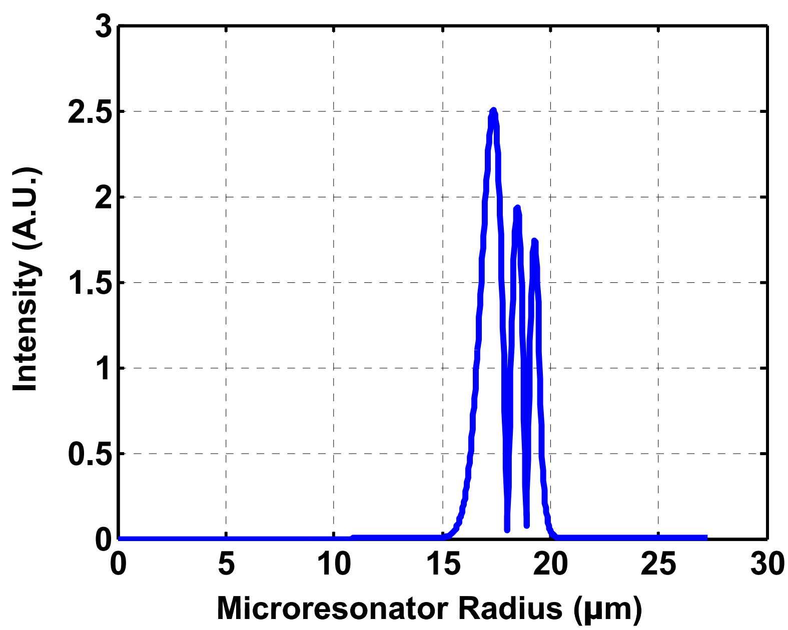

3
2.5
2
1.5
1
0.5
0
Intensity (A.U.)
0
5
10
15
20
25
30
Microresonator Radius (μm)

(c)

Figure 2.3 The calculated WGM profiles in the radial direction for a microresonator with a radius of 19.5 μm. They have the same azimuthal mode number but different radial mode numbers. The azimuthal mode number is 148. (a) Fundamental radial mode (m = 1), (b) 2^{nd} higher radial mode (m = 2), and (c) 3^{rd} higher radial mode (m = 3). The corresponding resonant wavelengths are 1554 nm, 1482 nm, and 1456 nm, respectively.

Based on the approaches to express the optical power of a WGM, the equivalent propagation constant of the WGM, defined as β, can be derived as [25, 88]:

$$\beta = \frac{l \cdot \int_0^{R_{rad}} \frac{E(r)^2}{r} dr}{\int_0^{R_{rad}} E(r)^2 dr} \tag{2.9}$$

where R_{rad} is the location at which the power leaks to the air, defined as the radiation caustic [88]. Using this method, this key parameter propagation constant β can be obtained. β is important for phase matching design between the microresonator and the coupler, which will be discussed later.

Though the analytical model is based on an ideal dielectric cylinder with rectangular cross section, it can be extended to analyze other microresonators such as microdisks, microrings, and microtoroids with modified boundary conditions.

For more sophisticated boundary conditions, Finite-difference-time-domain (FDTD) and other numerical methods [89] have been used to analyze the WGMs. A detailed example of using computed-aided simulation based on beam propagation method (BPM) [90] to obtain the microtoroid type of microresonators will be described later.

2.3 Analysis of Waveguide Coupler Modes

Phase matching with the waveguide coupler is important to achieve efficient power transfer. Phase matching conditions are met when two waveguides have the same propagation constant. In this section, we analyze the optical modes of the waveguide coupler.

Both rib waveguides and channel waveguides are commonly used to achieve single mode operation. Rib waveguides can sustain a large modal profile to minimize insertion loss [91]. However, because effective refractive index of a rib waveguide is typically much higher than that of silicon microresonators, phase matching condition between the rib waveguide and the microring can not be satisfied. Thus here we only consider channel waveguides.

The cross section of a channel waveguide is shown in Figure 2.4 . The waveguide width and thickness are denoted by *2a* and *2d*, respectively. The waveguide medium has a refractive index n_1, and has cladding medium around with a refractive index of n_0. To simplify the model, Marcatili's approximation is used to ignore light in the shaded regions at the corners of the crystalline Si [25, 92]. The crystalline Si core with a refractive index of 3.46 is the guiding region where most of the optical field is confined. The cladding in our case is assumed to be air with refractive index of 1. Small amount of light penetrates into the cladding region of lower index of refraction, where the field intensity decays exponentially.

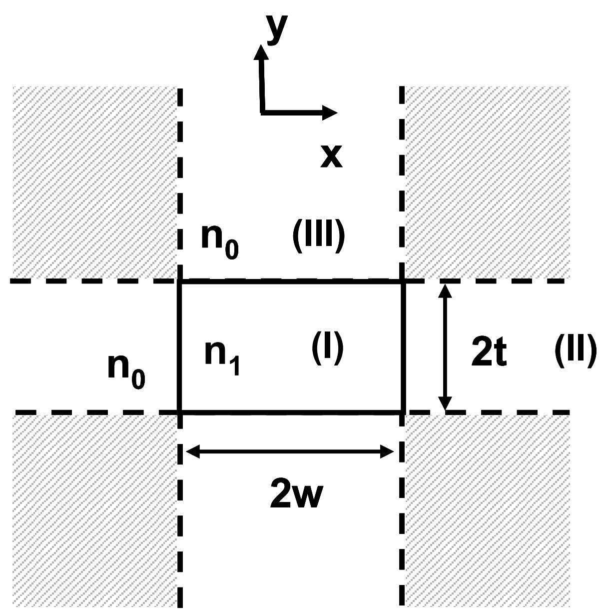

Figure 2.4 Cross-sectional profile of a channel waveguide. The waveguide core has a refractive index n_1, and the cladding region has a refractive index of n_0.

The electric field of the channel waveguide is defined to be either TE-polarized with the electric field E parallel to the x direction or TM-polarized with E parallel to the y direction. Here we use TE polarization as an example to expand the analysis. Based on Marcatili's model, the x-component of the magnetic field is equal to zero for TE polarization (i.e. $H_x = 0$). Then the optical wave field equation can be expressed as:

$$\frac{\partial^2 H_y}{\partial x^2} + \frac{\partial^2 H_y}{\partial y^2} + (k^2 n^2 - \beta^2) H_y = 0 \tag{2.10}$$

where the field components are:

$$
\begin{aligned}
H_x &= 0 \\
E_x &= \omega \frac{\mu_0}{\beta} H_y + \frac{1}{\omega \varepsilon_0 n^2 \beta} \cdot \frac{\partial^2 H_y}{\partial x^2} \\
E_y &= \frac{1}{\omega \varepsilon_0 n^2 \beta} \cdot \frac{\partial^2 H_y}{\partial x \partial y} \\
E_z &= \frac{1}{j \omega \varepsilon_0 n^2} \cdot \frac{\partial H_y}{\partial x} \\
H_z &= \frac{1}{j\beta} \cdot \frac{\partial H_y}{\partial y}
\end{aligned}
\tag{2.11}
$$

where n is the refractive index, k is the free-space wavenumber, β is the propagation constant, ω is the optical frequency, and ε_0 and μ_0 are the permittivity and permeability, respectively. The y-component of the magnetic field at different regions can be expressed as:

$$
H_y = \begin{cases} C\cos(k_x x)\cos(k_y y) & (I) \\ C\cos(k_x w)\cos(k_y y)\exp[-\gamma_x (x-w)] & (II) \\ C\cos(k_x x)\cos(k_y t)\exp[-\gamma_y (y-t)] & (III) \end{cases}
\tag{2.12}
$$

where k_x, k_y, γ_x, and γ_y are the transverse wave numbers for regions indicated as (I) (II) and (III) in Figure 2.4.

Applying the boundary conditions that the electric field E_z should be continuous at $x = w$, and the magnetic field Hz should be continuous at $y = t$, we can obtain the transcendental equations for the eigenvalues:

$$
\begin{aligned}
k_x w &= \tan^{-1}\left(\frac{n_1^{\,2}\gamma_x}{n_0^{\,2} k_x}\right) \\
k_y t &= \tan^{-1}\left(\frac{\gamma_y}{k_y}\right)
\end{aligned}
\tag{2.13}
$$

In Equation (2.13) we are interested in the fundamental mode of the waveguide.

The propagation constant β is related to the transverse wavenumbers in the above equations through following relations:

$$\begin{cases} \beta^2 = k^2 n_1^{\ 2} - (k_x^{\ 2} + k_y^{\ 2}) \\ \gamma_x^{\ 2} = k^2 (n_1^{\ 2} - n_0^{\ 2}) - k_x^{\ 2} \\ \gamma_y^{\ 2} = k^2 (n_1^{\ 2} - n_0^{\ 2}) - k_y^{\ 2} \end{cases} \tag{2.14}$$

From the above equations, β can be calculated for TE and TM modes by solving for k_x and k_y. Figure 2.5 displays the calculated propagation constants versus wavelength for TE mode of the silicon channel waveguide for various waveguide thickness t. The waveguide width is assumed to be 0.69 μm.

Having established the method to calculate the propagation constants with given waveguide dimensions, the design now is to select a set of waveguide dimensions that renders its fundamental mode phase-matched to the fundamental WGM of the microresonator.

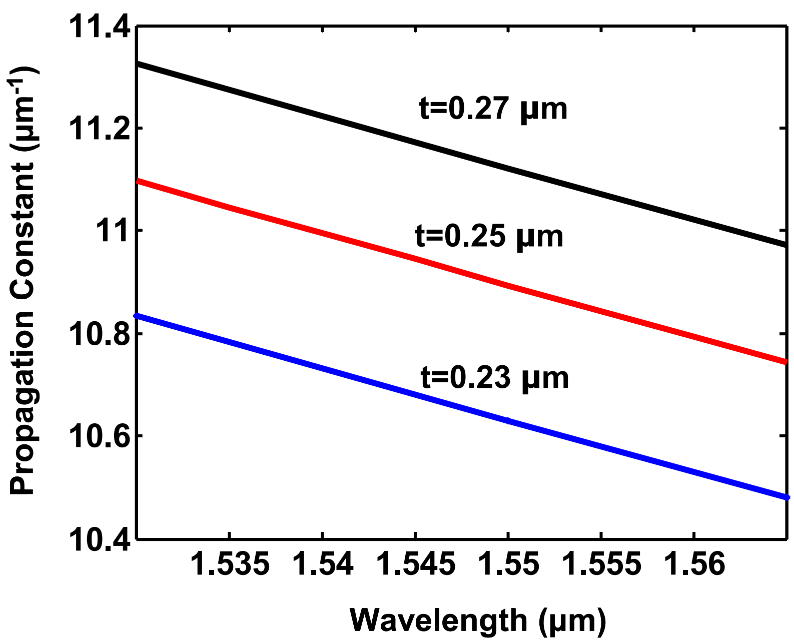

Figure 2.5 The calculated propagation constants versus wavelength for the TE mode of the silicon channel waveguide TE mode for various waveguide thickness t. The waveguide width is assumed to be 0.69 μm.

2.4 Quality Factor and Microresonator Loss

The definition of quality factor extends well beyond the boundary of integrated photonics and is generally defined for all resonant elements. A simple definition of quality factor (Q) is the ratio of the total energy in a system to the energy lost per cycle. The Quality factor can be expressed as

$$Q = \omega_0 \cdot \tau = \frac{\omega_0}{\Delta\omega} \tag{2.15}$$

where ω_0 is the resonant frequency and τ is the decay time of energy stored in the resonator, $\Delta\omega$ is the resonator bandwidth. Because Q represents the loss performance, high Q value is desirable for achieving narrowband filtering, nonlinear and cavity QED effects, as well as low threshold microlaser sources [93].

The loss in the resonator mainly comes from two categories: one is waveguide coupling and the other is intrinsic loss of the resonator. Q can be further decomposed to

$$\frac{1}{Q} = \frac{1}{Q_i} + \frac{1}{Q_e} \tag{2.16}$$

where the Q_e represents the quality factor due to waveguide coupling, and Q_i, the unloaded Q, represents the quality factor due to intrinsic loss. In general, Q_e is affected by the waveguide to microresonator power coupling ratio; and Q_i is determined by the power dissipation in the microresonator [94]. The resonator intrinsic loss primarily results from material loss, bending loss, scattering loss, and two-photon absorption loss, etc.

In terms of material loss, as light propagates in high-conductivity media, it can interact with free carriers such as electrons that can cause optical loss. Minimizing the doping level in silicon is required to achieve low propagation loss. The relation between free carrier density and propagation loss was reported by Soref [95]. To achieve an unloaded Q greater than 10^8, the free carrier density should be less than 10^{14}, which corresponds to a resistivity of 10 Ω-cm for n-type dopants. The resistivity of common electronic silicon wafers ranges from 0.01 Ω-cm to 100 Ω-cm.

Bending loss is one of the general concerns for microresonators as well as waveguides [96]. Strictly speaking, all the WGMs are leaky modes [47]. The leakage depends on the radius and the index contrast. Large radius and high index-contrast lead to lower power leakage due to better optical confinement in the microresonator. For an air-cladding silicon microresonator, the refractive index is assumed to be 3.46 at 1550 nm wavelength range. Due to the strong optical confinement in high-index-contrast silicon WGM microresonators, the radiation loss reduces as the microresonator radius is increased. The bending loss is negligible if the radius is larger than 10 μm [61].

Two-photon absorption is one of the intrinsic losses [97]. Two-photon absorption is significant only when the field intensity confined in the resonator is strong enough to induce nonlinear optical effects. In silicon-based microresonators, extra loss can occur due to free carriers generated by two-photon absorption.

Scattering loss results from surface roughness. It is usually the dominant optical loss in sub-micron silicon photonics due to the fabrication imperfections. In high index-contrast material, sidewall roughness induces strong perturbations on the guided modes because strong electric fields on the sidewall are exposed to this roughness. Minimizing surface roughness is an active research area. Microfabricated resonators with high Q has been demonstrated in silica [93] and Si [61]. In this work, a novel hydrogen-assisted annealing process is introduced to reduce the optical loss induced by surface roughness. By enhancing the silicon surface mobility, this CMOS-compatible annealing process creates a smooth surface while maintaining the single crystalline structure. Details will be discussed in Chapter 3.

2.5 Analysis of Coupled Microresonator

2.5.1 Microresonator with One Coupler

After analysis of the characteristics of the microresonator, we now investigate how the microresonator interacts with the coupler. First we exam the system of microresonator with one coupler. Figure 2.6 illustrates the optical wave transmission in the system with a waveguide coupled to a microresonator. The resonant frequency of the microresonator is indicated as ω_0. As the optical wave with a resonant frequency ω_0 propagates towards the microresonator, the optical power is coupled and stored inside the microresonator. Meanwhile, the stored energy couples back to the waveguide and interferes with the propagating waves.

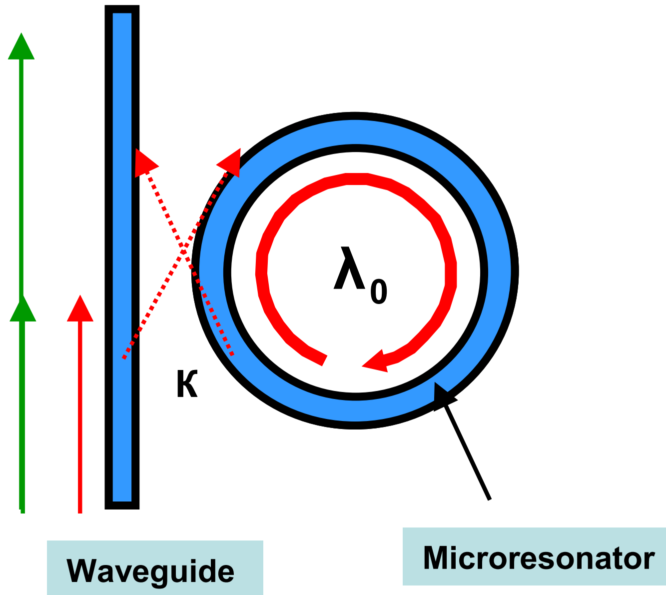

Figure 2.6 Schematic of a microresonator with one waveguide coupler. λ_0 is the resonant wavelength, and κ is the power coupling ratio between the waveguide coupler and the microresonator.

According to the time-domain coupling theory [5], the optical transmission can be expressed as a function of resonant frequency (ω_0), power coupling ratio between the microresonator and the waveguide coupler (κ), round-trip propagation time (T), and round-trip resonator loss (γ):

$$T_{through}(\omega) = \frac{j(\omega-\omega_0)+(\gamma-\kappa)/2T}{j(\omega-\omega_0)+(\gamma+\kappa)/2T} \tag{2.17}$$

where round-trip propagation time $T = {2\pi R}/{\upsilon_g}$, R is the radius of the microresonator, υ_g is the group velocity of the mode inside the microresonator. The round-trip resonator loss γ is related to the resonator loss α by $\gamma = 2\pi R \cdot \alpha$, if R is assumed to be the modal radius and α is small.

We now have

$$Q = \frac{\omega_0}{[1-\exp(-\alpha \cdot 2\pi R)] \cdot \frac{v_g}{2\pi R}} \tag{2.18}$$

Further derivation to reveal the relationship of Q and resonator loss α shows:

$$Q = \frac{\omega_0 \cdot n_g}{\alpha \cdot C} = \frac{2\pi \cdot n_g}{\alpha \cdot \lambda_0} \tag{2.21}$$

Depending on the relative magnitude of the power coupling ratio and the round-trip resonator loss, three coupling regimes are defined: when $\kappa < \gamma$, it is in under-coupling regime; when $\kappa > \gamma$, it is in over-coupling regime; when $\kappa = \gamma$, it is in critical coupling condition. The condition of critical coupling is a fundamental property of waveguide-resonator coupling system. It refers to the condition in which the waveguide coupling loss is equal to the internal resonator loss. The resulting transmission goes to zero at the resonant wavelengths at the output of the waveguide.

In Figure 2.7 we have calculated the optical transmission spectra around the resonant wavelength of 1550 nm in the three coupling regimes. γ is assumed to be 0.017. The power coupling ratios are (a) under-coupling, κ=0.0005, (b) critical-coupling, κ=0.017, and (c) over-coupling, κ=0.1.

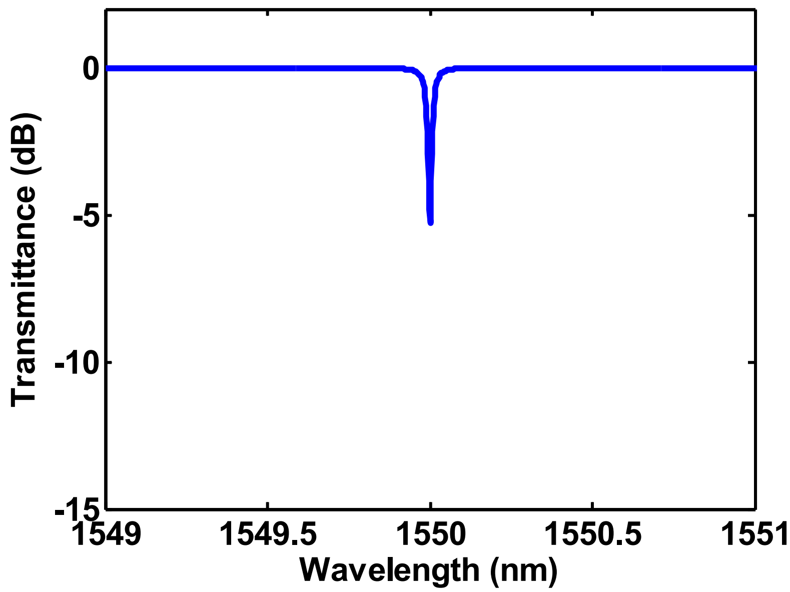
0
-5
-10
-15
Transmittance (dB)
1549
1549.5
1550
1550.5
1551
Wavelength (nm)

(a)

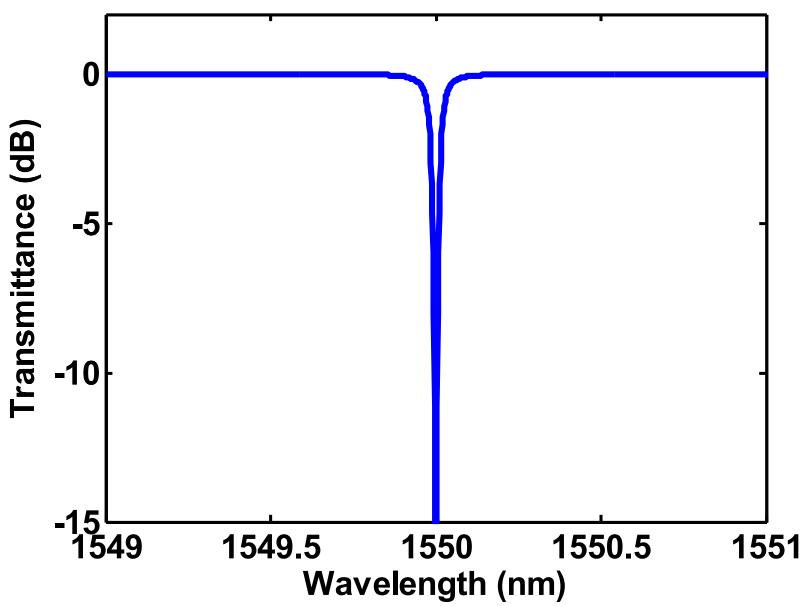
0
-5
-10
-15
Transmittance (dB)
1549
1549.5
1550
1550.5
1551
Wavelength (nm)

(b)

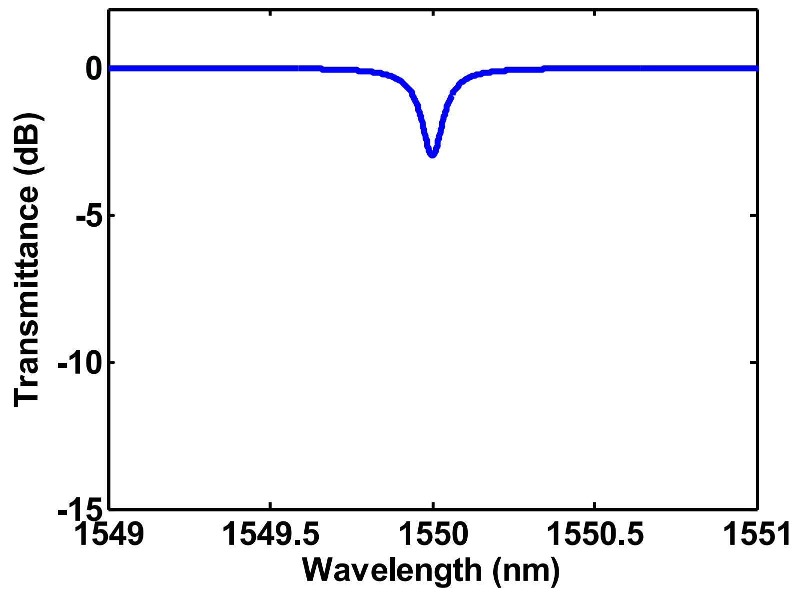

(c)

Figure 2.7 Calculated optical transmission spectra around the resonant wavelength of 1550 nm in three coupling regimes: (a) under-coupling regime, κ=0.005 (κ < γ), (b) critical coupling, κ = γ =0.017, and (c) over-coupling regime, κ=0.1 (κ > γ).

2.5.2 Microresonator with Two Couplers

We have analyzed the scenario in which one waveguide coupler is coupled to the microresonator. Similar principles applied to the microresonator with two waveguides, in which case the energy of the resonant wavelengths can be transferred from one waveguide coupler to the other.

Each of the two waveguides can be coupled to the microresonator with power coupling ratios controlled independently, as shown in Figure 2.8. The microresonator circuit function as an optical add-drop multiplexer (OADM) for the resonant wavelength. There are four ports: input, through, add and drop port, as shown in Figure 2.8. At resonance, the propagating light launched from the input port can be transfer to the drop port through the coupling between the microresonator and the waveguides. Likewise, light in the add port can be also transferred to the through port. Therefore, this two-waveguide-coupled microresonator structure can be utilized as an add-drop optical filter, as first proposed by Marcatili [96].

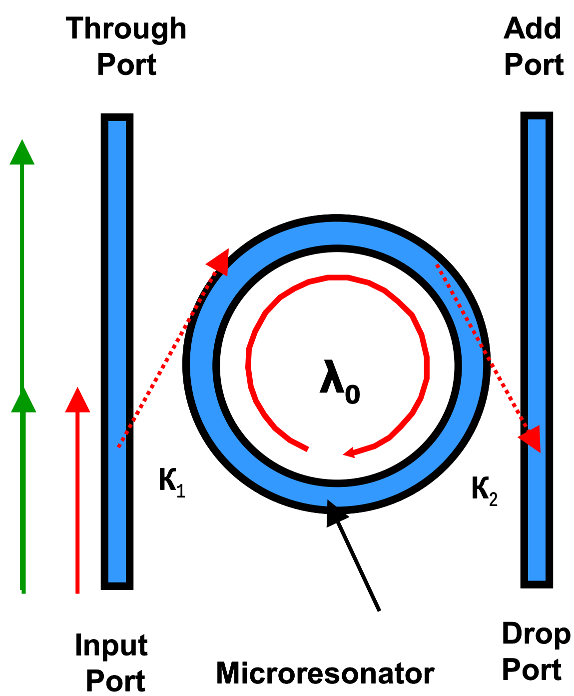

Figure 2.8 Schematic of a microresonator with two waveguides as input and output couplers. λ_0 represents the resonant wavelength. κ_1 and κ_2 are the power coupling ratios for the input and output waveguides, respectively.

According to the time-domain coupling theory [5], the optical transmission with two couplers is different from that with one coupler. It can be expressed as a function of resonant frequency (ω_0), power coupling ratio of the input and output waveguides (κ_1 and κ_2, respectively), round-trip propagation time (T), and round-trip resonator loss (γ) as:

$$T_{through}(\omega) = \frac{j(\omega - \omega_0) + (\gamma + \kappa_2 - \kappa_1)/2T}{j(\omega - \omega_0) + (\gamma + \kappa_2 + \kappa_1)/2T} \tag{2.20}$$

and

$$T_{drop}(\omega) = \frac{\sqrt{\kappa_1 \kappa_2}\,/T}{j(\omega - \omega_0) + (\gamma + \kappa_2 + \kappa_1)/2T} \tag{2.21}$$

where $T_{through}(\omega)$ and $T_{drop}(\omega)$ represent the amplitude transfer functions at the through and the drop ports, respectively.

The transfer function from the input to the through port in Equation (2.20) is analogous to that of a single-waveguide-coupled microresonator in Equation (2.17). The difference is that the round-trip resonator loss, γ, in Equation (2.17) is now the round-trip resonator loss plus the output waveguide coupling, $\gamma + \kappa_2$. The latter is the equivalent loss of the microresonator from the perspective of the input waveguide. Thus in the model they are equivalent mathematically.

For resonators with high intrinsic Q, γ is small and the transmission characteristics are dominated by coupling. By controlling κ_1 and κ_2 simultaneously, we can vary the transmission shape without much change of the transmission wavelengths or the intrinsic Q. This provides some unique benefits for tunable filter applications. The bandwidth of the filter can be tuned without sacrificing the peak transmissions. Figure 2.9 shows an example of tuning of the transmission spectra around the resonant wavelength of 1552 nm. In Chapter 6, a detailed analysis will be presented together with the experimental demonstration of a bandwidth-tunable microresonator that is proposed here.

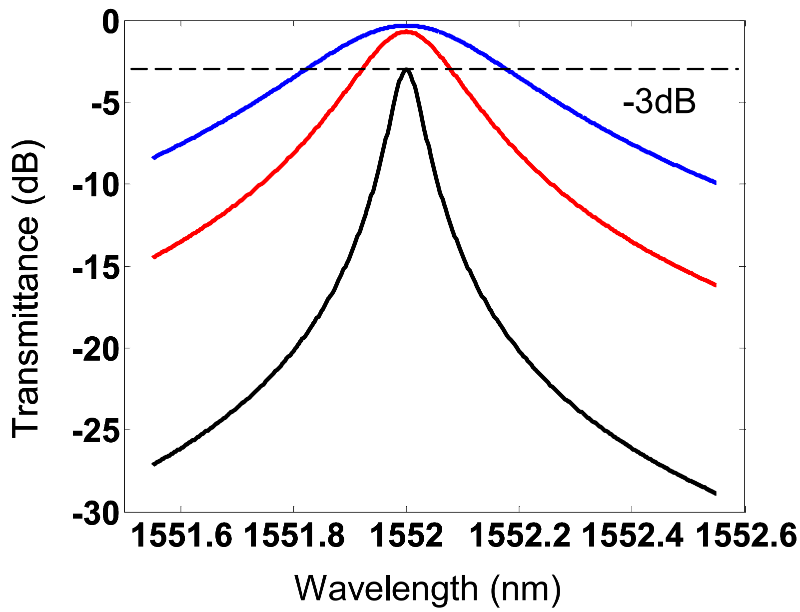

Figure 2.9 Calculated transmission spectra of the optical add-drop multiplexer for various values of κ_1 and κ_2. Top: κ_1 = 0.317, κ_2=0.3; middle: κ_1 = 0.117, κ_2=0.1; bottom: κ_1 = 0.034, κ_2=0.017. γ of the microresonator is assumed to be 0.017.

2.6 Review of Microdisk Resonators

With the aforementioned analysis, it is known that a microdisk can support multiple WGMs in the radial and azimuthal directions. Previously, silicon microdisk resonators with integrated MEMS-actuated tunable couplers have been realized, with both laterally [63, 98] and vertically coupled waveguides [64].

In the laterally-coupled microdisk resonator, the waveguides and the microdisk were fabricated on the same silicon layer. The waveguide couplers were deformed laterally using MEMS actuation to control the coupling ratio. With this laterally-coupled microdisk design, a switchable notch filter was demonstrated. Switching of resonance peaks with a 9 dB contrast ratio was observed. The loaded Q of the microdisk was estimated to be 7,700. A implementation of a tunable dispersion compensator with a dispersion tuning range of 400 ps/nm and a peak group delay of -35 ps has also been reported [63].

In vertically-coupled microdisk resonators, the waveguides and the microdisk were fabricated on two separate silicon layers with a silicon oxide layer in between. Using MEMS actuation, the waveguide couplers were deformed vertically to control the coupling ratio. Coupling ratio was varied over a range from 0 to 34% and a high Q (100,000) has been achieved. Using this vertically-coupled microdisk resonator, a dynamic add-drop filter with 20 dB extinction ratio was demonstrated. For dynamic dispersion compensation application, the vertically-coupled microdisk resonator was able to tune the group delay from 27 ps to 65 ps. The group velocity dispersion was tunable from 185 ps/nm to 1200 ps/nm [64, 99].

2.7 Summary

In this chapter, first we have identified the important parameters for modeling of the microresonators. A generic optical microresonator can be characterized by three key parameters: resonant wavelength λ_0, power coupling ratio κ, and resonator loss α. Changing any of them can vary the transmission characteristics of the microresonator.

Then a comprehensive theoretical analysis is presented to investigate the whispering gallery modes (WGMs) of the microresonator and the modes of the waveguide couplers. A microresonator can support specific WGMs in the radial and azimuthal directions. We have plotted the WGM profiles and investigate the waveguide coupler design to achieve phase matching condition.

The intrinsic loss of a microresonator includes free carrier absorption loss, bending loss, scattering loss, two-photon absorption loss. Using time domain coupling theory, we have analyzed two configurations of the microresonator systems: microresonator with one waveguide, and with two waveguide couplers. By varying the gap spacing, the coupling ratio can be tuned over a wide range, and the microresonator can be operated in under-coupling, critical coupling, or over-coupling regimes.

The microresonator with two waveguide couplers can be used to implement reconfigurable add-drop filters with variable transmission bandwidth. Previous works on laterally- and vertically-coupled microdisk resonators with tunable couplers are reviewed.

Chapter 3 Microtoroidal Resonators: Design and Analysis

3.1 Motivation

In the previous chapter, we have described of the silicon microdisk resonator with integrated micro-electro-mechanical-systems (MEMS) tunable couplers [63, 100]. One drawback of the microdisk resonators is the lack of radial mode control, which could produce additional resonances due to high order radial modes. For a silicon microdisk with 20-μm radius and 250-nm thickness, we have calculated the modal profiles at resonant wavelengths around 1550 nm using the model we have analyzed in Chapter 2. The index of the silicon microdisk is assumed to be 3.46. The index of surrounding air area is 1, and that of the SiO_2 base is 1.46. The fundamental and the 1^{st} higher radial modal profiles are shown in Figure 3.1.

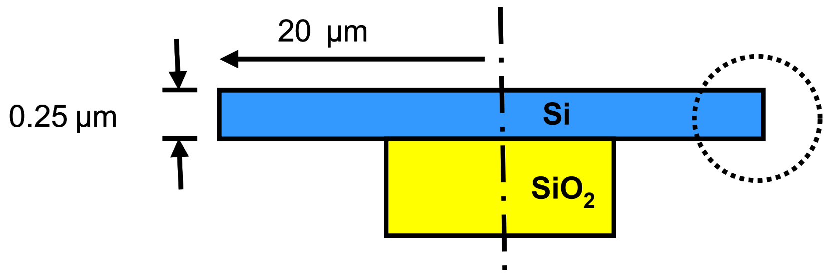

(a)

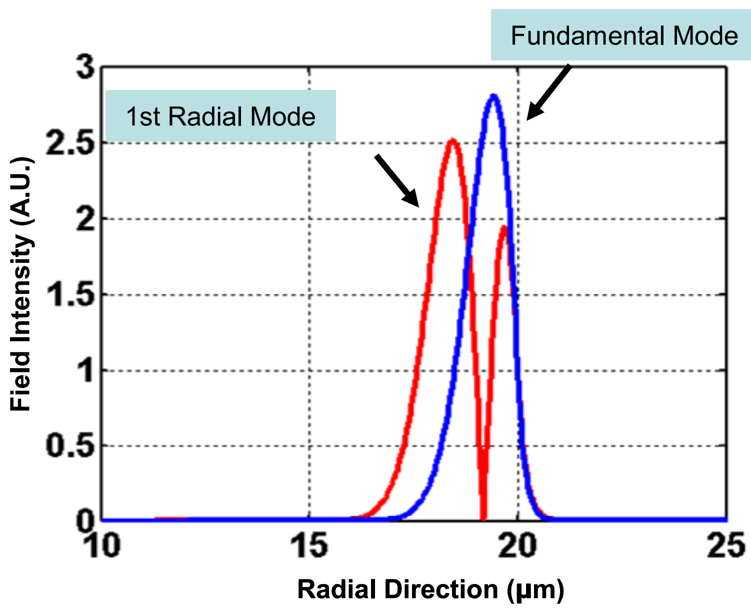

(b)

Figure 3.1 Radial modes profiles of the microdisk resonator. (a) Schematic cross section view of the microdisk structure. The thickness is 0.25 μm and the radius is 20 μm. (b) Calculated fundamental and the first higher order radial mode for microdisk structure in the dotted area shown in (a).

As mentioned in Chapter 2, it is fundamental that due to the refractive index distribution, higher radial modes are always present in microdisks. Figure 3.2 has illustrated the measured multiple radial modes in [101]. In this chapter, we have designed a microtoroidal resonator with MEMS tunable optical coupler. With the two-dimensional confinement in refractive index distribution, microtoroidal resonators offer tighter confinement of the optical guided mode and eliminate multiple radial modes observed in microdisk resonators.

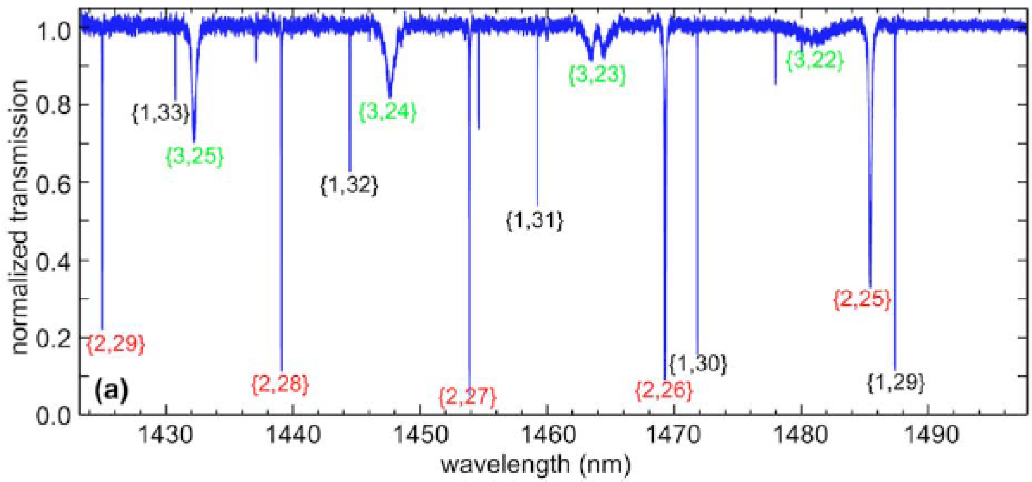

Figure 3.2 Normalized spectral transmission response of a 5 μm radius silicon microdisk resonator from experiments in [101]. It is measured with a fiber taper placed at 0.6±0.1 μm from the disk edge and optimized for TM coupling. The spectrum was normalized to the response with fiber taper at 3 μm laterally away from the disk edge.

3.2 Optical Losses

3.2.1 Optical Scattering Loss

Surface roughness is a severe challenge for many micro- and nanophotonic devices due to the optical scattering loss. It is usually the dominant optical loss in sub-micron silicon photonics, as investigated in optical waveguides and micro surface applications [102-104]. Due to the high index-contrast, sidewall imperfections induce strong perturbations on the guided modes since they have strong electric fields on the sidewall. The loss increases rapidly with shrinking of waveguide dimensions. Figure 3.3 shows the TE-like optical fundamental modal profiles in (a) a 5 μm x 5 μm rectangular cross section and in (b) a 0.5 μm x 0.5 μm rectangular cross section channel waveguides. It is obvious that a significant amount of optical fields are outside the waveguide boundary in the smaller waveguide.

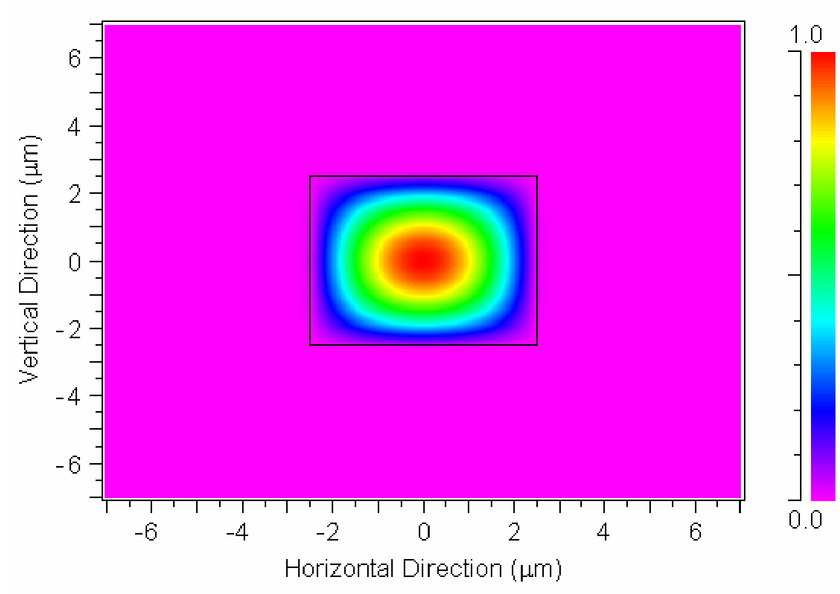

(a)

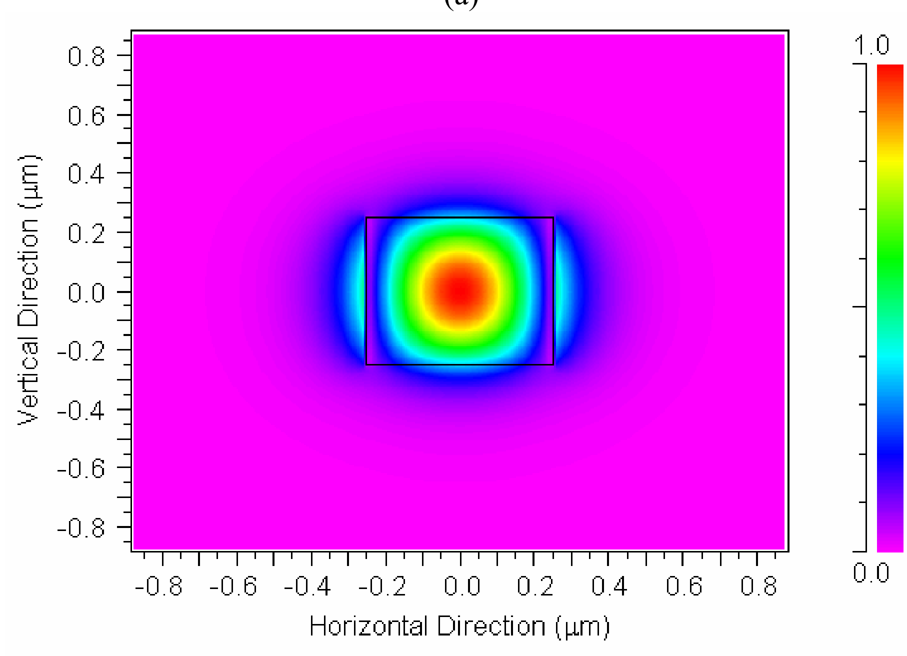

(b)

Figure 3.3 Comparison of TE-like optical fundamental modes in channel waveguides. (a) Mode profile in a 5 μm x 5 μm rectangular waveguide. (b) Mode profile in a 0.5 μm x 0.5 μm rectangular waveguide.

Based on the model introduced by Tien [105], the propagation loss induced by surface roughness was analyzed [106]. Figure 3.4 illustrates the calculated loss due to the surface roughness of 1 nm, 3 nm and 5 nm for a channel waveguide. The waveguide has a thickness of 0.25 μm. Due to the high index contrast, the dimensions of the silicon waveguide have to be sub-micron to meet the single mode operation criterion. However, as shown in Figure 3.4, for sub-micron waveguides, the optical loss increases dramatically with increasing surface roughness. Thus a smooth sidewall with surface roughness of the order of a nanometer is critical for nanophotonic integrated circuits.

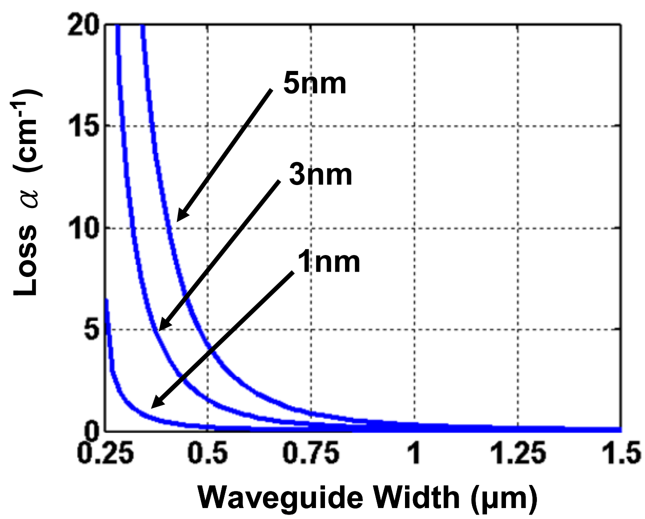

(a)

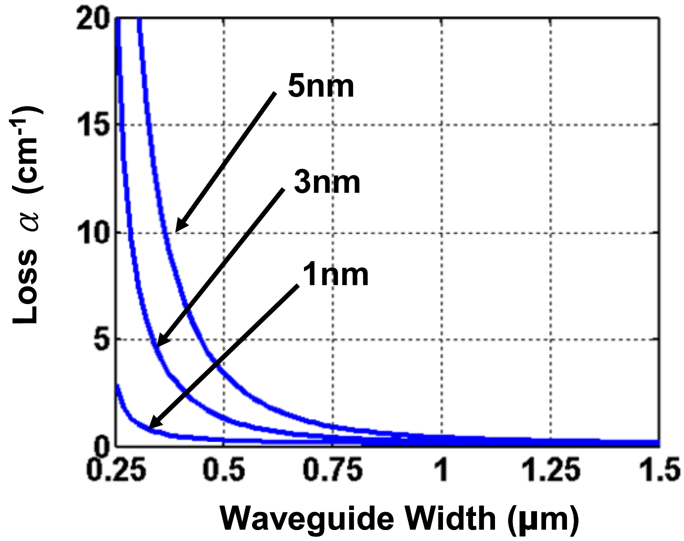

(b)

Figure 3.4 Calculated propagation loss induced by surface roughness of 1 nm, 3 nm and 5 nm to a channel waveguide with rectangular cross section [106]. The waveguide thickness is 0.25 μm. (a) TE-like mode loss (b) TM-like mode loss calculation.

For dry etched waveguides, the roughness could come from the finite addressing size of the photomasks, the limitations of photolithography, as well as photoresist and device materials etching process. Although the state-of-the-art complementary metal-oxide-semiconductor (CMOS) processing can achieve sidewall roughness less than 5 nm [107], in many conventional research laboratories, sidewall roughness is larger than 10 nm, which causes severe optical loss for nanophotonic devices.

To reduce the surface roughness, different approaches have been investigated, in terms of either etching or post-processing. Wet etching process such as tetramethylammonium hydroxide (TMAH) and potassium hydroxide (KOH) create smooth surfaces, but the drawback is that the structure geometry is defined by crystal planes, which limits the patterning flexibility. In post-dry etching processes to reduce roughness, thermal oxidation treatment is able to smooth the sidewall for silicon structures fabricated on SOI according to demonstrations in [108, 109]. However, the oxidation process consumes silicon materials significantly. It also it introduces thermal residual stress in silicon.

3.2.2 Hydrogen Annealing Process Design

We have investigated the hydrogen annealing process to reduce surface roughness. Hydrogen annealing was previously reported to reduce the interface state density and improve the CMOS device performance [110-113]. The surface mobility of silicon atoms is enhanced in hydrogen ambient at temperature conditions below the melting point (1414ºC) [114, 115]. And the surface silicon atoms migrate to minimize the total surface energy, thus the surface roughness is smoothed out while preserving the crystalline structure. It has been utilized to remove surface micro-defects (SMD) roughness in bulk silicon [116, 117].

In addition to changing the local surface morphology, hydrogen-enhanced surface migration also changes the global topology profile if the surface migration length is comparable to or larger than the structural dimensions [118, 119]. In bulk silicon case, it has been demonstrated to form round corners [120, 121] and various shape trenches and voids [122-124]. In silicon-on-insulator (SOI) where the silicon oxide layer becomes a barrier for the atom migration, hydrogen-enhanced surface migration can create rounded three-dimensional (3D) microstructures such as microspheres, micropillars, submicron wires, and microtoroids in the silicon layer [125-127]. Figure 3.5 shows SEM pictures of as-etched waveguides and mesa structures before and after the hydrogen annealing process. Surface roughness has been greatly reduced and the corners have been rounded while the volume of silicon is preserved.

This effect of reducing the surface roughness and changing the profile is similar to the thermal reflow process for glasses [93, 128, 129] or polymers [130-133]. The SiO_2 microtoroidal resonators made in material were recently fabricated by thermal reflow process [93]. However, such process can not be applied to single crystalline structures. Instead, we use the hydrogen annealing process to create three-dimensional toroidal structures while preserving the single crystalline quality for optical transmission performance [125, 127].

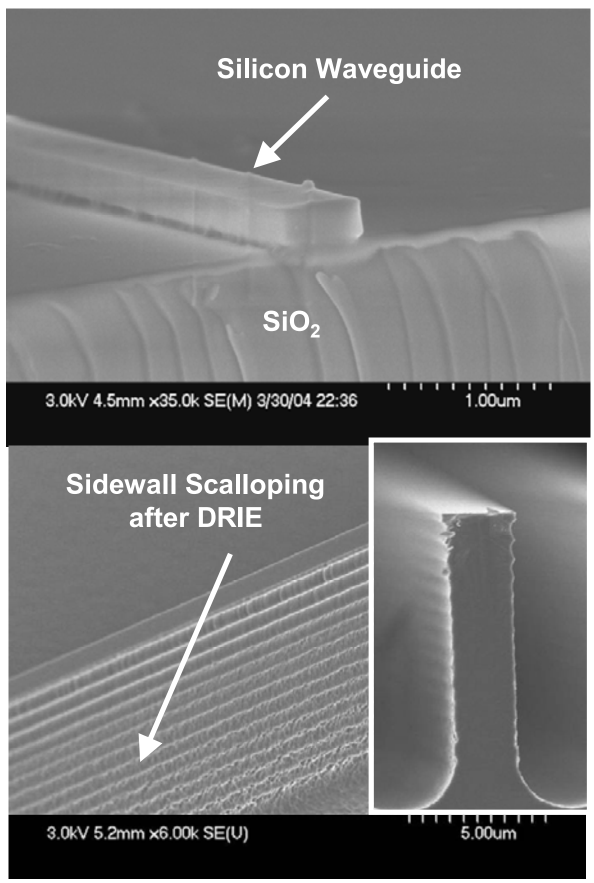

(a)

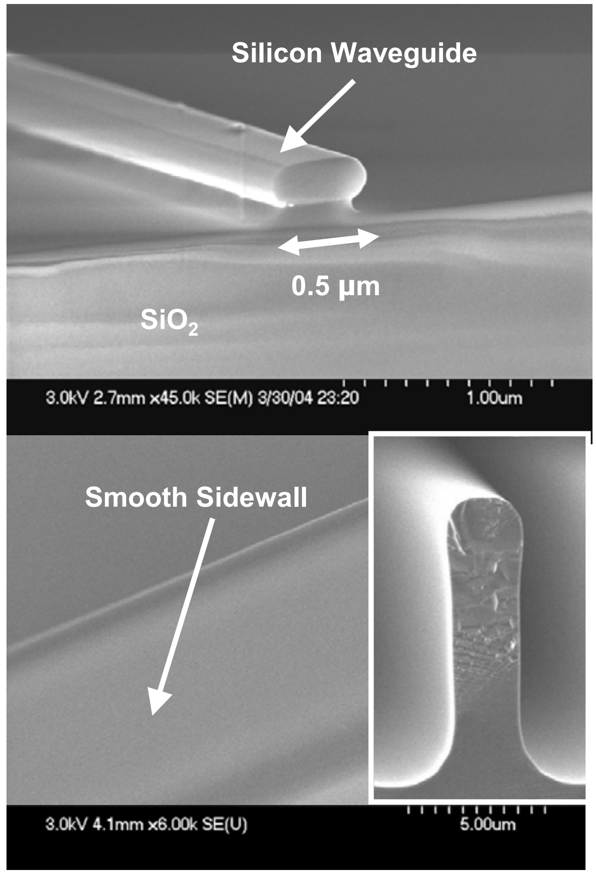

(b)

Figure 3.5 SEM pictures of as-etched waveguides and mesa structures before and after the hydrogen annealing process. (a) Before annealing: as-etched 0.34µm-high, 0.5µm-wide waveguide and 10µm-high, 2.5µm-wide mesa with rough sidewall scalloping after Deep Reactive Ion Etching (DRIE). (b) After annealing: the surface roughness is reduced and the corners are rounded. The insets show the cross sections of the mesa structure.

The process flow for creating a microtoroidal structure on SOI is shown in Figure 3.6. First the microdisk is patterned and etched. Then a controlled partial release of the SiO_2 layer leaves space for expansion in the vertical direction for the microtoroidal edge. Finally the hydrogen annealing treatment creates the microtoroid. A SEM micrograph of a test structure after the annealing process is shown in Figure 3.7.

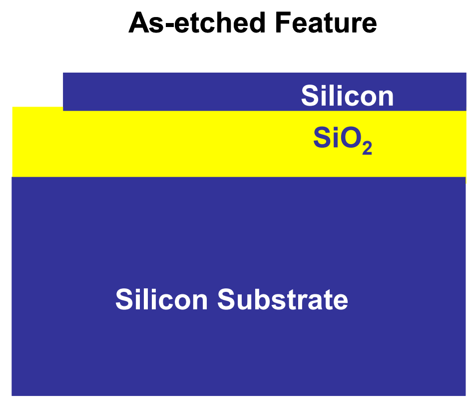
As-etched Feature
Silicon
SiO_2
Silicon Substrate

(a)

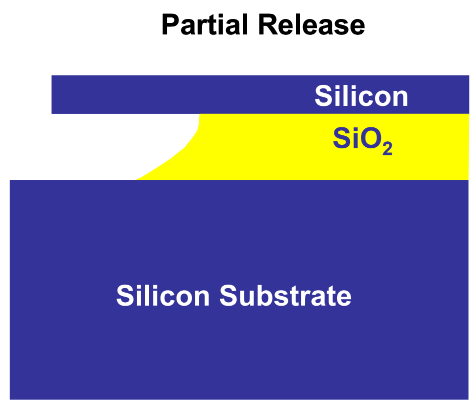
Partial Release
Silicon
SiO_2
Silicon Substrate

(b)

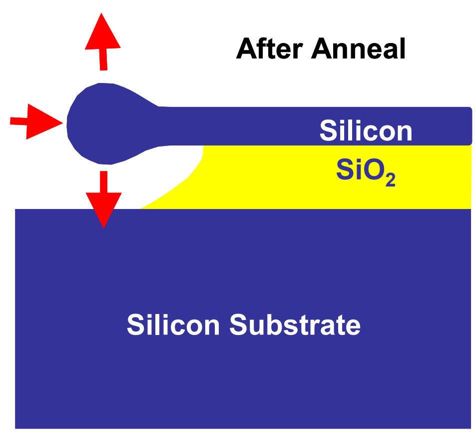
After Anneal
Silicon
SiO_2
Silicon Substrate

(c)

Figure 3.6 Schematic illustrating the microtoroid creation process in signal crystalline SOI. (a) The microdisk is patterned and etched. (b) Controlled partial release of the microdisk leaves space for vertical expansion. (c) The hydrogen annealing treatment creates the microtoroidal edge.

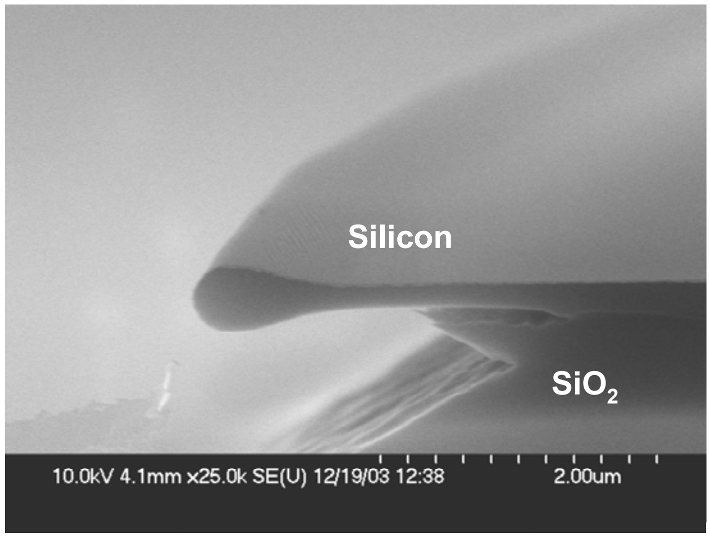

Figure 3.7 SEM micrograph of a test structure after the hydrogen annealing process showing the cross section view of the microtoroidal edge.

When microtoroid profile is created with the hydrogen annealing process, the surface roughness is reduced and optical mode is more confined compared to the microdisks. To integrate the microtoroidal resonators with MEMS tunable waveguides, we have combined the hydrogen annealing process with wafer bonding technique. Details of the combined process will be discussed in the fabrication section of this dissertation.

3.3 Device Optical Design

3.3.1 Optical Mode Modeling

We have calculated the propagation constants of the microtoroid with the actual shape produced by hydrogen annealing using beam propagation method (BPM) simulation [90]. The optical field profile of the toroidal resonator at 1.55 μm wavelength is shown in Figure 3.8. We have used the following parameters for the calculation: refractive indices of Si and air are 3.46 and 1.0, respectively; the bend radius of the toroid is 19.5 µm; and the radius of the toroid is 200 nm. As shown in Figure 3.8, both the TE-like and the TM-like modes support only one optical radial mode that tightly confined in silicon.

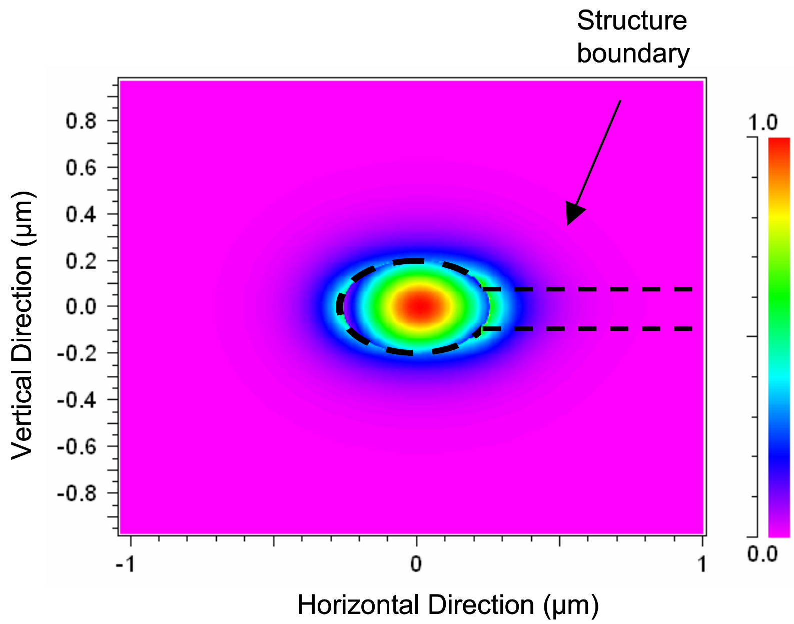

(a)

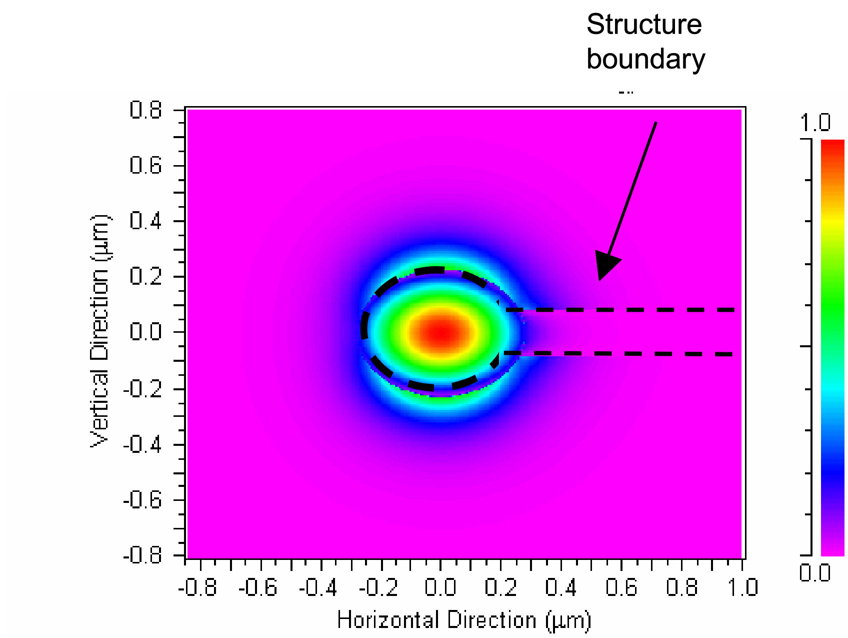

(b)

Figure 3.8 Simulated optical mode profiles of the microtoroid at 1.55 μm wavelength: (a) For TE-like polarized light (b) For TM-like polarized light.

3.3.2 Phase Matching

Phase matching between the waveguide and the microtoroidal resonator is important to achieve efficient coupling. It is satisfied when the two wave modes have the same propagation constant β.

We have achieved phase matching is achieved by controlling the dimensions of the waveguide. Using the theoretical model we introduced in Chapter 2, Figure 3.9 shows the calculated propagation constants of the waveguide (lines) and the microtoroid (dots) versus wavelength for various waveguide dimensions. Here, we fix the waveguide width at 0.69 μm, which is the minimum linewidth that can be regularly produced by the lithography tool (Nikon NRS 5:1 reduction stepper). As shown in Figure 3.9, the waveguide with 0.25 μm thickness is best matched to the microtoroid mode over a wide wavelength range centered at the wavelength of 1550 nm.

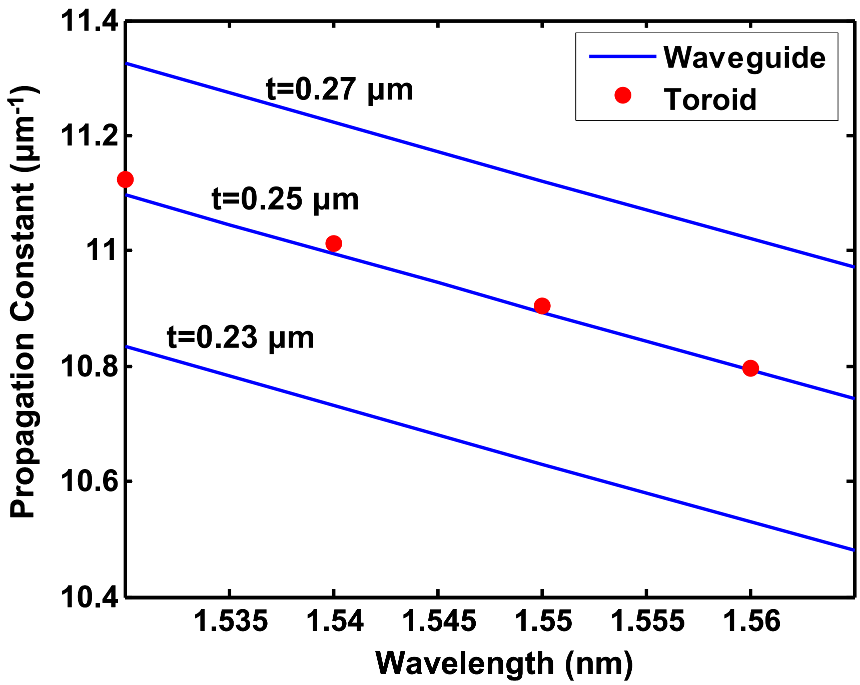

Figure 3.9 Calculated propagation constants of the waveguide and the microtoroid versus wavelengths for various waveguide thicknesses, *t*. The width of the waveguide is fixed at 0.69 μm.

3.4 Device Integration

3.4.1 Device Structure Design

The schematic of the tunable microtoroidal resonator is shown in Figure 3.10. Two suspended waveguides, which serve as input and output signal buses respectively, are vertically coupled to the center microtoroidal resonator. It is realized on a two-layer silicon-on-insulator (SOI) structure. The microtoroid and the fixed electrodes of the MEMS actuators are fabricated on the lower SOI silicon layer, while the suspended waveguides are integrated on the upper SOI silicon layer. The initial spacing between the microtoroid and the waveguides is designed to be 1 μm. This parameter is chosen so that there is negligible coupling without actuation, as shown in Figure 3.10(a). With increasing actuation voltage between the waveguide and the fixed electrodes, the suspended waveguide is pulled down towards the microtoroid, increasing the optical coupling exponentially, as illustrated in Figure 3.10(b).

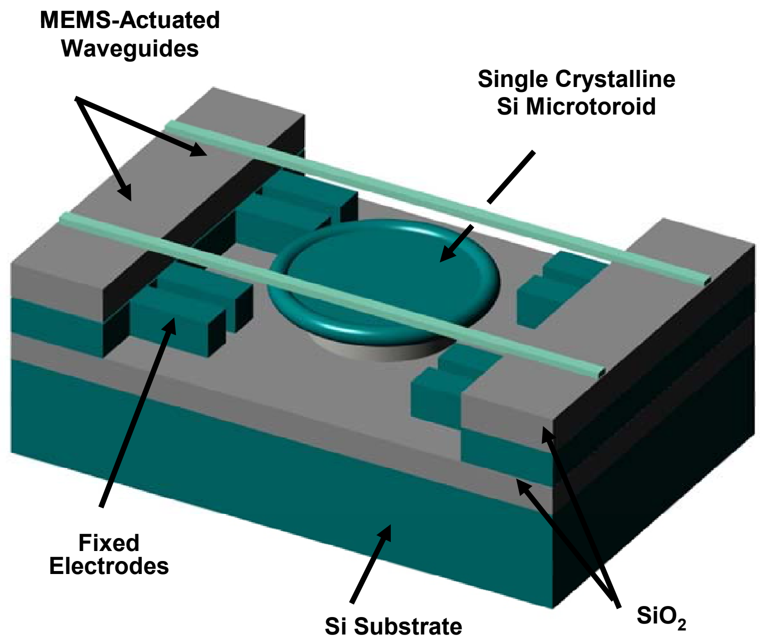

(a)

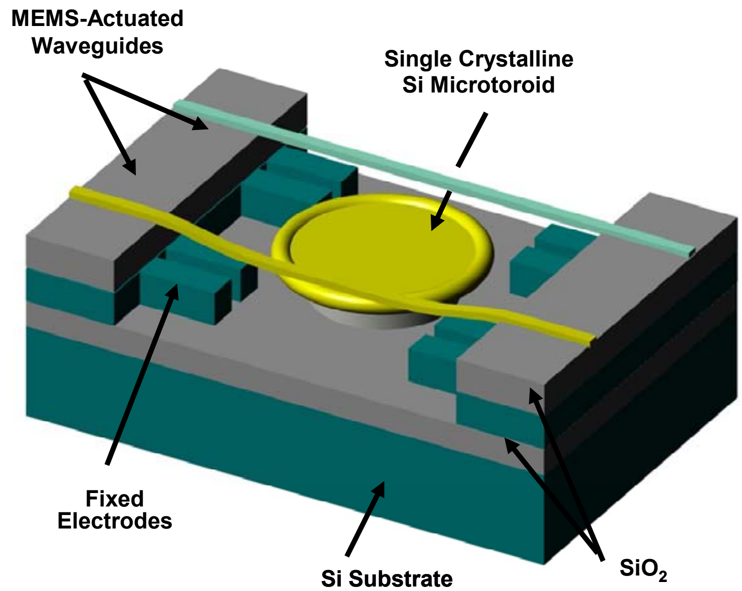

(b)

Figure 3.10 Schematic of the microtoroidal resonator with integrated MEMS tunable couplers. (a) At zero bias, the initial spacing is large enough to ensure negligible coupling between the resonator and the waveguide coupler. (b) Under biased actuation only for the lower waveguide coupler. The lower waveguide is pulled downward by the actuation voltage to increase coupling. The upper waveguide remains straight (uncoupled).

3.4.2 MEMS Actuation Design

The detailed actuator design is as shown in Figure 3.11. To actuate the suspended waveguides, we employ a comb-finger-like electrostatic actuator on both ends of the waveguide couplers, as shown in the A-A' cross-sectional view of Figure 3.11.

The top layer waveguides are electrically grounded. When a voltage is applied on the bottom layer electrodes, the suspended waveguides are pulled downwards by electrostatic force, so that the gap spacing between the waveguide and the microtoroid edge decreases, as shown in the B-B' cross-sectional view of Figure 3.11. With the control of the applied actuation voltage, the gap spacing can be continuously adjusted from 1 μm to almost physical contact.

This integrated actuator design enables us to bias the microtoroidal resonator in all coupling regimes: under-coupling, critical coupling, and over-coupling, or completely decoupled from the waveguide coupler. The principles of this kind of MEMS-actuated microresonators design have been reported in [64].

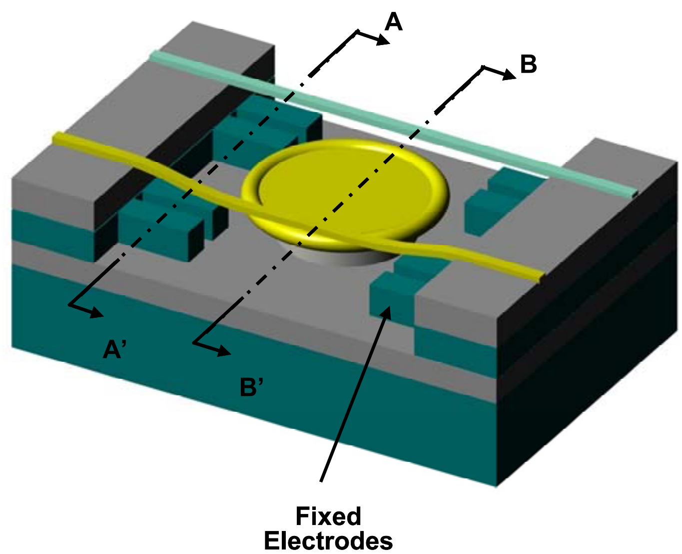

(a)

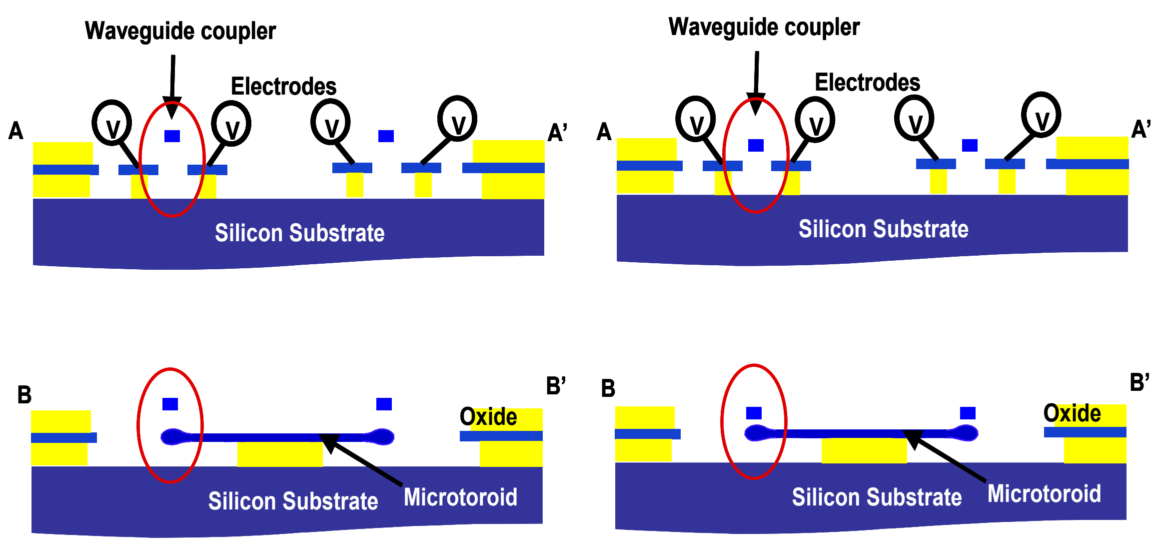

(b)

Figure 3.11 Schematics of the MEMS actuator design for the vertically-coupled microtoroidal resonator. (a) 3D schematic of the microtoroidal resonator with the integrated waveguides. (b) Cross section views of the actuator (A-A') and the microtoroid edge (B-B') with (left panel) and without (right panel) bias, respectively. When a voltage is applied to the bottom electrodes, the suspended waveguides are pulled downwards to decrease the gap spacing between the waveguide and the microtoroid edge.

There is a design trade-off in the doping concentration of the Si device layers. High doping is desired for better MEMS actuation, while low doping is necessary to minimize optical absorption due to free carriers. Fortunately, electrostatic actuation does not require low resistivity. With a doping concentration of 10^{14} cm^{-3} (n-type dopants), a resistivity of 10 Ω-cm and an optical loss smaller than 0.01 cm^{-1} can be achieved. This absorption coefficient corresponds to a Q of 10^8 for microresonators if it is the dominant loss. In practical demonstration, the surface roughness induced loss remains as the dominant loss.

3.5 Summary

In this chapter, we have analyzed the radial modes limitation of microdisk resonators, and introduced the design of microtoroidal resonators to achieve better optical confinement in the radial direction. This microtoroidal shape is realized by the hydrogen annealing process. It also reduces the optical loss induced by surface roughness. By enhancing the silicon surface mobility, the hydrogen annealing process creates a smooth surface while maintaining single crystalline structure of silicon. This is important for micro- and nano-scale photonic devices with high index contrast interface because they are very sensitive to scattering loss caused by surface roughness. With the modal simulation and phase matching calculation, we have also analyzed the optical modes in both the microtoroid and the waveguide. Phase matching is achieved by designing the thickness of waveguide. This optical design and novel fabrication process enable us to realize high performance tunable integrated microresonators.

Chapter 4 Microtoroidal Resonators: Fabrication and Optimization

4.1 Fabrication Process Flow

In this chapter, we investigate the fabrication process for the vertically-coupled tunable microtoroidal resonator described in the previous chapter.

The fabrication process flow is outlined in Figure 4.1 as the following module steps. First, the microtoroid and the fixed electrodes of the MEMS actuators are patterned on the bottom silicon layer, as shown in Figure 4.1(a). Then the disk is partially released to expose the edge. The hydrogen annealing process is used to form the microtoroid as in Figure 4.1(b). Next, another SOI wafer is bonded to the microtoroid wafer as in Figure 4.1(c). Its substrate is removed to reveal the second silicon layer. This design is advantageous to deposition of poly silicon to form the upper silicon layer of the double-layer structure, because single crystalline silicon has better optical loss performance compared with polysilicon. The waveguide couplers in the upper layer of the double-SOI wafer are aligned and patterned to the edges of the underneath microtoroids, as in Figure

4.1(d). As the last step, the waveguide couplers around the microtoroid are patterned and released for MEMS actuation.

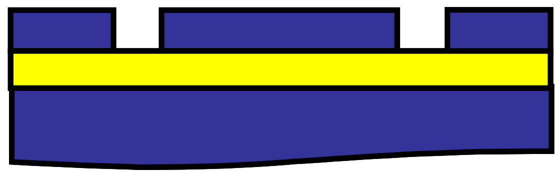

(a)

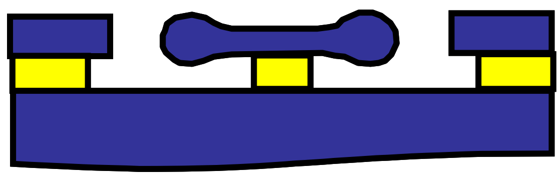

(b)

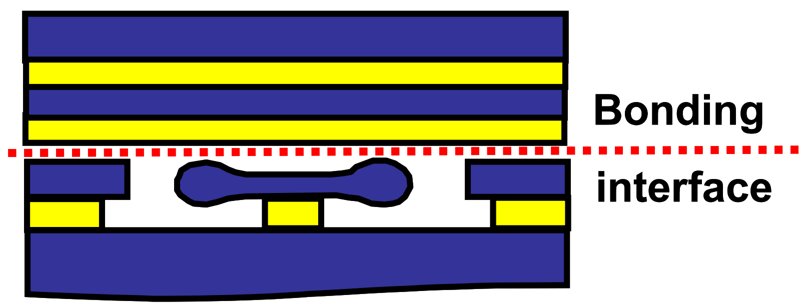

(c)

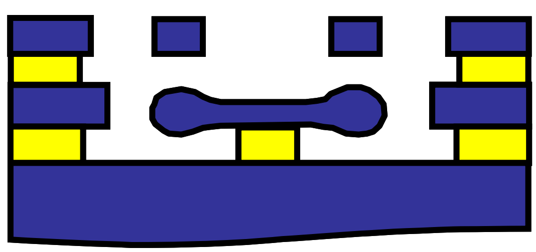

(d)

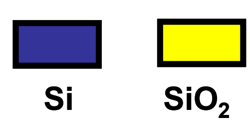

Figure 4.1 Fabrication process flow design for the integrated tunable microtoroidal resonator. (a) Pattern the microdisk and the fixed electrodes of the MEMS actuators at the bottom silicon layer. (b) Partially release the microdisk to expose the edge and use the hydrogen annealing process to form the microtoroid. (c) Bond another SOI wafer to the microtoroid wafer and remove the substrate to reveal the second silicon layer for the waveguide patterning. (d) Align and pattern the waveguide couplers on the upper silicon layer to the edges of the microtoroid. Release the center part of the waveguides to achieve the MEMS-actuated integrated device.

4.2 Process Challenges and Solutions

4.2.1 Planarity of Bonding Surface

The main challenge of the aforementioned design is the nonplanar topography of the microtoroids, produced by the hydrogen annealing process as analyzed in Chapter 3. This nonplanar topography prohibits the tight surface contact which is crucial for wafer bonding, as highlighted in Figure 4.2(a). We solved this problem by thinning the edges of the microdisks using thermal oxidation process before hydrogen annealing so that the microtoroid surface is lower than the surrounding planar area. The surrounding area is prevented from deformation by a silicon nitride film, as shown in Figure 4.2(b). The center part of the microtoroid is also protected from oxidation or hydrogen annealing so it will remain planar and bond to the top SOI wafer. This minimizes void formation and improves the bonding quality. The detailed process is optimized in the following sections.

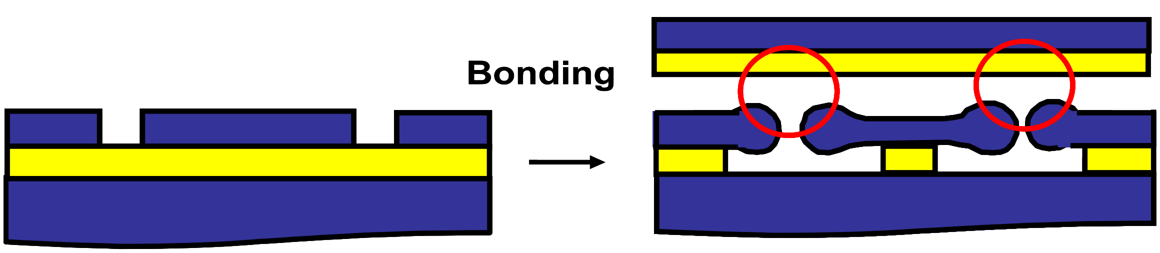

(a)

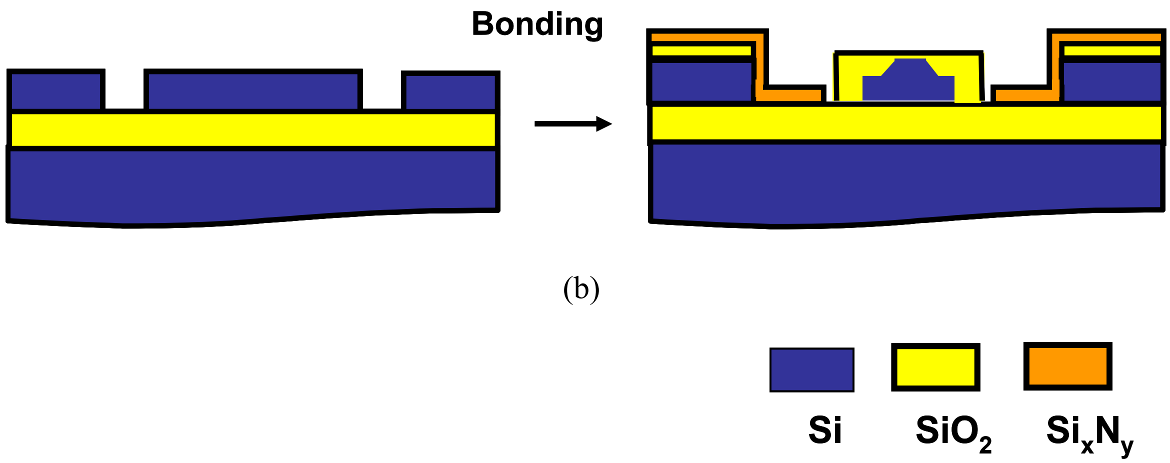

Figure 4.2 Thinning down process design to solve the nonplanar topography of the microtoroid. (a) Nonplanar topography of the microtoroids occurs in the hydrogen annealing process, preventing close contact of surfaces for successful wafer bonding. (b) An improved process for wafer bonding on microtoroids. The edge of the microdisk is thinned down using thermal oxidation process before hydrogen annealing so that the microtoroid surface was lower than the surrounding planar area. By depositing and patterning a silicon nitride film, the planar area is protected during the hydrogen annealing process.

4.2.2 Retraction of Microtoroid Edges

During the hydrogen annealing process, the edges of the microdisks are transformed to form the microtoroids. Unlike the thermal oxidation process, it does not consume silicon and the microresonator remains single crystalline.

Because of the profile transformation, the edges of the microtoroids retract from those of the originally patterned microdisks. Assuming the total silicon volume is preserved, we can calculate the amount of the edge retraction for a 200-nm thick microdisk according to the accurate shape of the microtoroid. As shown in Figure 4.3(b), after the hydrogen annealing treatment, the edge of the microdisk has retreated 1.17 μm.

Therefore, we have used this parameter to offset the waveguides alignment in the mask design, as shown in Figure 4.4.

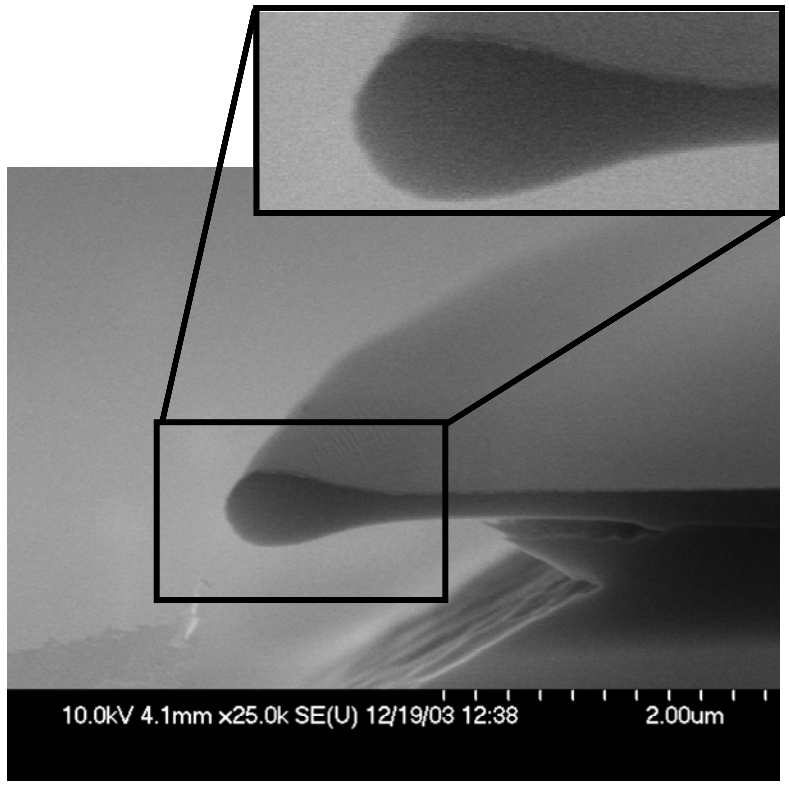

(a)

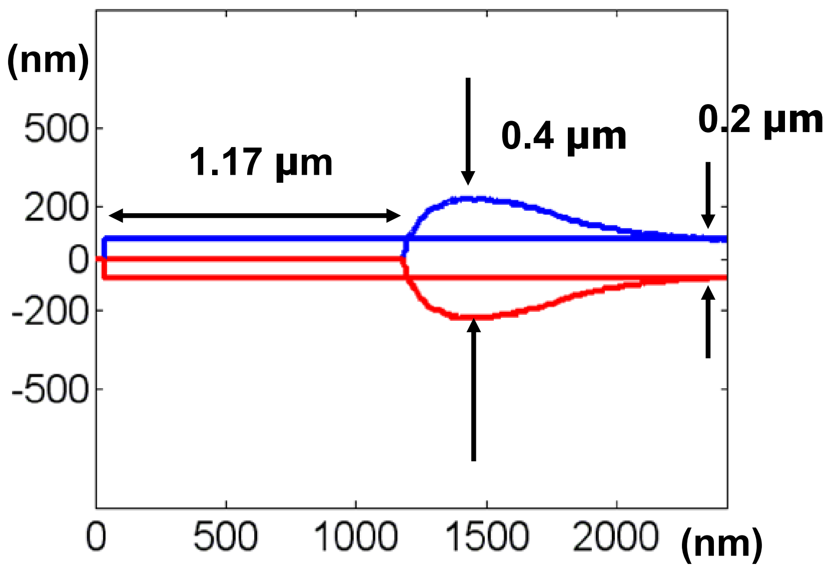

(b)

Figure 4.3 Microtoroid edge transformation calculation for the alignment design. (a) SEM showing the cross-sectional shape of the microtoroid. (b) Calculated edge retraction of the microtoroid from the edge of the original microdisk after the hydrogen annealing process, assuming the volume unchanged.

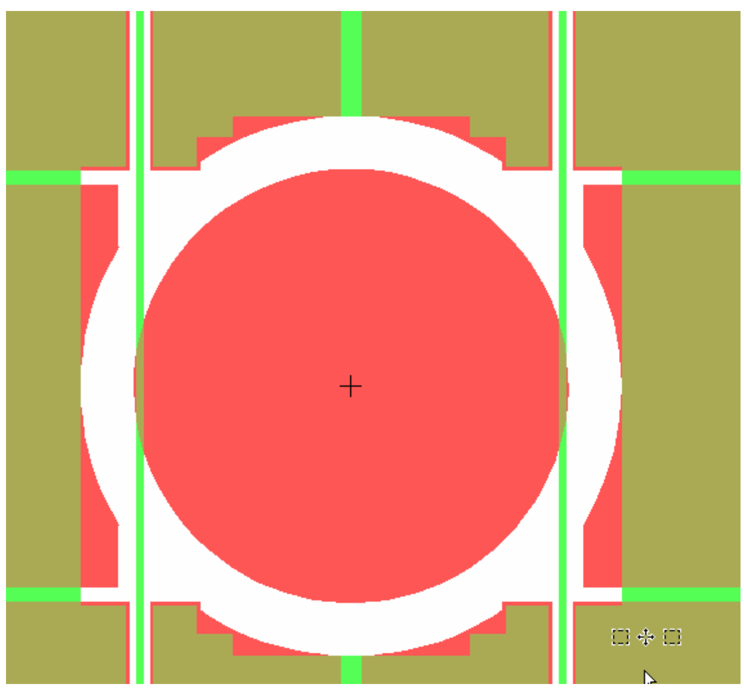

Figure 4.4 Photomask layout of the waveguide (green) and the microtoroid (red) layers. The waveguides are aligned to the edge of the microtoroid layer with an offset equal to the retraction.

4.3 Process Flow and Optimization

4.3.1 Process Flow for Integration

The detailed fabrication process is illustrated in Figure 4.5. First, microdisks were patterned and etched on an SOI wafer with a 350-nm-thick device layer. The edges of the disks were thinned down to 200 nm by time-controlled thermal oxidation. This allowed room for the microtoroids to expand in the vertical direction during hydrogen annealing. The sample was then partially released in buffered HF and annealed in 10-Torr hydrogen ambient at 1050°C for 5 minutes, creating a toroidal rim around the disks. The hydrogen annealing condition has been optimized for the formation of the microtoroids, as reported in [125-127]. A second SOI wafer with a 700-nm-thick device layer was thermally oxidized to create a SiO_2 spacer of 1 μm thickness. This is the initial spacing between the microtoroid and the waveguide couplers. This design is to ensure the initial coupling is negligible. After thermal oxidation, the thickness of the device layer was reduced to 250nm. This SOI wafer was then fusion-bonded to the wafer with the microtoroid pattern. And the substrate of the SOI wafer was subsequently removed to reveal the second SOI layer. The microtoroids were visible through the thin SOI layer, and the waveguides patterns were aligned to edges of the underneath microtoroids. As the last step, the waveguides around the toroids were released in buffered HF and supercritical dryer.

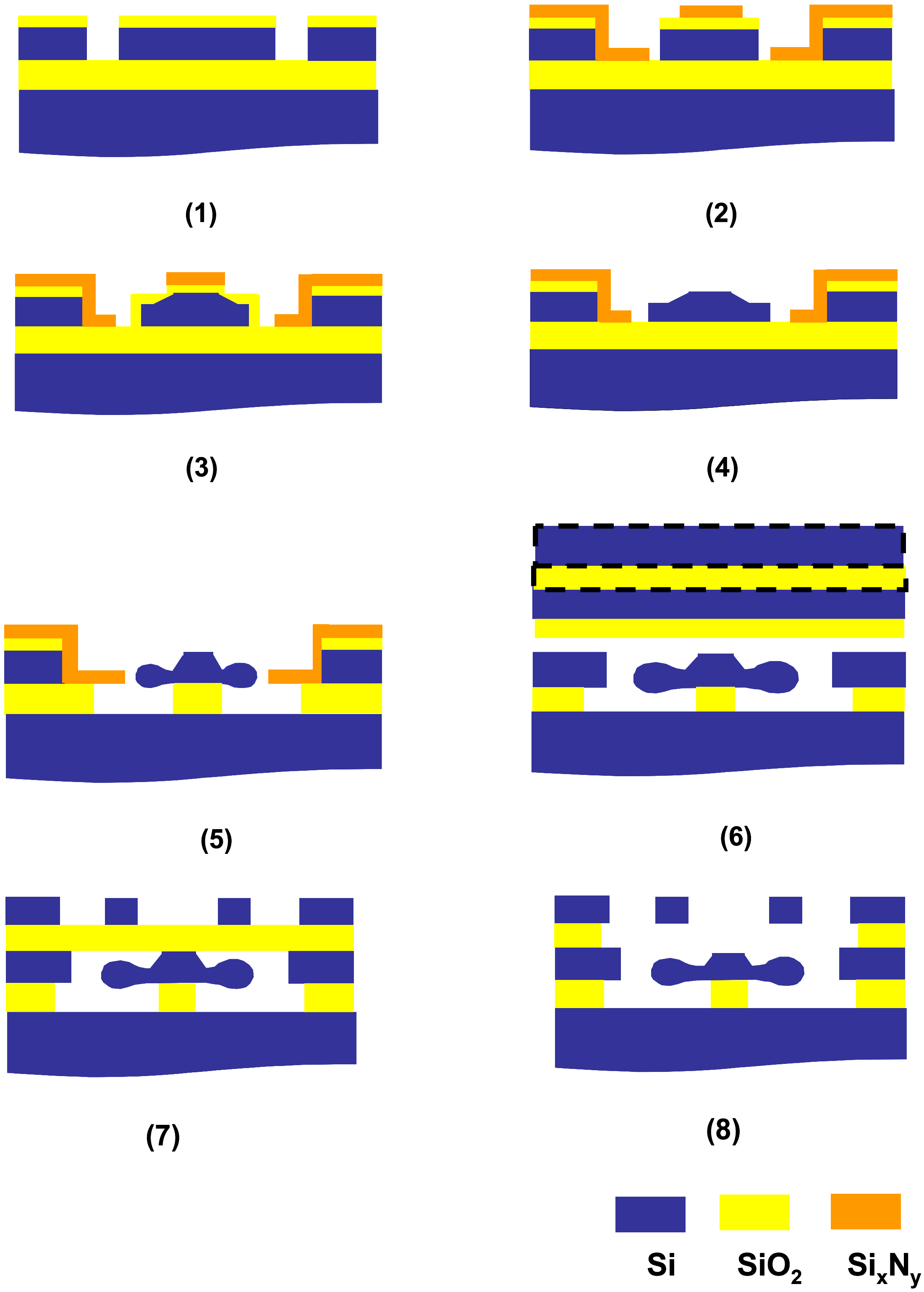

Figure 4.5 Optimized fabrication process flow for the integrated microtoroidal resonator.

4.3.2 Wafer Bonding Challenges and Process Optimization

To create the double SOI layer structure for our device, Si-SiO_2 bonding is a critical step. It is particularly challenging because the bottom wafer has already been patterned and has topology and voids. As discussed in the previous section, to maximize the bonding area and bonding strength, we have designed to only thin down the periphery of the microdisk and maintain the center as a post area. To prevent the center area from thermal oxidization, we have initially deposited an LPCVD silicon nitride layer and pattern it to cover the central area of the disk.

The cross-sectional profile of the oxidized structure simulated by TSprem4 is shown in Figure 4.6. It is verified that the center post area is sufficiently flat and suitable for bonding. The oxidation time is simulated using the Deal-Grove model [134], and further calibrated according to the experimental data to precisely control the final thickness of the device layers.

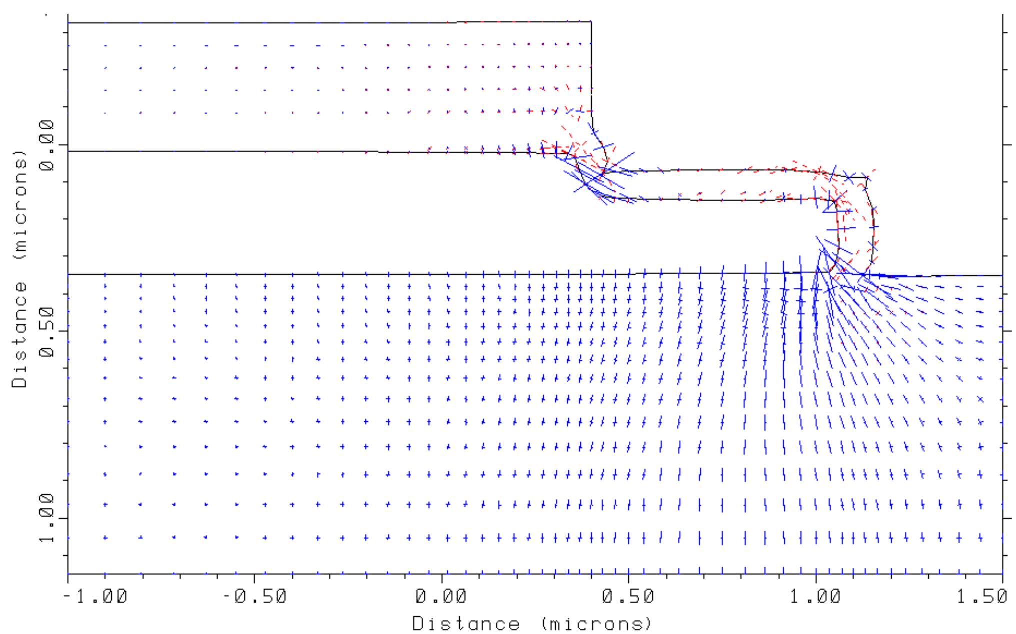

Figure 4.6 Simulated cross-sectional profile of the device after thermal oxidation.

However, if silicon nitride mask is directly covered the silicon surface, silicon nitride and silicon react at the interface when going through the hydrogen annealing process, resulting in an increase of the silicon surface roughness, as revealed in Figure 4.7. This leads to poor bonding quality for the subsequent Si-SiO_2 fusion bonding process.

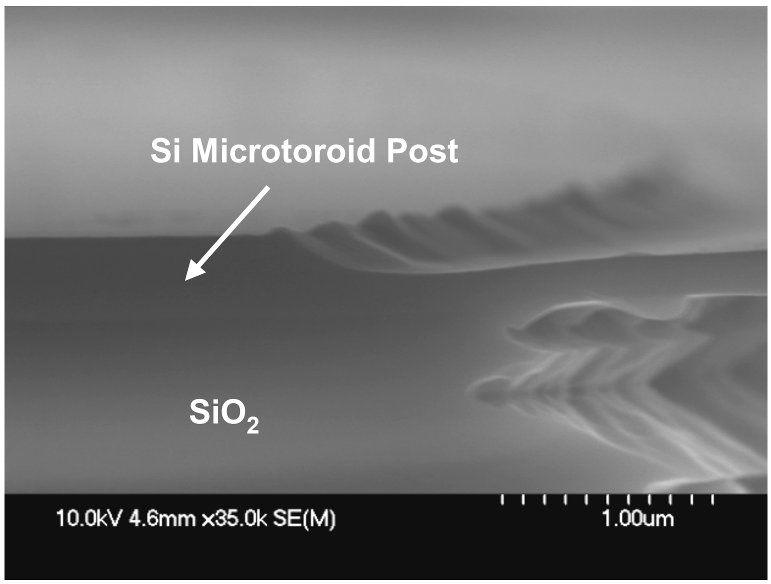

(a)

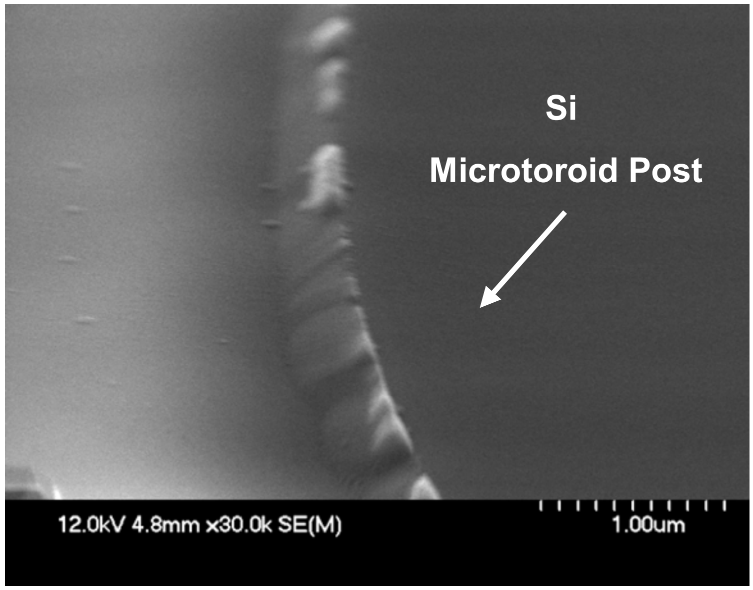

(b)

Figure 4.7 SEM micrographs of the silicon surface around the microtoroid post after silicon nitride was stripped. The surface roughness from the previous silicon nitride and silicon interface results in poor bonding quality. (a) Cross section view of the silicon surface at the microtoroid post area. (b) Top view of the silicon surface at the microtoroid post area.

To solve this problem, we have optimized the process by depositing a low temperature oxide (LTO) layer as the buffer layer between the silicon nitride mask and the silicon microtoroid post. This is compatible with the current process because this LTO layer is used as the mask to pattern the microtoroid base and the electrodes layer. Before the hydrogen annealing step, this buffer LTO layer was stripped using 10:1 buffered oxide etcher (BOE) solution. The exposed silicon layer is smooth, and shown a good bonding quality. Through-wafer infrared (IR) images provide a quick assessment of the bonding quality. Figure 4.8 shows the IR images of (a) a high quality bonding on a patterned substrate and (b) a poor bonding exhibiting trapped bubbles and voids.

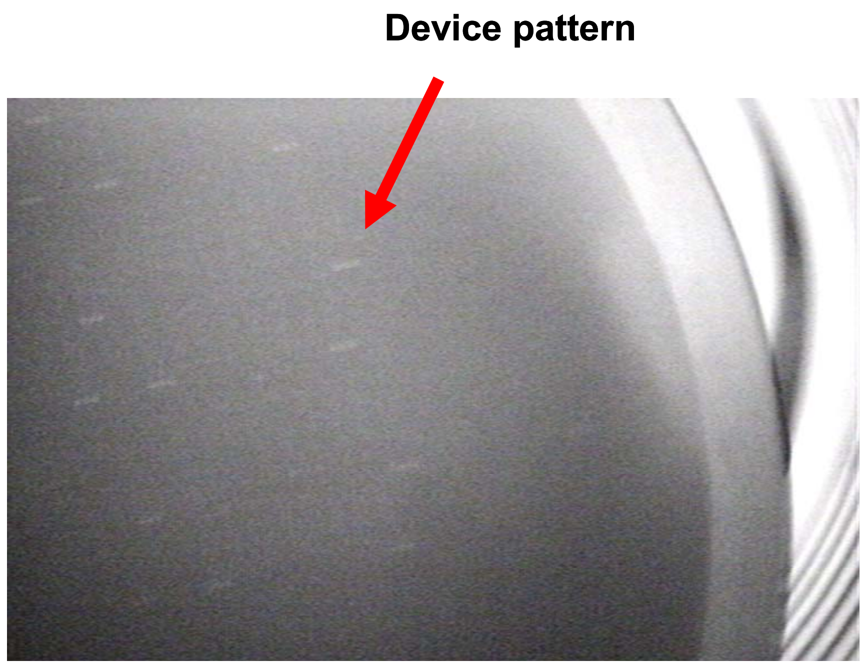

(a)

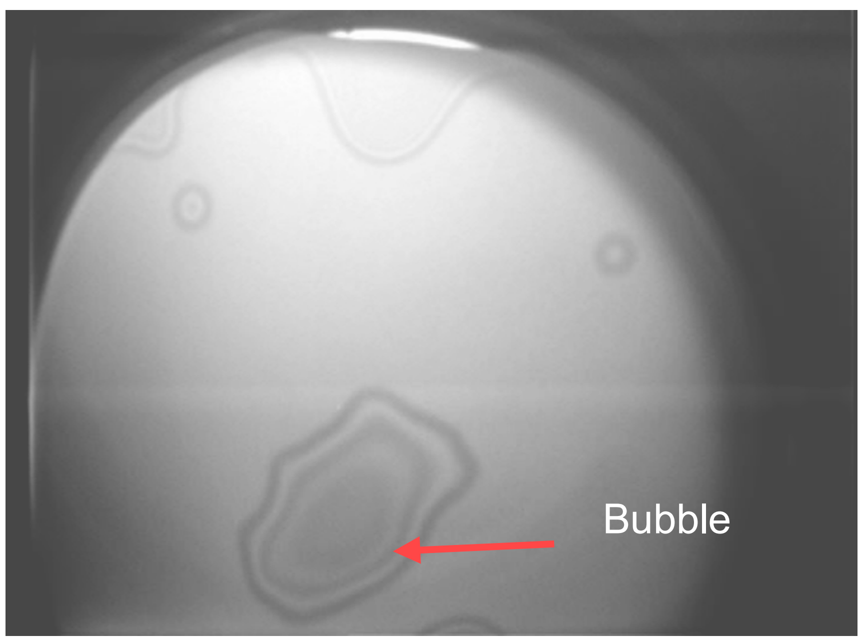

(b)

Figure 4.8 IR images of the bonded wafers (a) High quality bonding image on a patterned substrate. (b) Poor quality bonding exhibiting trapped bubbles and voids.

These inspection results were obtained by using our wafer bonding quality inspection set up. It is illustrated in Figure 4.9. This setup includes an infrared lamp (fiber illuminator), an infrared camera and a ring-shaped wafer holder to pass through the illumination light.

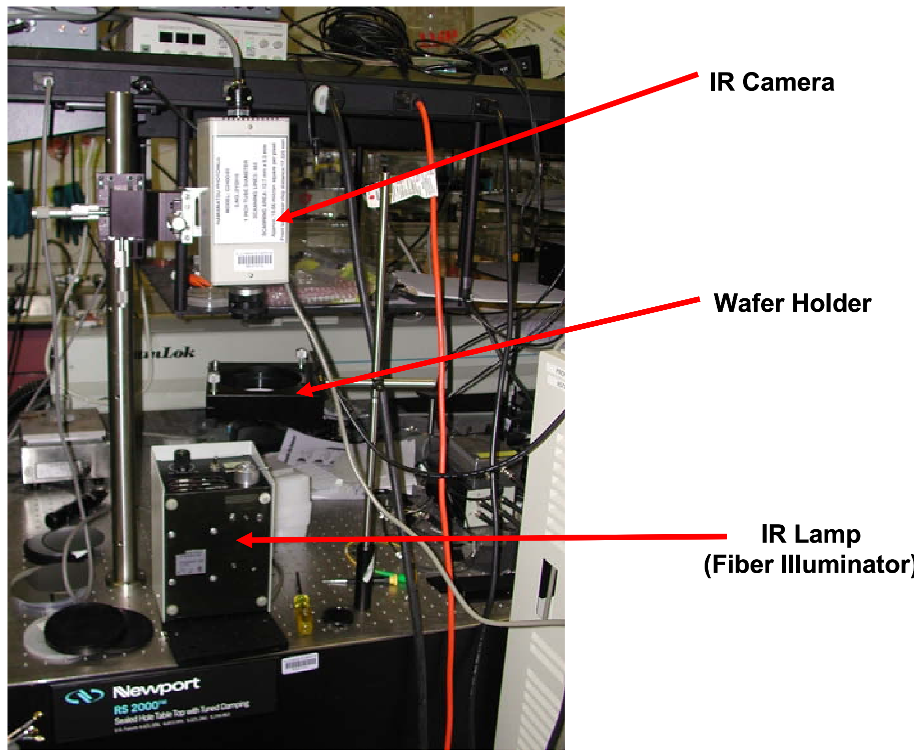

Figure 4.9 Wafer bonding inspection set up. It includes an IR lamp, an IR camera and a ring-shaped wafer holder to pass through the illumination light.

4.3.3 Critical Dimension (CD) Inspection and Assurance

To ensure the surrounding area is not affected by the hydrogen annealing process, the silicon nitride film and the LTO film are deposited onto a dummy mesa structure with a similar height of the device. Figure 4.10 shows the cross-sectional view of the SEM to inspect the step coverage. We can see that the corner protection is satisfactory with the LTO and the silicon nitride mask film layers.

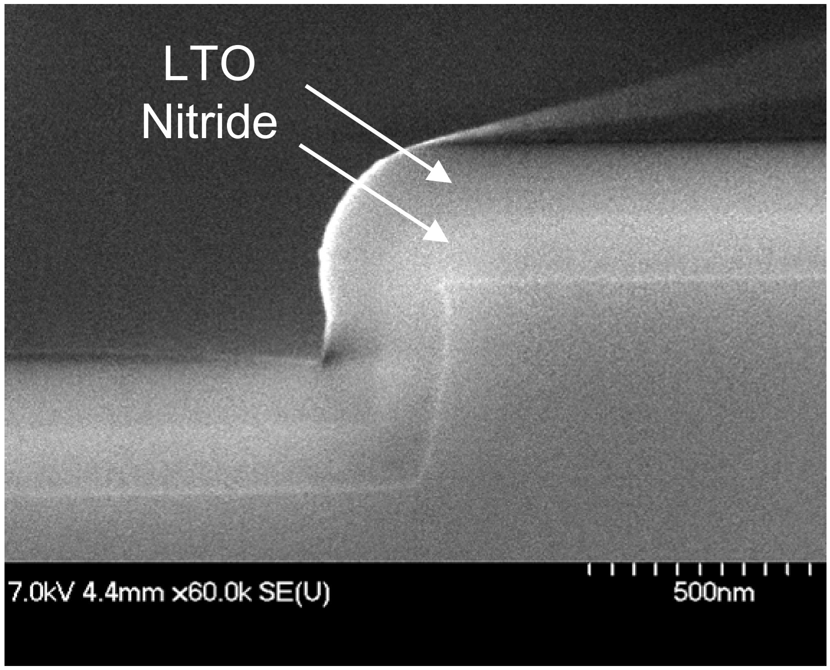

Figure 4.10 Cross-sectional view of a silicon mesa covered with silicon nitride and LTO films. The mesa top remains flat after hydrogen annealing process.

The Si/SiO_2 interface reacts during the hydrogen annealing process. If the optical field is exposed to the rough interface, the scattering loss will increase significantly. Thus it is necessary to segregate the optical field area from the rough edges. From the mode profile, it is estimated that a distance of 5 μm is sufficient to avoid light leakage to substrate or excessive scattering loss at the interface. Figure 4.11 shows the optical micrographs of the fabricated device, covered by the dielectric mask films. In Figure 4.11, (a) and (b) are before and after the hydrogen annealing process, respectively. The toroid edge formation is also observable from (a) to (b).

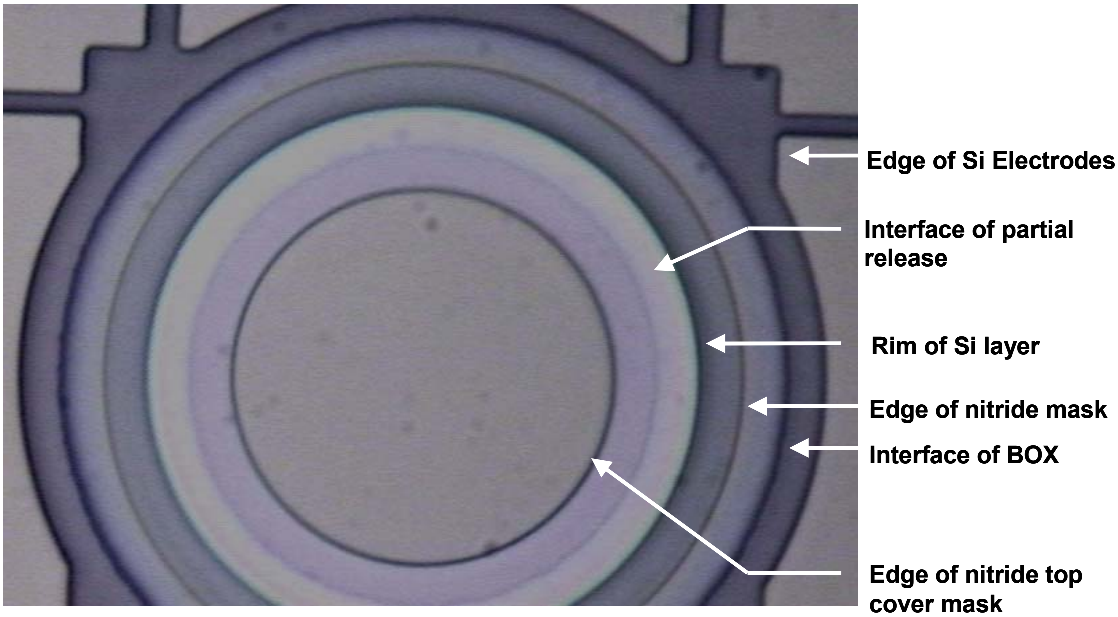

(a)

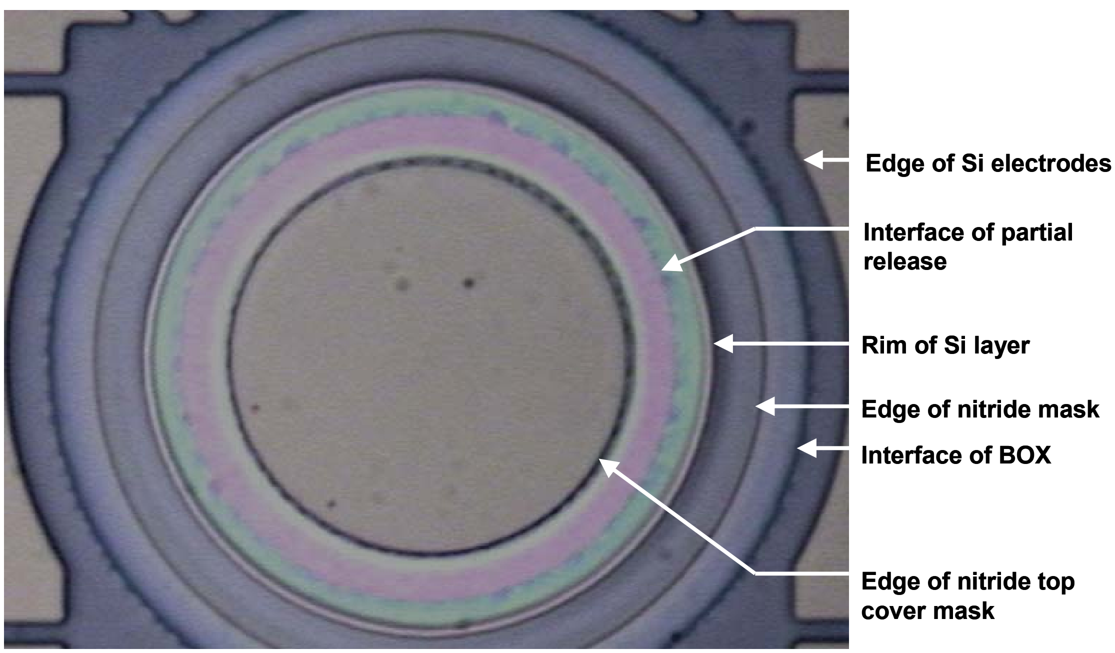

(b)

Figure 4.11 Top view optical micrographs of the microtoroidal resonator structure with the protection film layers (a) before and (b) after the hydrogen annealing process.

4.4 Analysis of Fabricated Device

The fabricated devices were inspected using optical microscopes and scanning electron micrograph (SEM). The SEM micrograph of the fabricated device is shown in Figure 4.12(a). The fabricated microtoroidal resonator has a ring radius of 19.5 µm and a toroidal radius of 200 nm. A higher magnification micrograph is shown in Figure 4.12(b). From the SEM pictures, the dimensions of the waveguides are measured to be 0.69 µm wide and 0.25 µm thick, very close to the designed parameters. Figure 4.12(c) and Figure 4.12(d) show the optical microscope images of the waveguides vertically aligned to the underneath microtoroid when focused on (a) the upper waveguide layer and (b) the bottom microtoroid, respectively.

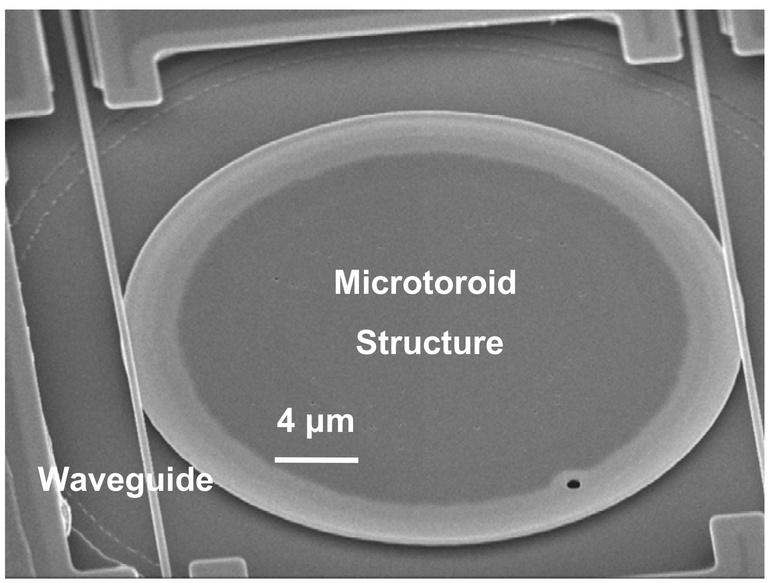

(a)

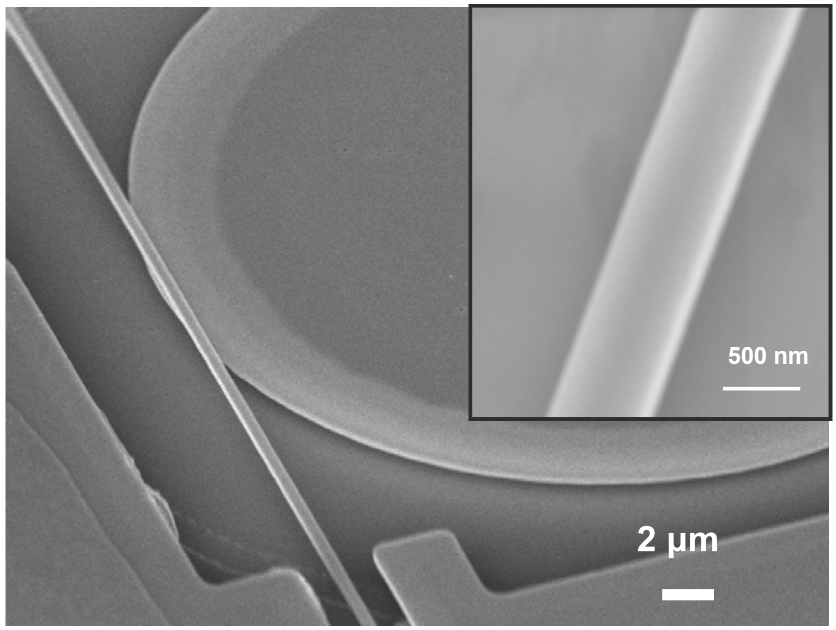

(b)

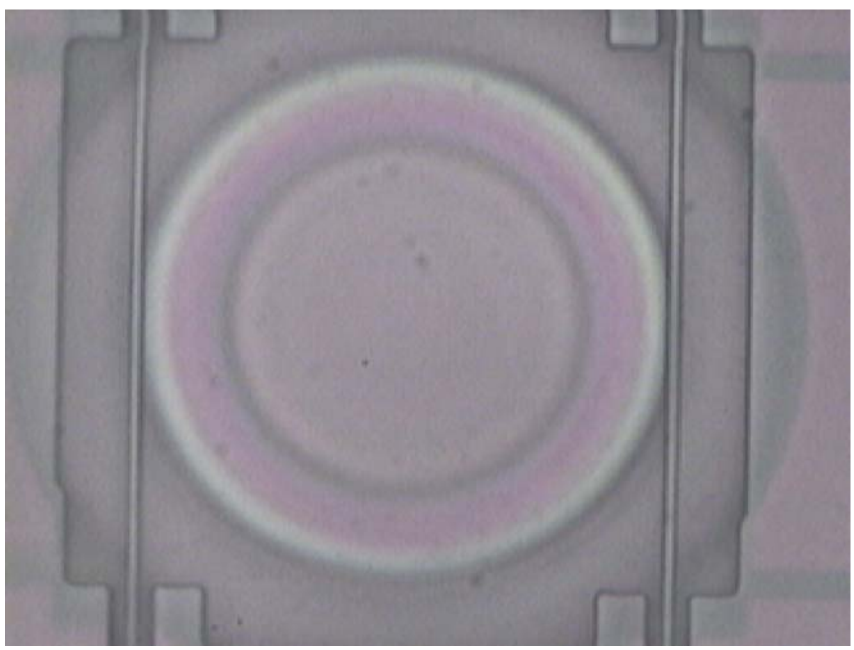

(c)

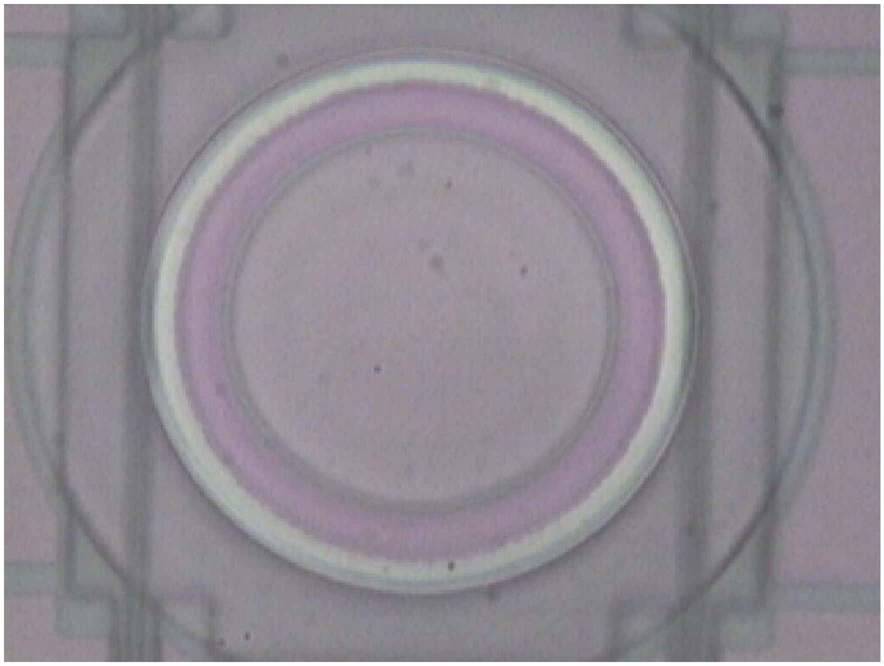

(d)

Figure 4.12 Fabricated device images (a) SEM micrograph of the microtoroidal resonator and the integrated waveguides. (b) Close-up SEM view of the waveguide aligned to the microtoroid. The inset shows top view of the waveguide. (c) Optical micrograph of the device when focused on the upper waveguide layer. (d) Optical micrograph of the device when focused on the bottom microtoroid layer.

The fabricated microtoroidal resonator exhibited a smooth sidewall, as shown in Figure 4.13. In addition to creating toroidal shape, the hydrogen annealing also reduced the surface roughness to < 0.26 nm root-mean-square (RMS), measured by atomic force microscope (AFM) [125], which is critical to attain high optical performance.

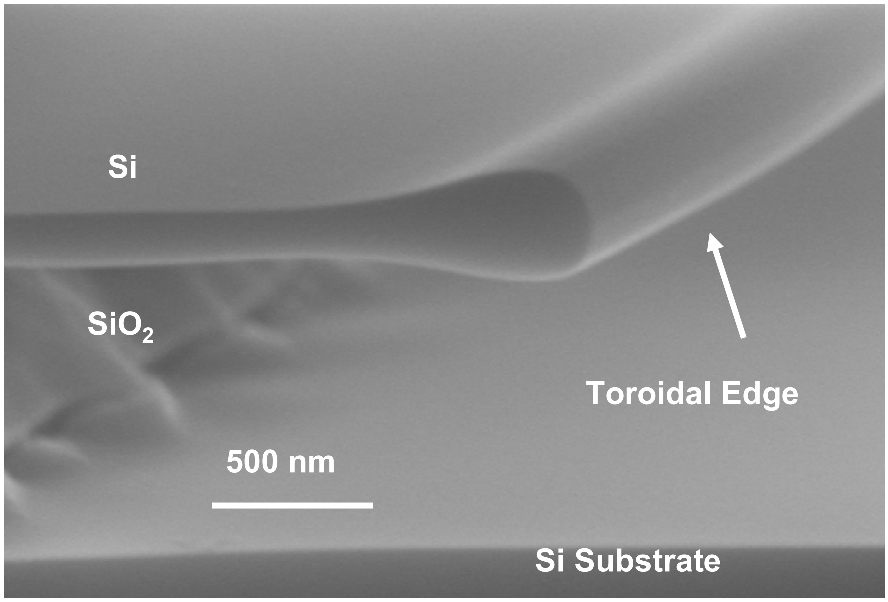

Figure 4.13 The SEM micrograph showing the toroidal edge formed after the hydrogen annealing process.

4.5 Summary

In this chapter, we have designed and optimized the process flow and successfully fabricated the tunable microtoroidal resonator with the integrated waveguides, combining the hydrogen annealing process and the wafer bonding technique.

To address the nonplanar topography induced by hydrogen annealing process, we have added a process to thin down only the edge of the microdisk and a passivation process to protect the surrounding area. Also, microtoroid edge retraction has been taken into consideration and alignment accuracy has been analyzed.

The optimized key fabrication processes are as follows: First, the pre-hydrogen-annealing structures are patterned in the bottom layer for the microtoroids and the electrodes of the MEMS actuators. Then the microdisk is partially released to expose the periphery area. Microtoroids are formed after the hydrogen annealing process. After bonding another SOI wafer to the microtoroid wafer and remove the substrate to reveal the second silicon layer, the waveguide couplers in this layer are patterned and aligned to the edges of the underneath microtoroids. The final step is to pattern and release the waveguides around the toroid to achieve MEMS actuation for the integrated device.

After the microtoroidal resonator was fabricated through the optimized process flow, the bonding quality and the critical dimensions of the device are inspected and ensured. The SEM micrographs of the fabricated microtoroidal resonator with the integrated waveguides have shown a good agreement with the design.

Chapter 5 Microtoroidal Resonators: Characterization

5.1 Experimental Setup Overview

The optical performance of the tunable microtoroidal resonator is tested using either a broadband amplified spontaneous emission (ASE) source (OpticWave Mini BLS-C-13) or a tunable laser (Agilent 81680A), as shown in the block diagram of Figure 5.1. Light is coupled to the waveguides by polarization-maintaining lensed fibers. A calibrated optical power meter (HP 8153A) and an optical spectrum analyzer (OSA) (ANDO AQ6317B) are placed at the output to measure the transmitted power. The ASE provides a broadband source for quick measurements over a wide spectral range, while the tunable laser is used for high-resolution characterization. We have used TE-polarized input, which is attained by a linear polarizer and a polarization controller.

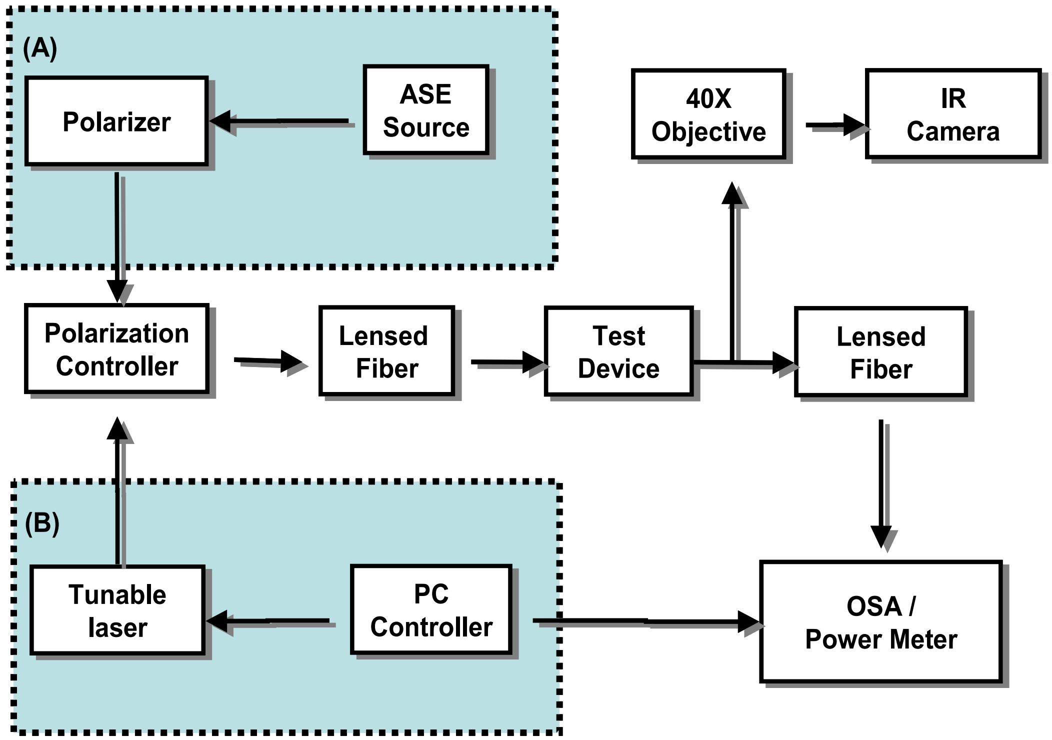

Figure 5.1 Experimental setup block diagram for the optical characterization of the integrated device. The amplified spontaneous emission (ASE) source is used for quick measurement of the spectral response as in (A), while the tunable laser provides high-resolution characterization measurement as in (B).

The photograph of the setup is shown in Figure 5.2. It includes the input and output stages, the piezoelectric transducer (PZT) controller, a microscope with up to 500 X magnification for observation, and the sample mount for testing. In Figure 5.2(b), the close-up view shows the input and output lensed fibers, the probes for MEMS actuation and a sample under test on the thermally stabilized mount.

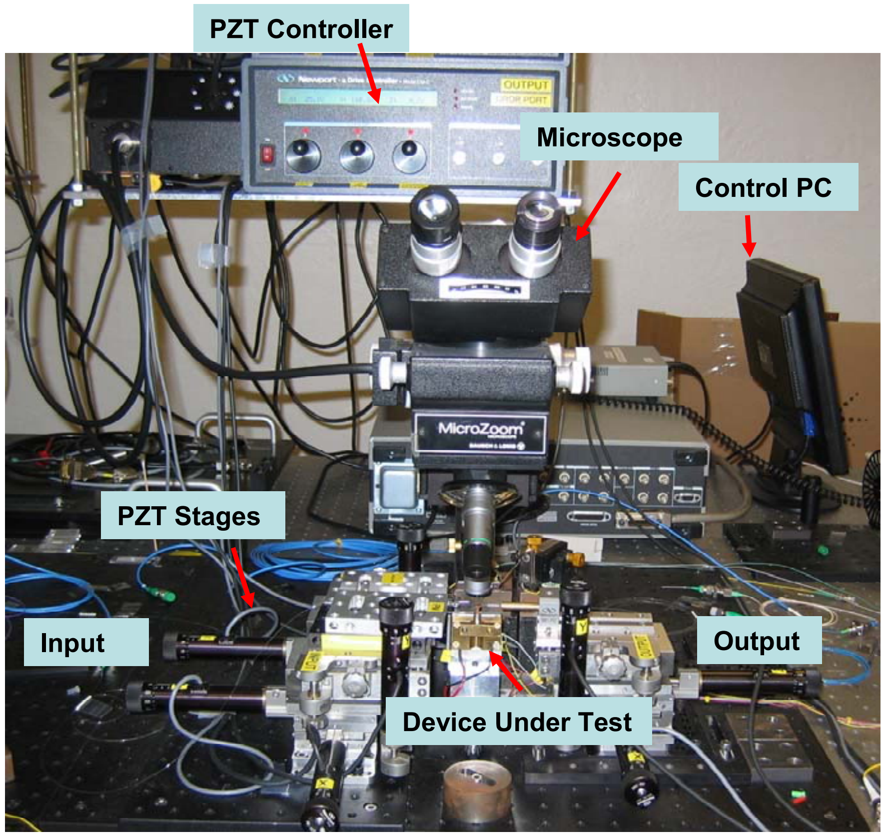
PZT Controller
Microscope
Control PC
MicroZoom
PZT Stages
Input
Output
Device Under Test

(a)

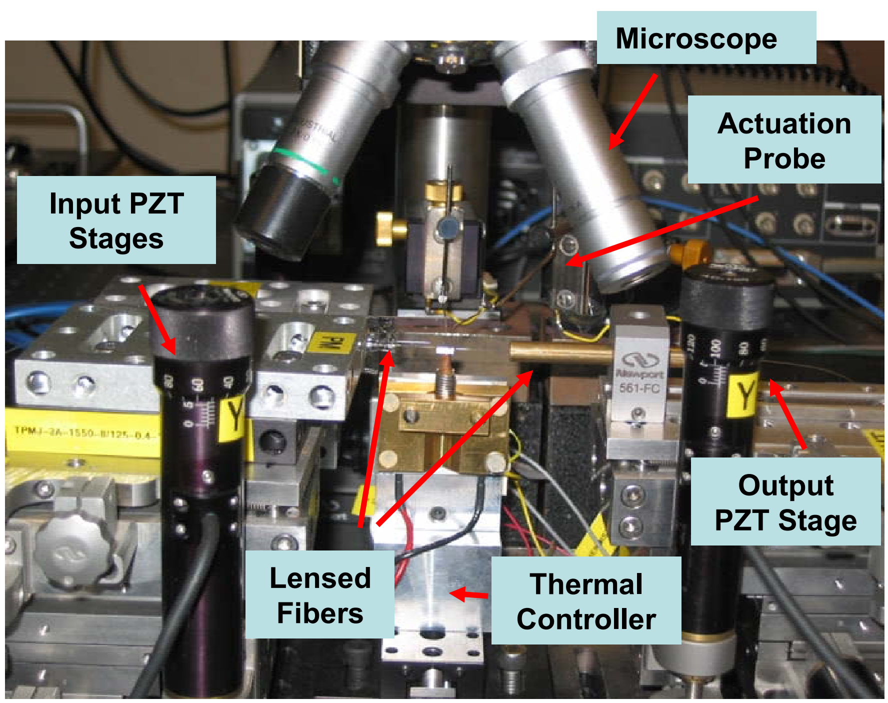
Microscope
Actuation Probe
Input PZT Stages
Output PZT Stage
Lensed Fibers
Thermal Controller

(b)

Figure 5.2 (a) Experimental setup for device characterization the integrated device spectrum measurement. (a) Overall view of the setup. It consists of an input and an output PZT stages, a PZT controller, a microscope with up to 500 X magnification for observation, and a central sample mount. (b) Close-up view showing the input and output lensed fibers, the probes for MEMS voltage actuation and a sample under test on the thermally stabilized mount.

5.2 Optical Performance Measurement

To actuate the waveguide, a bias voltage is applied to the fixed electrodes while the waveguide is grounded. At zero bias, almost 100% of the light is transmitted to the output port. With increasing bias, sharp dips gradually appear in the transmission spectrum, as shown in Figure 5.3. Each dip in the raw spectra of Figure 5.3(a) corresponds to a resonance wavelength. The free spectral range (FSR) of the TE mode is measured to be 5.15 nm. The small ripples are due to the reflections from the cleaved facets (Fabry-Perot effect). They can be eliminated by anti-reflection coating the facets, as will be shown in later analysis. Comparing with the microdisk resonator case, only one resonance peak is observed within each FSR, confirming the successful suppression of multiple radial modes observed in microdisk resonators.

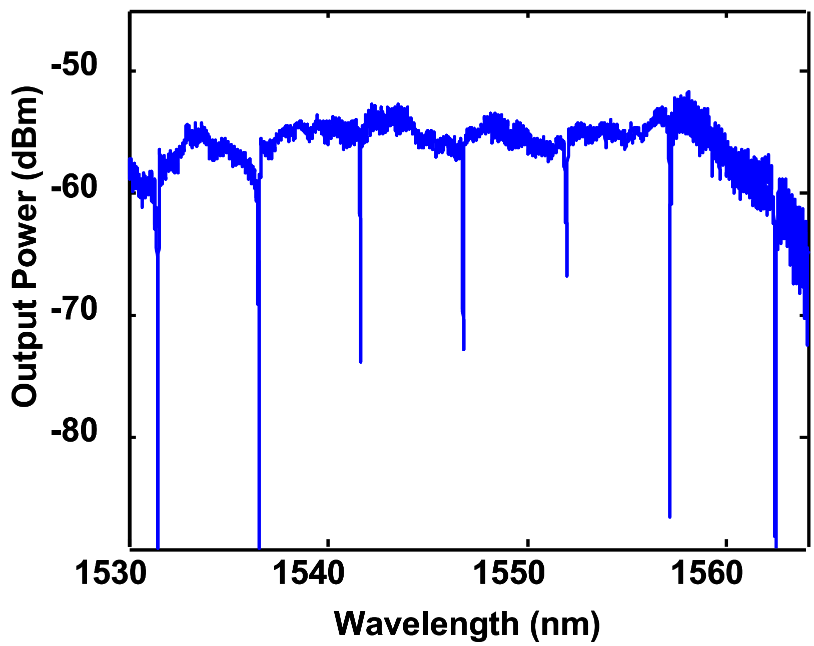

-50
-60
-70
-80
Output Power (dBm)
1530
1540
1550
1560
Wavelength (nm)

(a)

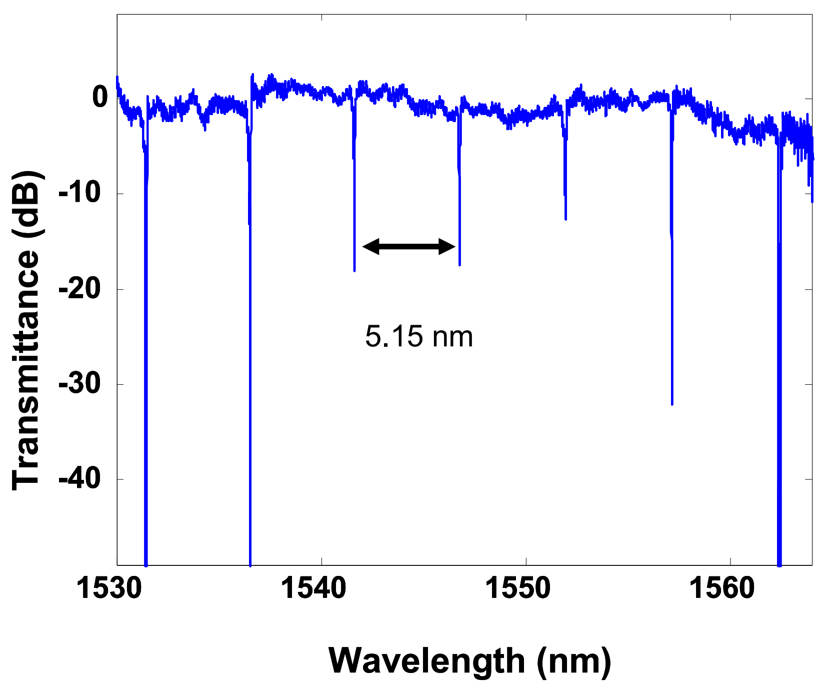

0
-10
-20
-30
-40
Transmittance (dB)
5.15 nm
1530
1540
1550
1560
Wavelength (nm)

(b)

Figure 5.3 Measured optical spectra of a microtoroidal resonator at a bias voltage of 67V. (a) Raw data of output spectrum (b) Spectrum normalized to that of a straight waveguide without coupling. The measured free spectral range (FSR) of the TE mode is 5.15 nm.

The integrated tunable coupler enables the microresonator to operate in all coupling regimes. At low voltage, the microresonator is under-coupled. Figure 5.4 shows the normalized transmission spectra of the resonator around one of the resonant wavelengths at 1548.2 nm at bias voltages of 51.0, 56.0, and 64.8V. As the voltage increases, the optical coupling becomes stronger, leading to a larger dip at resonance. The three coupling regimes are clearly visible in Figure 5.5, which plots the normalized transmittance at the resonant wavelength as a function of the applied voltage. In the under-coupling regime (V_{bias} < 114V), the transmittance decreases continuously with increasing voltage. The transmittance reaches a minimum at critical coupling (V_{bias} = 114V). The extinction ratio is measured to be 22.4 dB at critical coupling. Further increase in voltage move the resonator into the over-coupling regime. The increase in transmittance is accompanied by a broadening of the resonance linewidth since the coupling to waveguide is now stronger than the intrinsic loss of the resonator.

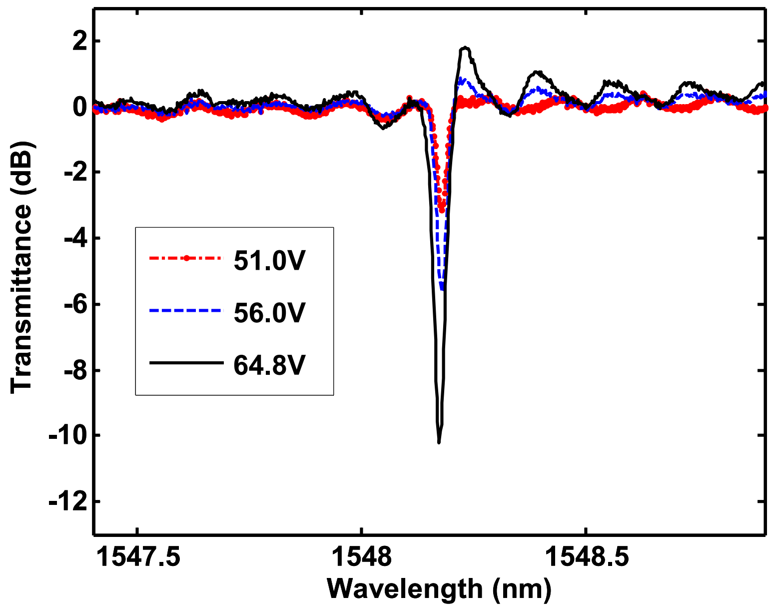

Figure 5.4 Normalized optical spectra of a microtoroidal resonator at bias voltages of 51.0, 56.0, and 64.8V.

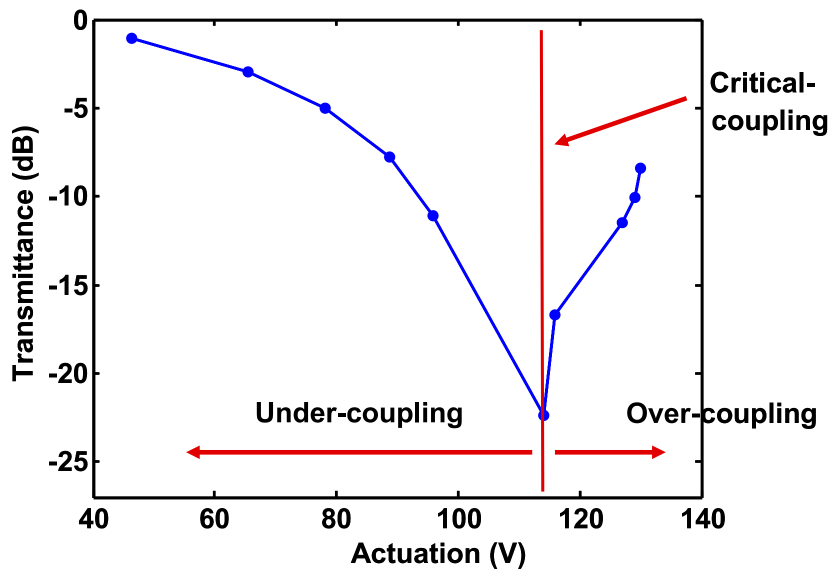

Figure 5.5 Normalized transmittance at resonance versus actuation voltage. The three coupling regimes are indicated in the plot. Transmittance change shows that the microresonator is continuously tunable from under-coupling to over-coupling regimes.

5.3 Analysis and Modeling of Experimental Characterization

Following the previous theoretically analysis in Chapter 2, the optical transfer function of the microresonator can be expressed as a function of resonant frequency (ω_0) and amplitude decay time constants, τ_0 and τ_e, due to intrinsic loss and external coupling, respectively:

$$t_{res} = \frac{j(\omega - \omega_0) + \frac{1}{\tau_0} - \frac{1}{\tau_e}}{j(\omega - \omega_0) + \frac{1}{\tau_0} + \frac{1}{\tau_e}} \tag{5.1}$$

where t_{res} is the transfer function of the microresonator.

Alternatively, the transfer function can also be expressed in terms of the unloaded quality factor, Q_0, and the external quality factor, Q_e:

$$t_{res} = \frac{2j\left(\frac{\lambda_0 - \lambda}{\lambda}\right) + \left(\frac{2}{Q_0} - \frac{1}{Q_L}\right)}{2j\left(\frac{\lambda_0 - \lambda}{\lambda}\right) + \left(\frac{1}{Q_L}\right)} \tag{5.2}$$

where $Q_0 = \omega_0 \cdot \tau_0 / 2$, $Q_e = \omega_0 \cdot \tau_e / 2$, and the loaded quality factor Q_L is defined as

$$\frac{1}{Q_L} = \frac{1}{Q_0} + \frac{1}{Q_e} \tag{5.3}$$

The measured spectra are usually complicated by the Fabry-Perot resonance between the two cleaved facets, as illustrated in Figure 5.7 to Figure 5.9. To more precisely model the measured spectrum, and more accurately extract the Q values of the resonator, particularly when the resonance peak is small, we develop a comprehensive model here that includes both the effects of the microresonator and the FP ripples.

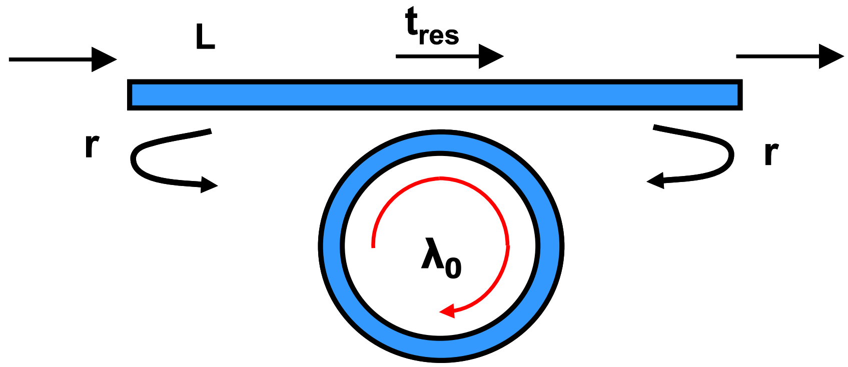

Figure 5.6 Schematics illustrating the interaction between the microresonator and the Fabry-Perot resonance of the coupling waveguide.

The total transmission t_{tot} is now a summation of multiple transmissions through the waveguide, as shown in Equation **Error! Reference source not found.**:

$$\begin{aligned} t_{tot} &= (1-r)^2 \cdot \exp(-\alpha L) \cdot \exp\left(jkLn_{eff}\right) \cdot t_{res} \\ &+ (1-r)^2 \cdot r^2 \cdot \exp(-3\alpha L) \cdot \exp\left(j(3kLn_{eff} + 2\phi_R)\right) \cdot t_{res}^3 \\ &+ (1-r)^2 \cdot r^4 \cdot \exp(-5\alpha L) \cdot \exp\left(j(5kLn_{eff} + 4\phi_R)\right) \cdot t_{res}^5 \\ &+ \cdots \end{aligned} \tag{5.4}$$

where r is the amplitude reflection coefficient at the facet of the silicon waveguide, α is the optical loss per unit length in the waveguide, L is the length of the waveguide, k is the free-space propagation constant, n_{eff} is the effective refractive index of the Si waveguide, and ϕ_R is the optical phase change at the reflection per interface. Since there is a zero phase shift at the reflection interface due to refractive index difference, the total transmission t_{tot} can be simplified to:

$$
\begin{aligned}
t_{tot} = &(1-r)^2 \cdot \exp(-\alpha L) \cdot \exp\left(jkLn_{eff}\right) \cdot t_{res} \cdot \\
&\left\{1 + r^2 \cdot \exp(-2\alpha L) \cdot \exp\left(j2kLn_{eff}\right) \cdot t_{res}^2 \right. \\
&\left. + r^4 \cdot \exp(-4\alpha L) \cdot \exp\left(j4kLn_{eff}\right) \cdot t_{res}^4 + \cdots \right\} \\
&= a_0\left(1 + q + q^2 + q^3 + \cdots\right) \\
&= \frac{a_0}{1-q}
\end{aligned}
\tag{5.5}
$$

where $a_0 = (1-r)^2 \cdot \exp(-\alpha L) \cdot \exp\left(jkLn_{eff}\right) \cdot t_{res}$, and $q = r^2 \cdot \exp(-2\alpha L) \cdot \exp\left(j2kLn_{eff}\right) \cdot t_{res}^2$

In this derivation, we have assumed the backscattering effect is small and can be neglected. Thus the total intensity transmittance is then given by

$$
T_{res} = \left|t_{tot}\right|^2 \tag{5.6}
$$

To include the effect of waveguide dispersion, the phase factor kLn_{eff} is replaced by

$$
\begin{aligned}
\phi &= kL\left[n_{eff} + \frac{dn}{d\lambda}(\lambda - \lambda_0)\right] \\
&= kLn_{eff}\left[1 + \frac{dn}{d\lambda}\frac{1}{n_{eff}}(\lambda - \lambda_0)\right] \\
&= kLn_{eff}\left[1 + D_\lambda(\lambda - \lambda_0)\right]
\end{aligned}
\tag{5.7}
$$

where $D_\lambda = \dfrac{dn}{d\lambda}\dfrac{1}{n_{eff}}$.

The quality factors, Q_0 and Q_L, are extracted from the measured optical spectra by least-mean-square-error fitting to the model. Figure 5.7 shows the measured and the fitted spectra around the resonance peak at 1548.2 nm when the resonator is (a) decoupled, (b) under-coupled, and (c) over-coupled. The experimental data agree very well with the theoretical model. From the fitted spectral response, the unloaded quality factor, Q_0, of the microtoroidal resonator is extracted to be 110,000. The loaded Q, Q_L, is continuously tunable from 110,000 to 5,400, exhibiting a tuning ratio of more than 20:1.

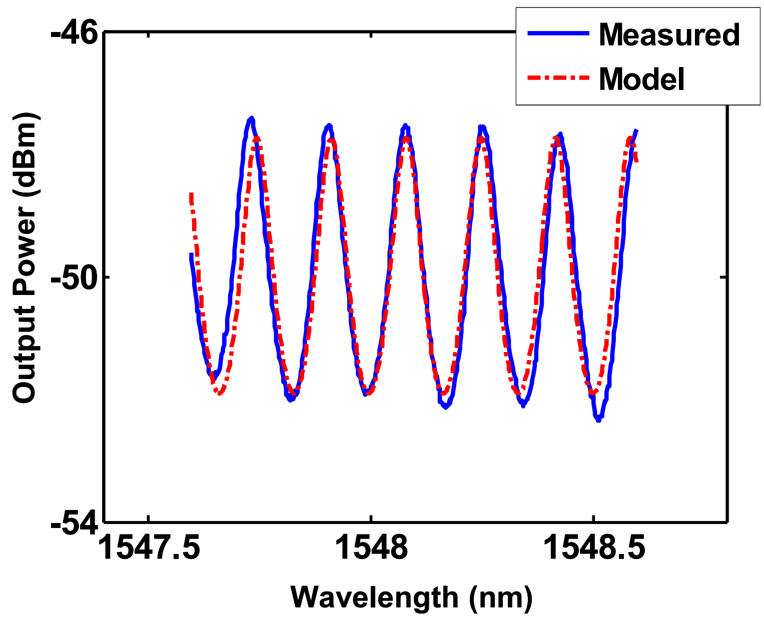

Figure 5.7 Measured and modeled spectra at 0V (microresonator is decoupled).

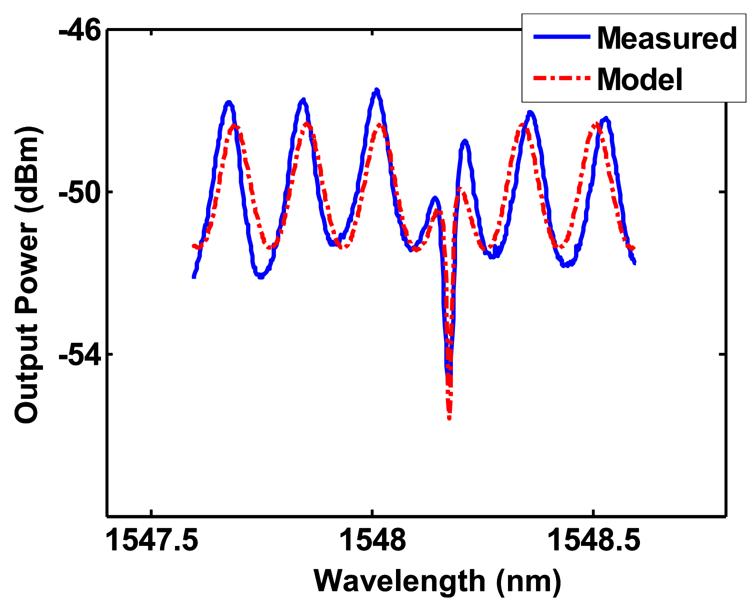

Figure 5.8 Measured and modeled spectra at 64.8V (microresonator is under-coupled).

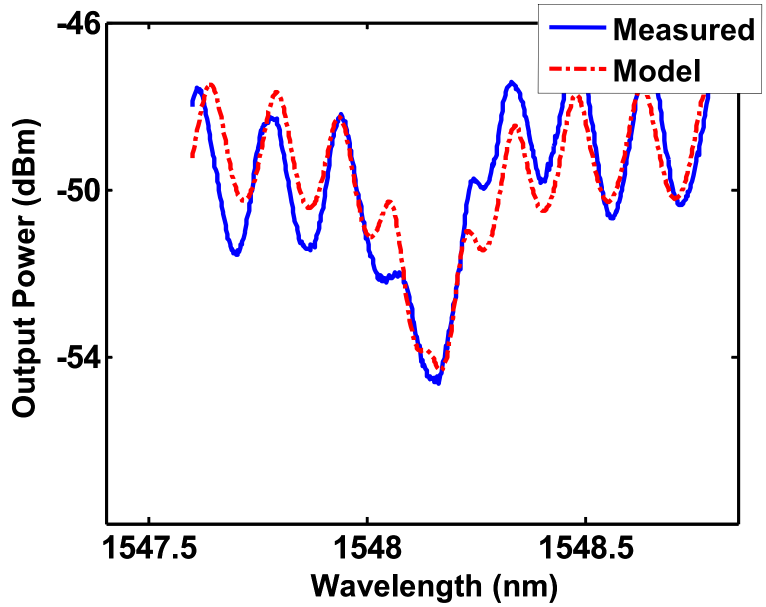

Figure 5.9 Measured and modeled spectra at 130V (microresonator is over-coupled).

The model described in this paper not only fit the resonance peak but also the ripples due to Fabry-Perot resonance. When the resonance peak is small, the quality factor extracted using this method is more accurate than using the lumped resonator model alone [135].

5.4 Discussion

Hydrogen annealing is a simple and powerful technique to fabricate suspended microring resonators with high quality factor and single radial mode. Compared with the etched ring with tethered anchor [136], the seamless toroidal structure has lower scattering loss and higher Q. The hydrogen annealing process also greatly reduces the surface roughness, as confirmed by the high Q measured in our devices. These tunable microresonators described in this paper can be cascaded to form reconfigurable optical add-drop multiplexers, wavelength-selective switches and crossconnects. It can also be used for bandwidth-tunable filters in dynamic optical networks. With the successful suppression of multiple radial modes, we expect the microtoroidal resonator to have even larger bandwidth tuning range than the microdisk-based tunable filters in [137].

5.5 Summary

In this chapter, we have experimentally characterized the single crystalline silicon microtoroidal resonator with MEMS-actuated tunable optical coupler. Using a broadband amplified spontaneous emission (ASE) source and a tunable laser, light is coupled into and out of the integrated device sample by polarization-maintaining lensed fibers. We have measured the transmitted power and spectra using a calibrated optical power meter and an optical spectrum analyzer (OSA). We have achieved an unloaded Q of 110,000 for this 39-μm-diameter resonator with a toroidal radius of 200 nm. The device is able to operate in all three coupling regimes: under-, critical, and over-coupling. The resonator can also be decoupled from the waveguide, which has the potential applications to allow them to be cascaded without loading the waveguides. The extinction ratio is measured to be 22.4 dB at critical coupling. In this chapter, we have also developed a detailed model combining the time-domain coupling theory with the Fabry-Perot resonance of the waveguide. The experimental and the theoretical results agree very well. The loaded Q is continuously tunable from 110,000 to 5,400. This device has potential applications in variable-bandwidth filters, reconfigurable add-drop multiplexers, wavelength-selective switches and crossconnects, and optical sensors.

Chapter 6 Microtoroidal Resonators Applications

6.1 Applications Overview

In many photonic integrated applications, optical microresonators can serve as basic optical functional blocks for various optical functions. Table 6.1 listed here shows a selection of applications for microresonators with various materials, including silicon, silica and compound semiconductors.

Author(s)	Application Area	Year	material
Little, et al.[3-5] Madsen, et al. [2]	filter	1997	silica
Lens, et al. [10] Madsen, et al. [11] Lee, et al. [99, 138]	dispersion compensators	1998	PLC silicon
Xu, et al. [7]	modulator	2003	silicon
von Klitzing, et al.[16, 17]	CQED	2001	fused silica
Kippenberg, et al. [15, 139]	nonlinear optics	2004	silica
Vollmer, et al.[18] Armani, et al. [19] White, et al. [140]	Optical sensor	2003	Silica
Choi, et al. [20, 22]	laser source	2003	InP

Table 6.1 List of various applications for microresonators. The years in the table is the earliest publication date of the cited papers.

Optical microresonators are good candidates for sensing applications. Recently there has been an intensive investigation utilizing microresonators for bio-sensing or chemical sensing applications. Optical microresonator-based biosensors are transducers that detect the presence of molecules at the surface of the resonator cavities. Surface functionalizations such as antibodies or oligonucleotide strands provide specificity for the targeted analytes, and the characteristic perturbation of the sensor such as the resonant peak shift can be used to detect those molecules bound to the surface. Transduction mechanisms for bound analytes include fluorescence, change in index of refraction [141] or absorption [19], or mass change in the evanescent region [142]. Because of resonance, compare to conventional sensors with straight waveguides, microcavities offer an enhancement of the measured response. So they have higher sensitivity for detecting molecules, which can be down to subfemtomole range [140], while typical sensitivity of evanescent wave biosensors based on fiberoptic or planar waveguide sensors is in the range of nanomole (nM) to picomole (pM). Also, microresonator-based sensing systems are nondestructive sensing to the samples. These advantages make microresonator-based sensors desirable for chemical and biological molecules detection.

Another important application area of microresonators is dynamic wavelength-division-multiplexing (WDM) networks. Tunable optical filters are key components in smart WDM networks. Wavelength-tunable filters can add, drop, switch, or block selected wavelength channels. Filters with tunable bandwidth are useful in dynamic bandwidth allocation for optimal spectral efficiency and in optical performance monitoring. Bandwidth-tunable filters have been demonstrated using mechanically stretched fiber Bragg gratings [143] and MEMS micromirror-based Gires-Tournois interferometer [144]. However, they are bulky and can not be easily integrated.

Microresonators have been widely studied for various filtering functions [5]. Here we first describe a dynamic add/drop filter based on a microdisk resonator [137]. System level functions such as matched filtering, dynamic channel banding, and wavelength demultiplexing have been demonstrated [90]. However, the lack of radial mode control in microdisk resonators limits the maximum tuning range due to excitation of high-order modes. We have further realized a reconfigurable and bandwidth-tunable add-drop filter with a large tuning range using a single-crystalline silicon microtoroidal resonator. Microtoroidal resonators offer tighter optical confinement and eliminate multiple radial modes observed in the microdisks. A full-width at half-maximum (FWHM) bandwidth tuning range of 2.8 GHz to 78.4 GHz has been achieved.

6.2 Wavelength Tunability Demonstration

6.2.1 Design, Fabrication, and Measurement

The tunable filter demonstrated here consists of a high-Q microdisk resonator, an input and an output deformable waveguides, and a microheater, as shown in Figure 6.1. The waveguide is suspended around the microdisk. Upon actuation, the waveguide is deformed and attracted towards the microdisk, changing the power coupling ratio. The microheater is integrated in the vicinity of the microdisk to control the resonant wavelength.

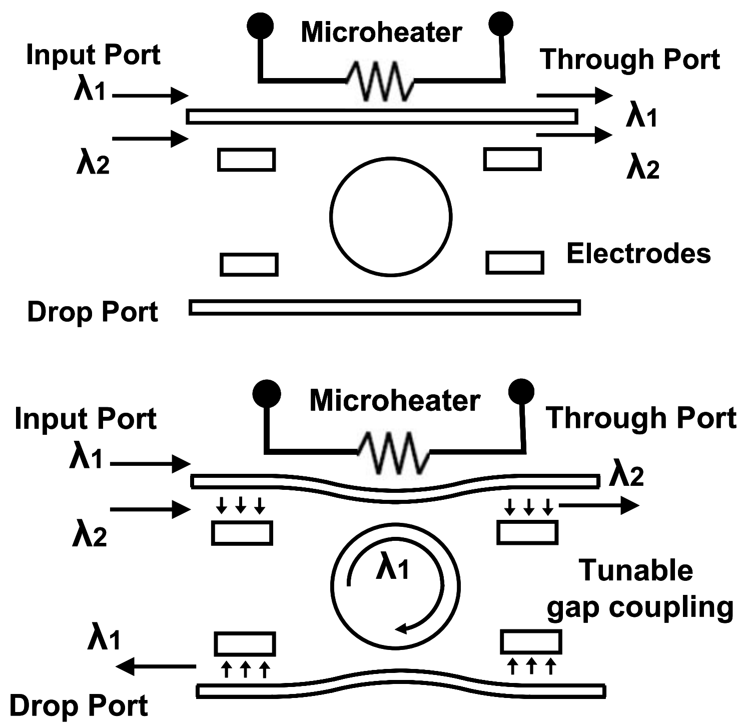

Figure 6.1 Schematic of the microdisk resonator tunable filter. By varying the gap spacing of microdisk and the waveguides, resonant wavelengths (e.g. λ_1 shown in the schematic) coupled to the drop port can be tunable.

Thermo-optic effect has been extensively used in planar lightwave circuits (PLCs) [4]. The thermal optic coefficient of Si (1.8×10^{-4} /ºC at room temperature for 1.55 μm wavelength range [145]) is ten times larger than glass, making it more efficient to tune the resonant wavelength by integrated microheaters.

The tunable filter comprises a fixed microdisk with 20 μm radius and two vertically-coupled deformable optical waveguides with 0.8 μm width. The waveguides are aligned to the edge of the microdisk. Both the microdisk and the waveguides are made in 0.25-μm-thick single crystalline silicon. The device is fabricated by thermally bonding two silicon-on-insulator (SOI) wafers with a 1-μm-thick silicon oxide in between, similar to the process step for making microtoroidal resonators described earlier. The optical waveguide is fabricated on the top SOI layer, and the microdisk and the electrodes for electrostatic actuators are fabricated on the bottom SOI layer. The waveguides around the microdisk are suspended by selectively removing the oxide underneath the waveguides.

The electrostatic actuator functions as a vertical comb-drive actuator with one movable finger and two fixed comb fingers. This design avoids the pull-in instability and permits the waveguide to be pulled down continuously from an initial gap spacing of 1 μm to almost touching. It has also employed the hydrogen-assisted annealing process we introduced in Chapter 3 to reduce the sidewall roughness. A 2-μm wide, 3.4-mm long Cr/Pt serpentine wire heater is patterned by lift-off process in the vicinity of the microdisk. The scanning electron micrograph (SEM) of the fabricated device is shown in Figure 6.2(a). An optical micrograph of the entire device including the integrated microheater is shown in Figure 6.2(b).

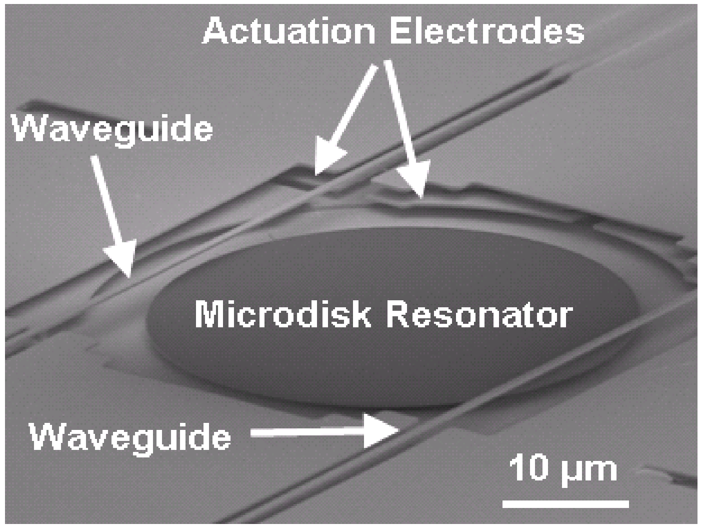

(a)

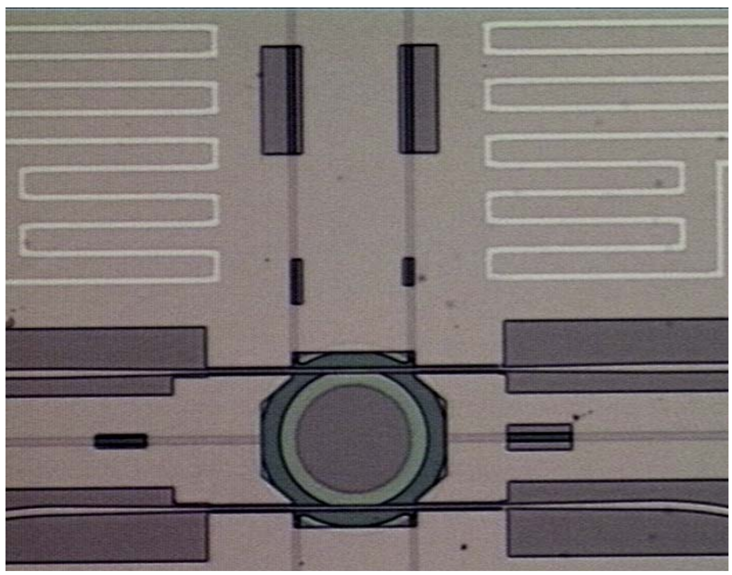

(b)

Figure 6.2 (a) SEM picture of a fabricated vertically-coupled microdisk resonator. (b) Top-view optical micrograph of the device with the integrated Cr/Pt serpentine wire microheater at the vicinity of the microdisk.

6.2.2 Measurement Results and Discussion

To demonstrate tunable bandwidth in our device, we actuated both waveguides and measured the spectral response of the drop port when varying the actuation biases.

Figure 6.3 shows the transmission spectra at the drop port for various power coupling ratios. When controlling the actuation voltages of input and drop waveguide to be 60.0V and 64.3V, the full-width at half-maximum (FWHM) bandwidth is 12.0 GHz, shown as curve (a). At the voltages of 62.6V and 67.5V, the bandwidth increases to 18.1 GHz, shown as curve (b). At 67.0 V and 74.0 V, the bandwidth increases to 41.2 GHz, shown as curve (c). These results indicate that a bandwidth-tunable optical filter can be realized.

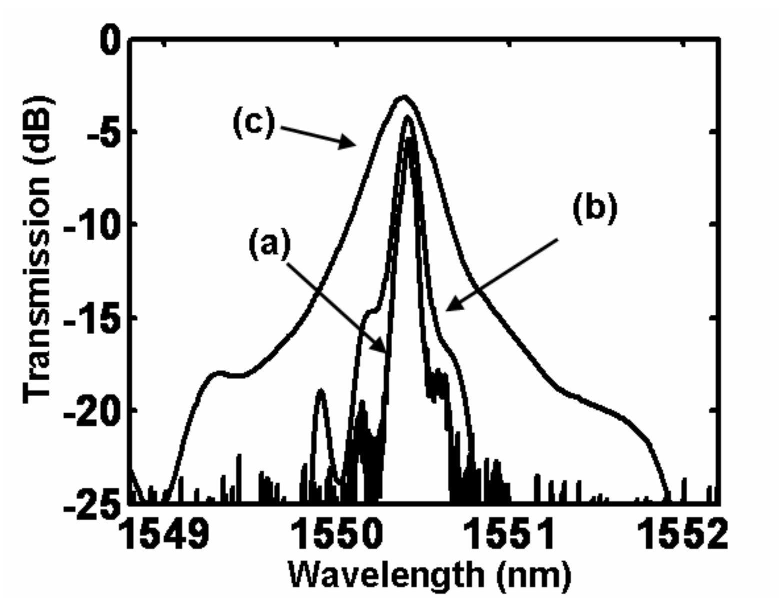

Figure 6.3 The measured spectral response at the drop port of the microdisk resonator filter with three different actuation bias conditions.

By applying current to the on-chip microheater, tuning of the resonant wavelength was also successfully demonstrated. With ambient environment at room temperature

25°C, applying a heater current of 1.7 mA yielded a red shift of 0.3 nm for the resonant wavelength. Figure 6.4 shows the transmission spectra at the through port for four heater currents: (a) 0 mA, (b) 1.7 mA, (c) 3.1 mA, and (d) 3.7 mA. Over 1 nm tuning range (125 GHz) has been achieved. The extinction ratio remains the same throughout the tuning process.

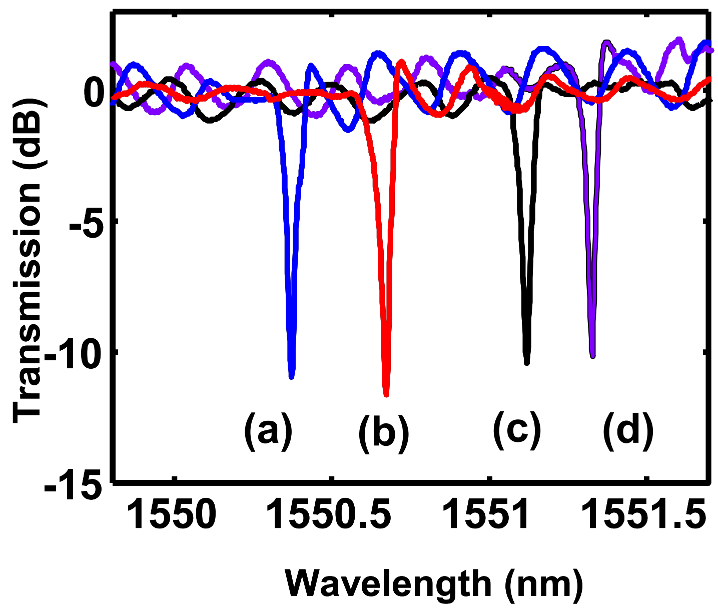

Figure 6.4 Measured Spectra at the through port with different currents applied through on-chip microheater.

The Free Spectrum Ranges (FSRs) of our fabricated device are 5.1 nm for TE mode and 3.7 nm for TM mode, which are also verified by numerical simulation of the 20 μm-radius microdisk.

The FWHM bandwidth is continuously tunable from 12 to 41.2 GHz, while the peak resonant wavelength is tunable over 125 GHz. This type of versatile tunable filters has extensive applications in optical performance monitoring, signal processing, and sensing.

Using this type of device, the system measurement has been performed in [146]. Channel demultiplexing is demonstrated on a WDM system which consists of three 2.5-Gbit/s NRZ data. The channel spacing is 7.5-GHz. Error-free data transmission for the middle channel has been achieved. Channel banding is also demonstrated where the tunable bandwidth is used to either demultiplex a single channel or a group of channels. Because of the high-index contrast of the silicon/oxide and silicon/air, the microdisk resonator size can be further decreased with negligible increase of the optical loss [61]. And a large number of microresonators can be integrated on a chip. The FSR can be greatly increased using the vernier architecture [28] to cover the entire C-band.

6.3 Dynamic Add-drop Multiplexers

According to the time-domain coupling theory [5], the optical transmission is determined by the relationship between the resonator intrinsic loss and the power coupling ratios of the input and output waveguides. For resonators with high quality factor Q, the loss is small and the filter bandwidth is dominated by coupling. By controlling the coupling ratios, we can achieve the dynamic add-drop function and vary the bandwidth of the dropped signal.

Without voltage biases, the input power is transmitted to the through port with negligible coupling to the drop port. When the electrostatic actuators are biased, the optical powers at resonant wavelengths decrease at the through port as they are transferred to the drop port. Figure 6.5 shows the spectral response of the through and the drop ports at biases of 32.8V. The measured FSR is 5.15 nm.

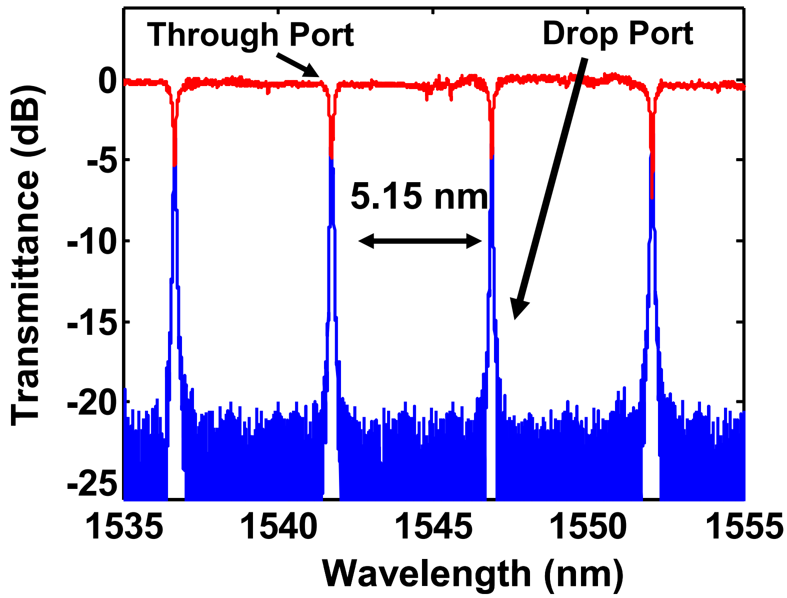
Through Port
Drop Port
5.15 nm
Transmittance (dB)
0
-5
-10
-15
-20
-25
1535
1540
1545
1550
1555
Wavelength (nm)

(a)

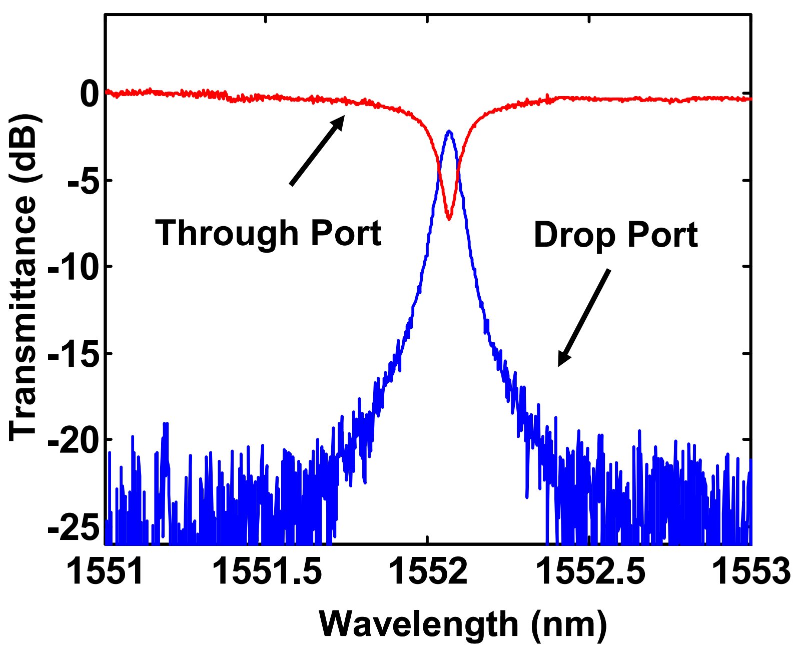
Through Port
Drop Port
Transmittance (dB)
0
-5
-10
-15
-20
-25
1551
1551.5
1552
1552.5
1553
Wavelength (nm)

(b)

Figure 6.5 (a) Measured spectral response of the through port and the drop port at actuation voltages of 32.8V. (b) Detailed measured spectral response of the through port and the drop port around the resonance of 1552.1 nm

Figure 6.6 shows the transmittance versus the applied voltages for both the through port and the drop port at a resonant wavelength of 1552.1 nm. A 21.8 dB extinction ratio is measured when the voltages are changed from 0 V (decoupled) to 58.1 V (over-coupled) for both waveguides. This kind of devices can be used as a dynamic add-drop filter.

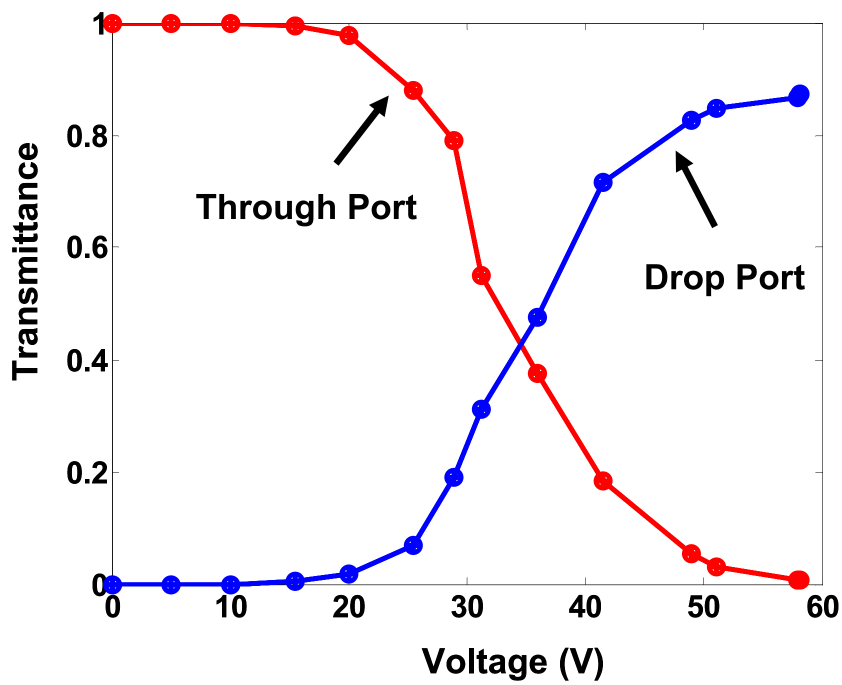

Figure 6.6 Measured transmittance versus actuation voltages at the resonant wavelength of 1552.1 nm.

6.4 Tunable Bandwidth

To demonstrate bandwidth tunability, we control the bias of each waveguide separately and measured the FWHM bandwidth of the drop port. Figure 6.7 shows the transmission spectra of the drop port for various power coupling ratios at a resonant wavelength of 1552.1 nm. When the bias voltages of input and drop waveguides are 32.7V and 35.9V, respectively, the FWHM bandwidth is 2.8 GHz, as shown by curve (a) in Figure 6.7. As the actuation voltages increase, the power coupling ratios also increase, which leads to larger bandwidth, as shown by curves (b) through (g). The detailed bias voltage pairs are shown in Table 6.2. With 48.6V (input port) and 58.1V (drop port), the bandwidth increases to 78.4 GHz, as shown by curve (g). To our knowledge, this is the largest bandwidth tuning range in microresonator-based filters reported up to date.

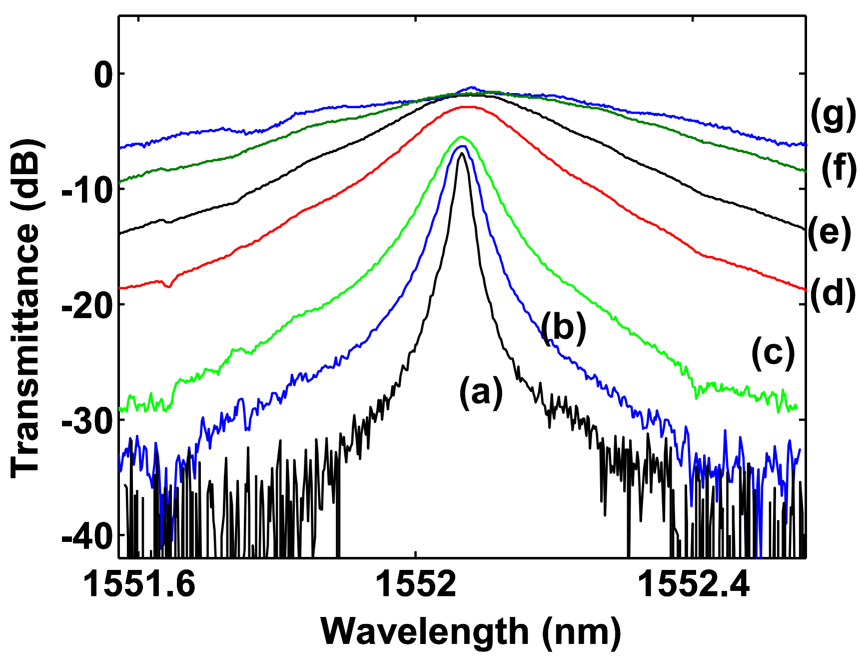

Figure 6.7 The measured spectra response at the drop port with various actuation biases. The bias conditions are shown in Table 6.2.

Spectrum Curve	Through Port Voltage (v)	Drop Port Voltage (v)
(a)	32.7	35.9
(b)	32.8	36.1
(c)	39.9	38.9
(d)	42.5	49
(e)	43.5	51.1
(f)	45.9	57.9
(g)	48.6	58.1

Table 6.2 Actuation bias conditions for the measured bandwidth tunable spectra in Figure 6.7.

As we have analyzed in Chapter 2, the optical transmission can be expressed as a function of resonant frequency (ω_0), power coupling ratio of the input and output waveguides (κ_1 and κ_2, respectively), round-trip propagation time (T), and round-trip resonator loss (γ). We list here again for further derivation convenience as

$$T_{through}(\omega) = \frac{j(\omega-\omega_0)+(\gamma+\kappa_2-\kappa_1)/2T}{j(\omega-\omega_0)+(\gamma+\kappa_2+\kappa_1)/2T} \tag{6.1}$$

and

$$T_{drop}(\omega) = \frac{\sqrt{\kappa_1\kappa_2}/T}{j(\omega-\omega_0)+(\gamma+\kappa_2+\kappa_1)/2T} \tag{6.2}$$

Here $T_{through}(\omega)$ and $T_{drop}(\omega)$ represent the amplitude transfer functions at the through and the drop ports, respectively. And $\gamma = 4\pi^2 R\cdot n_g / Q_0\lambda_0$, where n_g is the effective group index of the mode, R is the radius of the microresonator, Q_0 is the unloaded quality factor, and λ_0 is the resonant wavelength.

Equations (6.1) and (6.2) indicate that the transmission spectra depend on the intrinsic Q of the microresonator and the power coupling ratio. The mathematical expressions can be intuitively understood via the following definition of Q introduced in Chapter 2:

$$\Delta\omega = \omega_0 \cdot \frac{1}{Q_L} = \omega_0 \cdot \left(\frac{1}{Q_0} + \frac{1}{Q_\kappa}\right) \tag{6.3}$$

where Q_L is the loaded quality factor, Q_0 is the intrinsic quality factor, and Q_κ is the quality factor effectively induced by the power coupling ratio κ. Changing the power coupling ratio is equivalent to changing Q_κ, thus the transmission bandwidth is altered.

Using this model, the unloaded quality factors, Q_0, and the power coupling ratio, κ_1 and κ_2, are extracted from the measured optical spectra by least-mean-square-error fitting to the model. Figure 6.8 shows the measured and the fitted spectra around the resonance peak at 1552.1 nm when the filter bandwidth is tuned to those corresponding to curve (a) through (g) in Figure 6.7. The experimental spectra matched very well with the theoretical model. From the fitted spectral response, the unloaded quality factor, Q_0, of the microtoroidal resonator is extracted to be around 110,000. The power coupling ratio κ_1 increases from 1.6% to 67%, and κ_2 from 0.2% to 19%, when the FWHM bandwidth is tuned from 2.8 GHz to 78.4 GHz, as shown in Figure 6.9.

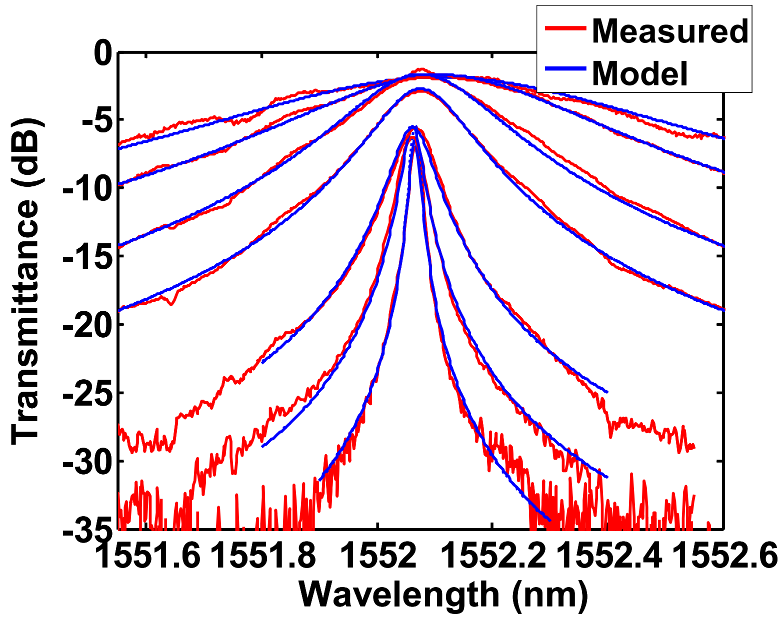

Figure 6.8 Measured and modeled spectra at the drop port with different actuation biases at the resonance of 1552.1 nm. The bias conditions are the same as in Figure 6.7, and are listed in Table 6.2.

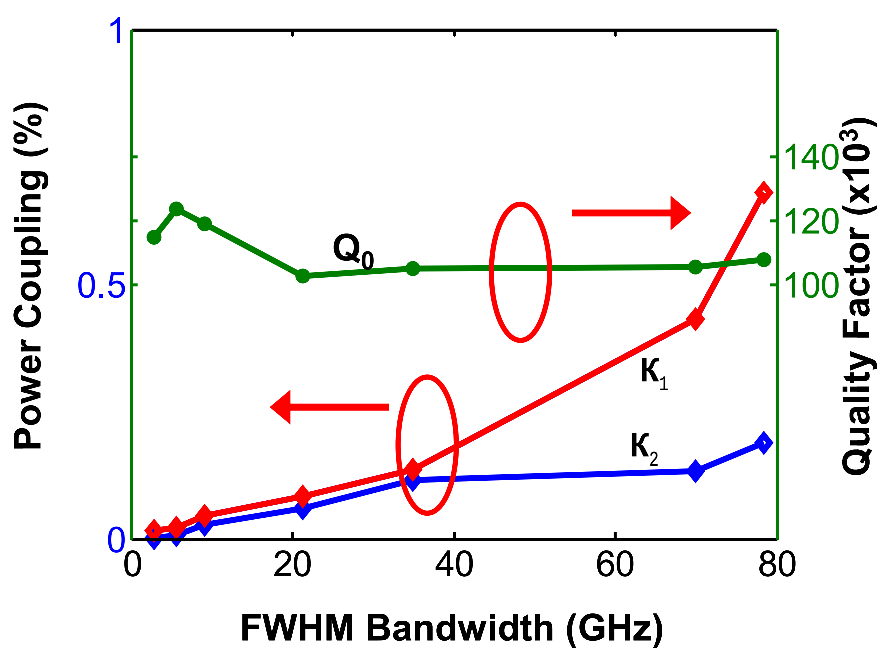

Figure 6.9 Calculated unloaded Q and the power coupling ratios versus the FWHM bandwidth of the spectra. The parameters are extracted from the experimental data by fitting to the theoretical model curves.

When κ_1 and κ_2 are much larger than γ (κ_1, $\kappa_2 >> \gamma$), critical coupling condition becomes $\gamma + \kappa_2 = \kappa_1$, so $\kappa_2 \approx \kappa_1$. At the drop port, the insertion loss at the resonant wavelength is very small, as Equation (6.2) will be derived as

$$T_{drop}(\omega_0) = \frac{\sqrt{\kappa_1 \kappa_2} / T}{(\gamma + \kappa_2 + \kappa_1)/2T} \approx \frac{\sqrt{\kappa_1 \kappa_2}}{\kappa_2 + \kappa_1)/2} \approx 1 \tag{6.4}$$

This permits the bandwidth tuning while maintaining a low insertion loss. When κ_1 and κ_2 are controlled to approach γ, the insertion loss at the resonant wavelength starts to increase. As shown in Figure 6.8, the lowest insertion loss demonstrated is -1.5 dB when κ_1 and κ_2 are 67% and 19%, respectively, while the intrinsic loss γ is 0.017.

Since γ is inversely proportional to Q_0, high-Q microresonator is desired to achieve low loss and large tuning range.

6.5 Summary and Future Directions

In this chapter, we describe a monolithically integrated dynamic add-drop filter with tunable bandwidth using the MEMS-actuated single-crystalline silicon microtoroidal resonator. The FWHM bandwidth has been demonstrated to continuously tunable from 2.8 GHz to 78.4 GHz. To the author's knowledge, this is the largest bandwidth tuning range in microresonator-based filters reported up to date. Using the time domain coupling theory, a theoretical model is established. The experimental and the theoretical results have agreed very well. From the fitted spectral response, the unloaded quality factor of the microtoroidal resonator is extracted to be 110,000. The power coupling ratio κ_1

increases from 1.6% to 67%, and κ_2 from 0.2% to 19%. As a dynamic add-drop filter, wavelength switching with a 21.8 dB extinction ratio is attained. This tunable filters has applications in dynamic bandwidth allocation, optical performance monitoring, signal processing, and sensing.

In the aforementioned chapters, we have investigated the vertically-coupled silicon microresonator, including design, fabrication and its applications. In this dissertation, we have demonstrated the feasibility of this device for a variety of applications. For practical deployment, additional research and development in the following areas are needed:

To reduce optical insertion loss, we need to further increase the quality factor of the microresonators. Currently our microresonators are fabricated by dry etching. Using hydrogen annealing process, we have been able to smooth the surface roughness and to attain a Q of 110,000. To achieve higher quality factor in this kind of compact silicon structure, the surface state absorption needs to be taken into consideration [61]. The etching conditions can be further optimized to diminish the initial roughness. Thermal oxidation to smooth out the surface (such as in [109]) or surface chemical treatment to passivate the surface (such as in [101]) are possible ways to further increase the quality factor.

The fabrication process can be investigated to decrease the complexity and increase yield. The wafer bonding process used in current design is a critical step to achieve the success of the device integration and functioning. To further increase the yield and simplify the fabrication process, other structures such as laterally-coupled microresonator systems and other tuning mechanisms need to be explored.

Lastly, proper packaging of the device is necessary for practical applications. Hermetic sealing can significantly increase the lifetime of the device. The interface between the integrated device and the peripheral structure is important to gain a satisfactory system-level performance and to provide as an on-wafer testing approach. Tapers and spot-size mode converters can be integrated with the waveguides [147-149].

Chapter 7 Conclusion

Optical microresonators are key building blocks for many photonic integrated circuits (PICs) areas. Their applications include optical filters, modulators, optical delay lines, laser sources, nonlinear optical devices, and optical sensors. In many applications, it is desirable to control the optical functions dynamically. Tunable microresonators can enable such functions. Most of the tunable microresonators reported to date used electro-optic, thermo-optic, or free-carrier plasma effects to control the resonant frequency, and gain-trimming or electro-absorption to control resonator Q. However, the coupling between the resonator and its input/output is generally fixed by the fabrication process. The ability to vary the optical coupling enable us to either achieve better optical performance or implement dynamic functions in the emerging adaptive photonic circuits. Ultra-compact tunable, switchable, and reconfigurable components can be realized.

In the study of this dissertation, a tunable microresonator with MEMS actuation is realized on silicon platform. Compared with III-V or II-VI semiconductor compounds, silicon has the advantages of low cost, mature fabrication technology, and potential monolithic integration with CMOS devices. Previously high performance microdisk resonators with tunable coupling have been demonstrated. By physically changing the gap spacing between the waveguide and the resonator, the power coupling ratio can be varied over a wide range from 0 to 34% and a high Q (quality factor) of 100,000 have been achieved simultaneously. Tunable dispersion compensators (185 ps/nm to 1200 ps/nm) have also been demonstrated. One drawback of the microdisk devices is the lack of radial mode control, which could produce additional resonances due to high-order modes. In this research, a novel tunable single-crystalline silicon microtoroidal resonator is proposed and demonstrated for the first time. Microtoroidal resonators offer tighter confinement of the optical mode and eliminate multiple radial modes observed in microdisks. By combining the hydrogen annealing and the wafer bonding processes, very compact and high Q resonators can be monolithically integrated with optical waveguides. The resonator-waveguide spacing is precisely controlled from 0 to 1 μm range. Use hydrogen-assisted, surface-tension-induced annealing, smooth surface is created and high optical performance is attained.

We have achieved an unloaded Q of 110,000 for a 39.5-μm-diameter resonator with a toroidal radius of 200 nm. The device is able to operate in all three coupling regimes: under-, critical, and over-coupling. We have developed a detailed model using the time-domain coupling theory. The experimental and the theoretical results agree very well. The loaded Q is continuously tunable from 110,000 to 5,400. Using this type of microtoroidal resonators we have successful demonstrated applications as bandwidth-tunable filters and dynamic add-drop multiplexers. A 21.8 dB extinction ratio is attained for a dynamic add-drop multiplexer. The bandwidth of the drop port is tuned from 2.8 to

78.4 GHz by voltage control, the highest bandwidth tunability in this type of filter reported up to date.

The resonators can also be decoupled from the waveguide, enabling them to be cascaded and integrated along the waveguide for optical signal processing. This type of devices can be used as a building block of reconfigurable photonic integrated circuits. Their applications include optical matched filtering, dynamic bandwidth allocation, optical performance monitoring, optical signal processing, reconfigurable add-drop multiplexers, wavelength-selective switches and crossconnects, and optical sensing.

Appendix 1 Recipe of Silicon Microtoroid Formation Using Hydrogen Annealing Technology

PRE-CLEAN	
1Organics	4:1 H2SO4:H2O2 @90C for 10 minutes
2 Rinse	Dump Rinse (std 6 cycles) OR overflow rinse for 5 minutes
3 Metal trace	5:1:1 H2O:H2O2:HCl @70C for 10 minutes
4 Rinse	Dump Rinse (std 6 cycles) OR overflow rinse for 5 minutes
5 Oxide	50:1 HF dip for 15 - 30 seconds
6 Rinse	Dump Rinse (std 6 cycles) OR overflow rinse for 5 minutes
7 Spin Dry	Spin Dry (280 seconds rinse; 120 seconds spin dry; >16 ohm-cm on DI H2O)

	STANDARD					
STEP	1	2	3	4	5	6
STEP NAME	START	PURGE	HOMESUS	TEMP CK	LOAD	ROTATE
DURATION	0.1 SEC	20 SEC	15 SEC	0.1 SEC	0.1 SEC	20 SEC
TOKEN (Macro of operations)					LOAD	
CENTER (°C)	800	910	910	910S	850*	950

DEPOSITION/ VENT	VENT	VENT	VENT	VENT	VENT	VENT
N2H2 ((Liter/min)	20H	80H	40HR*	20H	10H	20HR
ROTATION	0	10RD	0	0	0	35R
HClHI	0V	0V	0V	0V	0V	0V
HCl	0V	0V	0V	0V	0V	0V
V_Pressure (Torr)	ATM	ATM	ATM	ATM	ATM	30
Vent Match	0	0	0	0	0	1
Temp. Variation Allowance offset						
Front	DEFAULT	-100	-100	DEFAULT	DEFAULT	DEFAULT
Side	DEFAULT	-100	-100	DEFAULT	DEFAULT	DEFAULT
Rear	DEFAULT	-100	-100	DEFAULT	DEFAULT	DEFAULT

Ramp UP		**USER**		
STEP	7	8	9	10
STEP NAME	PUMP	PUMP	BAKE	BAKE
DURATION	30 SEC	20 SEC	5 MIN	45 SEC
TOKEN (Macro of operations)				
CENTER (Celsius)	1000	1000	1000	900R
DEPOSITION/VENT	VENT	VENT	VENT	VENT
N2H2 ((Liter/min)	20H	20H	20H	20H
ROTATION	*SAME	*SAME	*SAME	*SAME
HClHI	0V	0V	0V	0V
HCl	0V	0V	0V	0V
V_Pressure (Torr)	10	10	10	10
Vent Match	1	1	1	1
Temp. Variation Allowance offset				
Front	DEFAULT	DEFAULT	DEFAULT	DEFAULT
Side	DEFAULT	DEFAULT	DEFAULT	DEFAULT
Rear	DEFAULT	DEFAULT	DEFAULT	DEFAULT

	STANDARD			
STEP	11	12	13	14
STEP NAME	RMP DOWN	HOMESUS	UNLOAD	END
DURATION	60 SEC	15 SEC	0.1 SEC	1 SEC
TOKEN (Macro of operations)			UNLOAD	END
CENTER (Celsius)	800	850	800	800
DEPOSITION/VENT	VENT	VENT	VENT	VENT
N2H2 ((Liter/min)	20H	10HR	10H	20H

ROTATION	10R	0	0	0
HClHI	0V	0V	0V	0V
HCl	0V	0V	0V	0V
V_Pressure (Torr)	ATM	ATM	ATM	ATM
Vent Match	0	0	0	0
Temp. Variation Allowance offset				
Front	DEFAULT	DEFAULT	DEFAULT	DEFAULT
Side	DEFAULT	DEFAULT	DEFAULT	DEFAULT
Rear	DEFAULT	DEFAULT	DEFAULT	DEFAULT

Appendix 2 Time Domain Coupling Theory Fitting Model Programs

A2.1 Resonator Parameter Fitting with FP: ResonanceFitMain.m

```
% This program fits the resonance dips in the transmission port of
% waveguide-coupled microdisk.
% It is based on the paper B.E. Little et al., "Microring Resonator
% Channel Dropping Filters, JLT, 15, pp. 998, (1997).
% Adapted to include also the facet reflection Fabry Perot
% effects.

% Initialized by David Leuenberger
% Revised by Jin Yao
% Adding calling functions to fit all coupling regimes:
% ResonanceFitMainFix more suitable for under-coupling and over
coupling regimes
% ResonanceFitMain more suitable for around critical-coupling

% It is asumed that the power spectrum is saved in a two-column array
called
% "data".
% First launch "plotInitialGuess.m" to load a data file and set the
initial
% guess

% Optimization parameters:
options = optimset('MaxIter',6000,'MaxFunEvals',6000);
```

```
% coefficient vector for initial guess:
x0(1) = wl0_init;  %1547.621e-9;
x0(2) = Q0_init;
x0(3) = Qe_init;
x0(4) = r_init;
x0(5) = Leff_init;
x0(6) = P0dBm_init;
x0(7) = D_init;
x0(8) = gamma_init;

% Calculate the new coefficients using FMINSEARCH
[x,fval,exitflag,output] =
fminsearch(@fitFunc,x0,options,WLdata,Pdata);

% Special connstraints:
% The waveguide loss gamma has to be smaller than 1, if not there would
be
% gain!

% if x(1)>1554.75e-9 %1558.333e-9  %1544.465e-9 for 46V
%     x(1)=1554.75e-9;
% end
%
% if x(1)<1554.7365e-9
%     x(1)=1554.7365e-9;
% end

if x(8)>1
    x(8)=1;
end

if x(7)>-0.01
    x(7)=-0.01;
end

wl0_init = x(1)
Q0 = x(2)
Qe = x(3)
r = x(4)
Leff = x(5)
P0dBm = x(6);
D = x(7)
gamma = x(8)

switch exitflag
    case 1
        disp('FMINSEARCH converged to a solution X.');
    case 0
        disp('Maximum number of function evaluations or iterations
reached.');
    case -1
        disp('Algorithm terminated by the output function.');
end

disp(['Number of function evaluations: ' num2str(output.funcCount)]);
```

```
disp(['Number of function iterations: ' num2str(output.iterations)]);

% Plot fit:
tTot = transmissionFunc(x,WLdata);
Tlin = tTot.*conj(tTot);
TdB = 10*log10(Tlin);
PdBfit = P0dBm + TdB;

figure(4);clf;
plot(1e9*WLdata,Pdata-1.3,'-b',1e9*WLdata,PdBfit-1.3,'-.r');
%xlabel('wavelength (nm)');ylabel('Output Power (dBm)');
legend('Measured','Model');
%title(['Q0=' num2str(round(Q0)) ',Qe=' num2str(round(Qe))]);
Q_tot=1/(1/Q0+1/Qe)

% Initial estimation of parameter values
% Read data file:
[FileName,PathName] = uigetfile; eval(['data = dlmread(''' PathName
FileName ''')']);

% Parameters:
%%%%%%%%%%%%%%%%%%%%%%%%%%%%%%%%%%%%%%%%
pixel_start=300
pixel_stop=800%length(data);
npoints = 500;


% Set nitial guess for fit parameters:
wl0_init = 1548.176e-9; % resonance wavelength [m]
Q0_init = 111489; % intrinsic quality factor
Qe_init = 80000000; % external quality factor
r_init = 0.49865;%0.47465; % facet reflectivity
Leff_init = %0.0072396; % Effective FP cavity length
P0dBm_init = -36.7%-37.5; % power level normalization [dBm]
D_init = -0.101; % Waveguide dispersion [dn/(d_lambda*neff)]
gamma_init = 0.991; % Single trip waveguide loss exp(-alpha*L) L=2mm;
alp=1.5 cm-1
%%%%%%%%%%%%%%%%%%%%%%%%%%%%%%%%%%%%%%%%%%%%%%%%%%%%%%%%%%%%%%%%%%%%%%%%
%%%%
WLdata=1e-9*data(pixel_start:pixel_stop,1); % wavelength vector
Pdata=data(pixel_start:pixel_stop,2); % Transmission vector [dB]
figure(1);clf;
plot(1e9*WLdata,Pdata);
xlabel('Wavelength [nm]');ylabel('P [dBm]');title('Raw data');
%%%%%%%%%%%%%%%%%%%%%%%%%%%%%%%%%%%%%%%%%%%%%%%%%%%%%%%%%%%%%%%%%%%%%%%%
%%%%
wlVec=WLdata;
x0(1) = wl0_init;
x0(2) = Q0_init;
x0(3) = Qe_init;
x0(4) = r_init;
x0(5) = Leff_init;
x0(6) = P0dBm_init;
x0(7) = D_init;
x0(8) = gamma_init;
```

```
tTot = transmissionFunc(x0,wlVec);
Tlin = tTot.*conj(tTot);
TdB = 10*log10(Tlin);
PdB = P0dBm_init + TdB;

thickLines(4);
figure(2);clf;
plot(1e9*wlVec,Tlin);xlabel('WL [nm]');ylabel('Ttot');title('Calculated
Curve');

figure(3);clf;
plot(1e9*WLdata,Pdata,'-b',1e9*WLdata,PdB,'r-.');
xlabel('WL [nm]');ylabel('P_[150] [dBm]');
legend('raw data','calculation');


%%%%%%%%%%%%%%%%%%%%%%%%%%%%%%%%%%%%%%%%%
function tTot=resonanceFitFunc(x,wlVec)

wl0 =x(1); % 1547.621e-9;
Q0 = x(2);
Qe = x(3);
r = x(4);
Leff = x(5);
P0dBm = x(6);
D = x(7);
gamma = x(8);

n=length(wlVec);

% Comment: For the moment we neglect the waveguide absorption

% Description of input parameters:

% wlVec: vector containing the wavelenghts [nm]
% tTot: total amplitude transmission including microdisk resonance and
%       facet reflectivity

% Fitting parameters:
% wl_0: resonance wavelength
% Q0: intrinsic quality factor of microdisk
% Qe: external quality factor of microdisk
% r:facet (amplitude) reflectivity
% Leff: effective waveguide length (= L*neff)
% P0dBm % power level normalization [dBm] (not explicitly used in this
% function)
% D: Waveguide dispersion [dn/(d_lambda*neff)]
% gamma: Single trip waveguide loss exp(-alpha*L)

% As in usual derivation the Fabry Perot transmissiont can be written
% as an infinite sum: theTot = a0*(1+q+q^2+q^3+...) = a0/(1-q)

kVec = 2*pi./wlVec;
```

```
%tDisk=(j*2*(wlVec-wl0)./wlVec+ones(n,1)/Q0-ones(n,1)/Qe)./(j*2*(wlVec-
wl0)./wlVec+ones(n,1)/Q0+ones(n,1)/Qe);
tDisk=(j*2*(-wlVec+wl0)./wlVec+ones(n,1)/Q0-ones(n,1)/Qe)./(j*2*(-
wlVec+wl0)./wlVec+ones(n,1)/Q0+ones(n,1)/Qe);


a0 = (1-r)^2*gamma*exp(j*kVec.*(Leff*(1+D*(wlVec-wl0)))).*tDisk;
q = r^2*gamma^2*exp(j*2*kVec.*(Leff*(1+D*(wlVec-wl0)))).*(tDisk.^2);

tTot = a0./(1-q);



%%%%%%%%%%%%%%%%%%%%%%%%%%%%%%%%%%%%%%%
function error = fitFunc(x,wlVec,Pdata)
% This function is called by fminsearch.
% x is a vector which contains the coefficients of the
% equation. WLdata and Pdata are the original data sets that are
% passed to fminsearch.

% constraints:
% The waveguide loss gamma has to be smaller than 1, if not there would
be
% gain!
if x(8)>1
    x(8)=1;
end

if x(7)>-0.01
    x(7)=-0.01;
end

if x(1)>1554.252e-9  %Given a certain range due to ripples
    x(1)=1554.252e-9;
end

if x(1)<1544.1e-9
    x(1)=1544.1e-9;
end
P0dBm = x(6);

n=length(wlVec);

tTot = transmissionFunc(x,wlVec);
Tlin = tTot.*conj(tTot);
TdB = 10*log10(Tlin);
PdB = P0dBm + TdB;
%diff = Pdata  - PdB;

error = sum(abs(Pdata  - PdB).^2);


end
```

A2.2 Filter Through and Drop port fitting for Bandwidth Tuning: filterfitting.m

```
%%%%%%%%%%%%%%%%%%%%%%%
% Fitting through port and drop port spectra
% Based on Time Domain Coupling Theory
% Last revised 4/25/2007 Jin Yao

function thruput()

global Q T r lmd01

% total number of data points
Num=5001;

% multiply column txt file
P30V=textread('\your directory\yourfile');

%receiving drop port baseline reference dBm
ref=Reference_dBm;

wl=P30V(:,1);
R=P30V(:,2);

for i=1:Num
    ip(i) =Reference_dBm;  % receiving reference level
end
Input=(ip)';

plot(wl, R-ref,'r-');
hold on

ibegin=1
for i=1:Num
    if P30V(i,1)== 1551.8; %Fitting range lower
    ibegin=i;
    end

        if P30V(i,1)== 1552.4; %Fitting range upper
    iEnd =i;
        end

end

i=1;  %%DO not use j as counter
for ij=ibegin:1:iEnd
   WL(i)=P30V(ij,1); %to find the WL of best fit
   Spec(i)=R(ij)-Input(ij);  %% normalized spectrum

    i=i+1;
end
```

```
lmd01=1552.062e-9;   %Central wavelength
c=3e8;
w=2*pi*c./(WL*1e-9);
w01=2*pi*c/lmd01
R=20e-6;
ng=1550^2/(2*pi*20e3*5.16);  %TE FSR = 5.16
vg=c/ng;
T=2*pi*R/vg

% Refined start guess after initial large range guess
alp=1.4*1e2;   % cm-1
r=2*pi*R*alp   %0.01257
Q_alp=4*pi^2*R*ng/(lmd01*r)


% Refine your searching range
k0=[0.0211    0.0060    0.0153]; % K(3) is  Gama

lb=[0.012,0.002,0.014];  % lower boundary and higher boundary
hb=[1,1,0.8];

[k, resnorm]=lsqcurvefit(@dropfit,k0,w,Spec,lb,hb); % Call the function
to fit

% k
% resnorm
%%DO not use j as counter

myfit=10*log10((abs(2*sqrt(k(1)*k(2))./(j*2*T*(w-
w01)+k(3)+k(1)+k(2)))).^2));
plot(WL,myfit, 'b-');  hold on% auto


myfit=10*log10((abs(2*sqrt(k0(1)*k0(2))./(j*2*T*(w-
w01)+k0(1)+k0(2)+k0(3)))).^2));

Q_fit=4*pi^2*R*ng/(lmd01*k(3))
Q_k0=4*pi^2*R*ng/(lmd01*k0(3))
end


%%%%%%%%%%%%%%%%%%%%%%
%Call function

function F = dropfit(k,w)
global Q T r lmd01


% Metric resonant WL

w0=2*pi*3*1e8/lmd01;
```

```
F=10*log10((abs(2*sqrt(k(1)*k(2))./(j*2*T*(w-w0)+k(3)+k(1)+k(2))).^2));

End
```

BIBLIOGRAPHY

[1] K. Oda, N. Takato, and H. Toba, "A wide-FSR waveguide double-ring resonator for optical FDM transmission systems," *Journal of Lightwave Technology*, vol. 9, pp. 728-36, 1991.

[2] C. K. Madsen, A. J. Bruce, M. A. Cappuzzo, and R. E. Scotti, "Bandpass filter demonstration using all-pass filter decomposition and ring resonators," presented at Conference Proceedings. LEOS'98. 11th Annual Meeting. IEEE Lasers and Electro-Optics Society 1998 Annual Meeting (Cat. No.98CH36243). IEEE. Part vol.1, 1998, pp. 330-1. Piscataway, NJ, USA.

[3] B. E. Little, S. T. Chu, W. Pan, and Y. Kokubun, "Microring resonator arrays for VLSI photonics," *IEEE Photonics Technology Letters*, vol. 12, pp. 323-5, 2000.

[4] B. E. Little, S. T. Chu, P. P. Absil, J. V. Hryniewicz, F. G. Johnson, F. Seiferth, D. Gill, V. Van, O. King, and M. Trakalo, "Very high-order microring resonator filters for WDM applications," *IEEE Photonics Technology Letters*, vol. 16, pp. 2263-5, 2004.

[5] B. E. Little, S. T. Chu, H. A. Haus, J. Foresi, and J. P. Laine, "Microring resonator channel dropping filters," *Journal of Lightwave Technology*, vol. 15, pp. 998-1005, 1997.

[6] T. Sadagopan, S. J. Choi, C. Sang Jun, K. Djordjev, and P. D. Dapkus, "Carrier-induced refractive index changes in InP-based circular microresonators for low-voltage high-speed modulation," *IEEE Photonics Technology Letters*, vol. 17, pp. 414-16, 2005.

[7] Q. Xu, B. Schmidt, S. Pradhan, and M. Lipson, "Micrometre-scale silicon electro-optic modulator," *Nature*, vol. 435, pp. 325-7, 2005.

[8] P. Rabiei, W. H. Steier, Z. Cheng, W. Chuan-guang, and H. J. Lee, "Polymer micro-ring modulator with 1 THz FSR," presented at Postdeadline Papers. Summaries of papers presented at the Conference on Lasers and Electro-Optics. Conference Edition (IEEE Cat. No.02CH37337). Opt. Soc. America. Part vol.2, 2002, pp. CPDB8-1-CPDC2-3. Washington, DC, USA.

[9] C. A. Barrios, V. R. Almeida, R. Panepucci, and M. Lipson, "Electrooptic modulation of silicon-on-insulator submicrometer-size waveguide devices," *Journal of Lightwave Technology*, vol. 21, pp. 2332-9, 2003.

[10] G. Lenz, B. J. Eggleton, C. K. Madsen, C. R. Giles, and G. Nykolak, "Optimal dispersion of optical filters for WDM systems," *IEEE Photonics Technology Letters*, vol. 10, pp. 567-9, 1998.

[11] C. K. Madsen, G. Lenz, A. J. Bruce, M. A. Cappuzzo, L. T. Gomez, T. N. Nielsen, L. E. Adams, and I. Brenner, "An all-pass filter dispersion compensator using planar waveguide ring resonators," presented at OFC/IOOC'99. Optical Fiber Communication Conference and the International Conference on Integrated Optics and Optical Fiber Communications (Cat. No.99CH36322). IEEE. Part vol.4, 1999, pp. 99-101. Piscataway, NJ, USA.

[12] C. K. Madsen, J. A. Walker, J. E. Ford, K. W. Goossen, T. N. Nielsen, and G. Lenz, "A tunable dispersion compensating MEMS all-pass filter," *IEEE Photonics Technology Letters*, vol. 12, pp. 651-3, 2000.

[13] G. Lenz, B. J. Eggleton, C. K. Madsen, and R. E. Slusher, "Optical delay lines based on optical filters," *IEEE Journal of Quantum Electronics*, vol. 37, pp. 525-32, 2001.

[14] G. Lenz, B. J. Eggleton, and C. K. Madsen, "Optical filter dispersion in WDM systems: a review," *OSA trends in optics and photonics. WDM components. Vol.29. Opt. Soc. America. 1999*, pp. 246-53.

[15] T. J. Kippenberg, S. M. Spillane, D. K. Armani, and K. J. Vahala, "Ultralow-threshold microcavity Raman laser on a microelectronic chip," *Optics Letters*, vol. 29, pp. 1224-6, 2004.

[16] W. von Klitzing, R. Long, V. S. Ilchenko, J. Hare, and V. Lefevre-Seguin, "Tunable whispering gallery modes for spectroscopy and CQED experiments," *New Journal of Physics, vol.3, 2001*.

[17] W. von Klitzing, R. Long, V. S. Illcenko, J. Hare, and V. Lefevre-Seguin, "Frequency tuning of the whispering-gallery modes of silica microspheres for cavity quantum electrodynamics and spectroscopy," *Optics Letters*, vol. 26, pp. 166-8, 2001.

[18] F. Vollmer, S. Arnold, D. Braun, I. Teraoka, and A. Libchaber, "Multiplexed DNA quantification by spectroscopic shift of two microsphere cavities," *Biophysical Journal*, vol. 85, pp. 1974-9, 2003.

[19] A. M. Armani and K. J. Vahala, "Heavy water detection using ultra-high-Q microcavities," *Optics Letters*, vol. 31, pp. 1896-8, 2006.

[20] S. J. Choi, Z. Peng, Q. Yang, S. J. Choi, and P. D. Dapkus, "Eight-channel microdisk CW laser arrays vertically coupled to common output bus waveguides," *IEEE Photonics Technology Letters*, vol. 16, pp. 356-8, 2004.

[21] X. Liu, W. Fang, Y. Huang, X. H. Wu, S. T. Ho, H. Cao, and R. P. H. Chang, "Optically pumped ultraviolet microdisk laser on a silicon substrate," *Applied Physics Letters*, vol. 84, pp. 2488-90, 2004.

[22] S. J. Choi, K. Djordjev, S. J. Choi, and P. D. Dapkus, "Microdisk lasers vertically coupled to output waveguides," *IEEE Photonics Technology Letters*, vol. 15, pp. 1330-2, 2003.

[23] K. Sasaki, F. Ohno, A. Motegi, and T. Baba, "Arrayed waveguide grating of 70 x 60 um2 size based on Si photonic wire waveguides," *Electronics Letters*, vol. 41, pp. 801-2, 2005.

[24] D. Dai, L. Liu, L. Wosinski, and S. He, "Design and fabrication of ultra-small overlapped AWG demultiplexer based on a-Si nanowire waveguides," *Electronics Letters*, vol. 42, pp. 400-2, 2006.

[25] K. Okamoto, *Fundamentals of Optical Waveguides*. San Diego: Academic Press, 2000.

[26] B. Little, "A VLSI photonics platform," presented at Optical Fiber Communications Conference (OFC). (Trends in Optics and Photonics Series Vol.86) Technical Digest (IEEE Cat. No.03CH37403). Opt. Soc. America. Part vol.2, 2003, pp. 444-5. Washington, DC, USA.

[27] P. Rabiei, W. H. Steier, Z. Cheng, C.-g. Wang, and H. J. Lee, "Polymer micro-ring modulator with 1 THz FSR," presented at Postdeadline Papers. Summaries of papers presented at the Conference on Lasers and Electro-Optics. Conference Edition (IEEE Cat. No.02CH37337). Opt. Soc. America. Part vol.2, 2002, pp. CPDB8-1-CPDC2-3. Washington, DC, USA.

[28] S. T. Chu, B. E. Little, V. Van, J. V. Hryniewicz, P. P. Absil, F. G. Johnson, D. Gill, O. King, F. Seiferth, M. Trakalo, and J. Shanton, "Compact full C-band tunable filters for 50 GHz channel spacing based on high order micro-ring resonators," presented at Optical Fiber Communication Conference (OFC) (IEEE Cat. No.04CH37532). Opt. Soc. America. Part vol.2, 2004, pp. 3. Washington, DC, USA.

[29] H. C. Tapalian, J. P. Laine, and P. A. Lane, "Thermooptical switches using coated microsphere resonators," *IEEE Photonics Technology Letters*, vol. 14, pp. 1118-20, 2002.

[30] P. Kopperschmidt, "Tunable band gaps in electro-optical photonic bi-oriented crystals," *Applied Physics B (Lasers and Optics)*, vol. B73, pp. 717-20, 2001.

[31] K. Djordjev, S.-J. Choi, S.-J. Choi, and P. D. Dapkus, "Active semiconductor microdisk devices," *Journal of Lightwave Technology*, vol. 20, pp. 105-13, 2002.

[32] K. Djordjev, S.-J. Choi, S.-J. Choi, and R. D. Dapkus, "Microdisk tunable resonant filters and switches," *IEEE Photonics Technology Letters*, vol. 14, pp. 828-30, 2002.

[33] A. L. Huston and J. D. Eversole, "Strain-sensitive elastic scattering from cylinders," *Optics Letters*, vol. 18, pp. 1104-6, 1993.

[34] V. S. Ilchenko, P. S. Volikov, V. L. Velichansky, F. Treussart, V. Lefevre-Seguin, J. M. Raimond, and S. Haroche, "Strain-tunable high-Q optical microsphere resonator," *Optics Communications*, vol. 145, pp. 86-90, 1998.

[35] G. N. Nielson, D. Seneviratne, F. Lopez-Royo, P. T. Rakich, F. Giacometti, H. L. Tuller, and G. Barbastathis, "MEMS based wavelength selective optical switching for integrated photonic circuits," presented at Conference on Lasers and Electro-Optics (CLEO). IEEE. Part vol.1, 2004, pp. 2. Piscataway, NJ, USA.

[36] K. Djordjev, S.-J. Choi, S.-J. Choi, and P. D. Dapkus, "Vertically coupled InP microdisk switching devices with electroabsorptive active regions," *IEEE Photonics Technology Letters*, vol. 14, pp. 1115-17, 2002.

[37] K. Djordjev, S.-J. Choi, S.-J. Choi, and P. D. Dapkus, "Gain trimming of the resonant characteristics in vertically coupled InP microdisk switches," *Applied Physics Letters*, vol. 80, pp. 3467-9, 2002.

[38] K. Djordjev, S.-J. Choi, S.-J. Choi, and P. D. Dapkus, "Active semiconductor microdisk switching devices utilizing gain and electroabsorption effects," presented at Optical Fiber Communications Conference. (OFC). Postconference Technical Digest. Postdeadline Papers (IEEE Cat. No.02CH37339). Opt Soc. America. Part vol.2, 2002, pp. FA2-1-3. Washington, DC, USA.

[39] L. Martinez and M. Lipson, "High confinement suspended micro-ring resonators in silicon-on-insulator," *Optics Express, vol.14, no.13*, pp. 6259-6263, 2006.

[40] S. T. Chu, W. Pan, S. Sato, T. Kaneko, B. E. Little, and Y. Kokubun, "Wavelength trimming of a microring resonator filter by means of a UV sensitive polymer overlay," *IEEE Photonics Technology Letters*, vol. 11, pp. 688-90, 1999.

[41] D. K. Sparacin, H. Ching-yin, L. C. Kimerling, J. Michel, J. P. Lock, and K. K. Gleason, "Trimming of microring resonators by photo-oxidation of a plasma-polymerized organosilane cladding material," *Optics Letters*, vol. 30, pp. 2251-3, 2005.

[42] A. Yariv, "Critical coupling and its control in optical waveguide-ring resonator systems," *IEEE Photonics Technology Letters*, vol. 14, pp. 483-5, 2002.

[43] P. Yong-Le and R. K. Chang, "Highly efficient prism coupling to whispering gallery modes of a square mu cavity," *Applied Physics Letters*, vol. 82, pp. 487-9, 2003.

[44] S. Schiller and R. L. Byer, "High-resolution spectroscopy of whispering gallery modes in large dielectric spheres," *Optics Letters*, vol. 16, pp. 1138-40, 1991.

[45] M. L. Gorodetsky and V. S. Ilchenko, "Optical microsphere resonators: optimal coupling to high-<i>Q</i> whispering-gallery modes," *Journal of the Optical Society of America B (Optical Physics)*, vol. 16, pp. 147-54, 1999.

[46] M. L. Gorodetsky and V. S. Ilchenko, "High-Q optical whispering-gallery microresonators: precession approach for spherical mode analysis and emission patterns with prism couplers," *Optics Communications*, vol. 113, pp. 133-43, 1994.

[47] D. R. Rowland and J. D. Love, "Evanescent wave coupling of whispering gallery modes of a dielectric cylinder," *IEE Proceedings-J Optoelectronics*, vol. 140, pp. 177-188, 1993.

[48] R. Ulrich, "Theory of the prism-film coupler by plane-wave analysis," *Journal of the Optical Society of America*, vol. 60, pp. 1337-50, 1970.

[49] P. K. Tien and R. Ulrich, "Theory of prism-film coupler and thin-film light guides," *Journal of the Optical Society of America*, vol. 60, pp. 1325-37, 1970.

[50] D. Sarid, P. J. Cressman, and R. L. Holman, "High-efficiency prism coupler for optical waveguides," *Applied Physics Letters*, vol. 33, pp. 514-15, 1978.

[51] D. Sarid, "High efficiency input-output prism waveguide coupler: an analysis," *Applied Optics*, vol. 18, pp. 2921-6, 1979.

[52] V. B. Braginsky, M. L. Gorodetsky, and V. S. Ilchenko, "Quality-factor and nonlinear properties of optical whispering-gallery modes," *Physics Letters A*, vol. 137, pp. 393-7, 1989.

[53] N. Dubreuil, J. C. Knight, D. K. Leventhal, V. Sandoghdar, I. Hare, and V. Lefevre, "Eroded monomode optical fiber for whispering-gallery mode excitation in fused-silica microspheres," *Optics Letters*, vol. 20, pp. 813-15, 1995.

[54] G. Griffel, S. Arnold, D. Taskent, A. Serpenguzel, J. Connolly, and N. Morris, "Morphology-dependent resonances of a microsphere-optical fiber system," *Optics Letters*, vol. 21, pp. 695-7, 1996.

[55] A. Serpenguzel, S. Arnold, and G. Griffel, "Excitation of resonances of microspheres on an optical fiber," *Optics Letters*, vol. 20, pp. 654-6, 1995.

[56] V. S. Ilchenko, X. S. Yao, and L. Maleki, "Pigtailing the high-Q microsphere cavity: a simple fiber coupler for optical whispering-gallery modes," *Optics Letters*, vol. 24, pp. 723-5, 1999.

[57] J. C. Knight, G. Cheung, F. Jacques, and T. A. Birks, "Phase-matched excitation of whispering-gallery-mode resonances by a fiber taper," *Optics Letters*, vol. 22, pp. 1129-31, 1997.

[58] M. Cai, O. Painter, and K. J. Vahala, "Observation of critical coupling in a fiber taper to a silica-microsphere whispering-gallery mode system," *Physical Review Letters*, vol. 85, pp. 74-7, 2000.

[59] M. Cai and K. Vahala, "Highly efficient optical power transfer to whispering-gallery modes by use of a symmetrical dual-coupling configuration," *Optics Letters*, vol. 25, pp. 260-2, 2000.

[60] S. M. Spillane, T. J. Kippenberg, O. J. Painter, and K. J. Vahala, "Ideality in a fiber-taper-coupled microresonator system for application to cavity quantum electrodynamics," *Physical Review Letters*, vol. 91, pp. 043902/1-4, 2003.

[61] M. Borselli, T. J. Johnson, and O. Painter, "Beyond the Rayleigh scattering limit in high-Q silicon microdisks: theory and experiment," *Optics Express, vol.13, no.5, 7 March 2005*.

[62] W. M. J. Green, R. K. Lee, G. A. DeRose, A. Scherer, and A. Yariv, "Hybrid InGaAsP-InP Mach-Zehnder racetrack resonator for thermooptic switching and coupling control," *Optics Express, vol.13, no.5, 7 March 2005*.

[63] M. C. Lee and M. C. Wu, "MEMS-actuated microdisk resonators with variable power coupling ratios," *IEEE Photonics Technology Letters*, vol. 17, pp. 1034-6, 2005.

[64] M.-C. M. Lee and M. C. Wu, "Tunable coupling regimes of silicon microdisk resonators using MEMS actuators," *Optics Express, Vol. 14, Issue 11, pp. 4703-4712*, 2006.

[65] U. Levy, K. Campbell, A. Groisman, S. Mookherjea, and Y. Fainman, "On-chip microfluidic tuning of an optical microring resonator," *Applied Physics Letters*, vol. 88, pp. 111107-1-3, 2006.

[66] M. C. Wu, O. Solgaard, and J. E. Ford, "Optical MEMS for lightwave communication," *Journal of Lightwave Technology*, vol. 24, pp. 4433-54, 2006.

[67] S.-S. Lee, L.-S. Huang, C.-J. Kim, and M. C. Wu, "Free-space fiber-optic switches based on MEMS vertical torsion mirrors," *Journal of Lightwave Technology*, vol. 17, pp. 7-13, 1999.

[68] S.-S. Lee, E. Motamedi, and M. C. Wu, "Surface-micromachined free-space fiber optic switches with integrated microactuators for optical fiber communication systems," presented at Tranducers 97. 1997 International Conference on Solid-State Sensors and Actuators. Digest of Technical Papers (Cat. No.97TH8267). IEEE. Part vol.1, 1997, pp. 85-8. New York, NY, USA.

[69] R. T. Chen, H. Nguyen, and M. C. Wu, "A high-speed low-voltage stress-induced micromachined 22 optical switch," *IEEE Photonics Technology Letters*, vol. 11, pp. 1396-8, 1999.

[70] J.-c. Tsai, S. Huang, D. Hah, and M. C. Wu, "1N² wavelength-selective switch with telescope-magnified 2D input/output fiber collimator array," presented at 2003 IEEE/LEOS International Conference on Optical MEMS (Cat. No.03EX682). IEEE. 2003, pp. 45-6. Piscataway, NJ, USA.

[71] C. H. Chi, J. Tsai, M. C. Lee, D. Hah, and M. C. Wu, "Integrated 1x4 wavelength-selective switch with on-chip MEMS micromirrors," presented at 2005 Quantum Electronics and Laser Science Conference (QELS) (IEEE Cat. No. 05CH37696). IEEE. Part vol. 3, 2005, pp. 1732-4 vol. 3. Piscataway, NJ, USA.

[72] C.-H. Chi, J. Yao, J.-c. Tsai, M. C. Wu, and K. Okamoto, "Compact 18 MEMS optical switches using planar lightwave circuits," presented at Optical Fiber Communication Conference (OFC) (IEEE Cat. No.04CH37532). Opt. Soc. America. Part vol.2, 2004, pp. 3. Washington, DC, USA.

[73] K. E. Petersen, "Silicon as a mechanical material," *Proceedings of the IEEE*, vol. 70, pp. 420-57, 1982.

[74] M. Fujino, P. R. Patterson, H. Nguyen, W. Piyawattanametha, and M. C. Wu, "Monolithically cascaded micromirror pair driven by angular vertical combs for two-axis scanning," *IEEE Journal of Selected Topics in Quantum Electronics*, vol. 10, pp. 492-7, 2004.

[75] W. Piyawattanametha, P. R. Patterson, H. Dooyoung, H. Toshiyoshi, and M. C. Wu, "A 2D scanner by surface and bulk micromachined vertical comb actuators," presented at 2003 IEEE/LEOS International Conference on Optical MEMS (Cat. No.03EX682). IEEE. 2003, pp. 93-4. Piscataway, NJ, USA.

[76] W. Piyawattanametha, P. R. Patterson, G. D. J. Su, H. Toshiyoshi, and M. C. Wu, "A MEMS non-interferometric differential confocal scanning optical microscope," presented at TRANSDUCERS '01. EUROSENSORS XV. 11th International Conference on Solid-State Sensors and Actuators. Digest of Technical Papers. Springer-Verlag. Part vol.1, 2001, pp. 590-3. Berlin, Germany.

[77] M. W. Pruessner, D. Kelly, M. Datta, H. Lim, R. Maboudian, and R. Ghodssi, "Design and fabrication of an InP-based moving waveguide 1 x 2 optical MEMS switch," presented at 2003 International Semiconductor Device Research Symposium (IEEE Cat. No.03EX741). IEEE. 2003, pp. 280-1. Piscataway, NJ, USA.

[78] T. Bakke, C. P. Tigges, and C. T. Sullivan, "1 x 2 MOEMS switch based on silicon-on-insulator and polymeric waveguides," *Electronics Letters*, vol. 38, pp. 177-8, 2002.

[79] M. Matsuhara and A. Watanabe, "Coupling of curved transmission lines, and application to optical directional couplers," *Journal of the Optical Society of America*, vol. 65, pp. 163-8, 1975.

[80] L. Rayleigh, "The Problem of the Whispering Gallery," *Phil. Mag.*, vol. 20, pp. 1001-1004, 1910.

[81] L. Rayleigh, "Further Applications of Bessel's Functions of High Order to the Whispering Gallery and Allied Problems," *Phil. Mag.*, vol. 27, pp. 100-109, 1914.

[82] M. Gastine, L. Courtois, and J. L. Dormann, "Electromagnetic resonances of free dielectric spheres," *IEEE Transactions on Microwave Theory and Techniques*, vol. MTT-15, pp. 694-700, 1967.

[83] P. Affolter and B. Eliasson, "Electromagnetic resonances and Q-factors of lossy dielectric spheres," *IEEE Transactions on Microwave Theory and Techniques*, vol. MMT-21, pp. 573-8, 1973.

[84] C. G. B. Garrett, W. Kaiser, and W. L. Bond, "Stimulated Emission into Optical Whispering Modes of Spheres," *Physical Review*, vol. 124, pp. 1807-1809, 1961.

[85] P. Debye, "Der Lichtdruck auf Kugeln von beliebigem Material," *Ann. Physik*, vol. 30, pp. 57-136, 1909.

[86] J. R. Wait, "Electromagnetic whispering gallery modes in a dielectric rod," *Radio Science*, vol. 2, pp. 1005-1017, 1967.

[87] R. P. Wang and M. M. Dumitrescu, "Theory of optical modes in semiconductor microdisk lasers," *Journal of Applied Physics*, vol. 81, pp. 3391-7, 1997.

[88] A. W. Snyder and J. D. Love, "Optical waveguide theory," *Chapman & Hall. 1983*.

[89] S. C. Hagness, D. Rafizadeh, S. T. Ho, and A. Taflove, "FDTD microcavity simulations: design and experimental realization of waveguide-coupled single-mode ring and whispering-gallery-mode disk resonators," *Journal of Lightwave Technology*, vol. 15, pp. 2154-65, 1997.

[90] "http://www.rsoftdesign.com/products/component_design/BeamPROP/."

[91] K. K. Svidzinskiy, "Silicon-based optical integrated circuits for terabit-rate optical networks," presented at Elsevier. Microelectronic Engineering, vol.69, no.2-4, Sept. 2003, pp. 221-7. Netherlands.

[92] E. A. J. Marcatili, "Dielectric rectangular waveguide and directional coupler for integrated optics," *Bell System Technical Journal*, vol. 48, pp. 2071-102, 1969.

[93] D. V. Armani, T. J. Kippenberg, S. M. Spillane, and K. J. Vahala, "Ultra-high-Q toroid microcavity on a chip," *Nature*, vol. 421, pp. 925-8, 2003.

[94] M. L. Gorodetsky, A. A. Savchenkov, and V. S. Ilchenko, "Ultimate Q of optical microsphere resonators," *Optics Letters*, vol. 21, pp. 453-5, 1996.

[95] R. A. Soref and B. R. Bennett, "Electrooptical effects in silicon," *IEEE Journal of Quantum Electronics*, vol. QE-23, pp. 123-9, 1987.

[96] E. A. J. Marcatili, "Bends in optical dielectric guides," *Bell System Technical Journal*, vol. 48, pp. 2103-32, 1969.

[97] H. K. Tsang, C. S. Wong, T. K. Liang, I. E. Day, S. W. Roberts, A. Harpin, J. Drake, and M. Asghari, "Optical dispersion, two-photon absorption and self-phase modulation in silicon waveguides at 1.5 mum wavelength," *Applied Physics Letters*, vol. 80, pp. 416-18, 2002.

[98] M. C. Lee and M. C. Wu, "A MEMS-actuated tunable microdisk resonator," presented at 2003 IEEE/LEOS International Conference on Optical MEMS (Cat. No.03EX682). IEEE. 2003, pp.28-9. Piscataway, NJ, USA., 2003.

[99] M. C. Lee and M. C. Wu, "Vertically-coupled MEMS microdisks for tunable optical delays and dynamic dispersion compensation," presented at 2005 Conference on Lasers and Electro-Optics (CLEO) (IEEE Cat. No. 05TH8796). IEEE. Part Vol. 1, 2005, pp. 434-6 Vol. 1. Piscataway, NJ, USA., 2005.

[100] M. C. Lee and M. C. Wu, "A reconfigurable add-drop filter using MEMS-actuated microdisk resonator," presented at IEEE/LEOS Optical MEMs 2005 (IEEE Cat. No. 05EX1115). IEEE. 2005, pp. 67-8. Piscataway, NJ, USA., 2005.

[101] M. Borselli, T. J. Johnson, and O. Painter, "Measuring the role of surface chemistry in silicon microphotonics," *Applied Physics Letters*, vol. 88, pp. 131114-1-3, 2006.

[102] Y. J. Wang, X. L. Cheng, Z. L. Lin, F. Gao, and F. Zhang, "Monolithic beam splitter in silicon-on-insulator," *Optics Express*, vol. 13, pp. 5154-5159, 2004.

[103] P. B. W. Bogaerts, and R. Baets, "Scattering at sidewall roughness in photonic crystal slabs," *Optics Letters*, vol. 28, pp. 689-91, 2003.

[104] L. V. F. Grillot, S. Laval, D. Pascal, and E. Cassan, "Size influence on the propagation loss induced by sidewall roughness in ultrasmall SOI waveguides," *IEEE Photonics Technology Letters*, vol. 16, pp. 1661-3, 2004.

[105] P. K. Tien, "Light waves in thin films and integrated optics," *Applied Optics*, vol. 10, pp. 2395-13, 1971.

[106] M.-C. M. Lee, "Tunable Optical Microresonators Using Micro-Electro-Mechanical-System (MEMS) Technology," in *Electrical Engineering*, vol. PhD. Los Angels: UCLA, 2005.

[107] S. J. McNab, N. Moll, and Y. A. Vlasov, "Ultra-low loss photonic integrated circuit with membrane-type photonic crystal waveguides," *Optics Express, vol.11, no.22, 3 Nov. 2003*.

[108] J. Arentoft, T. Sondergaard, M. Kristensen, A. Boltasseva, M. Thorhauge, and L. Frandsen, "Low-loss silicon-on-insulator photonic crystal waveguides," *Electronics Letters*, vol. 38, pp. 274-5, 2002.

[109] K. K. Lee, D. R. Lim, L. C. Kimerling, J. Shin, and F. Cerrina, "Fabrication of ultralow-loss Si/SiO₂ waveguides by roughness reduction," *Optics Letters*, vol. 26, pp. 1888-90, 2001.

[110] Y. Kato, H. Takao, K. Sawada, and M. Ishida, "Improvement of metal-oxide semiconductor interface characteristics in complementary metal-oxide semiconductor on Si(111) by combination of fluorine implantation and long-time hydrogen annealing," *Japanese Journal of Applied Physics, Part 2 (Letters)*, vol. 45, pp. L108-10, 2006.

[111] Y. Kato, H. Takao, K. Sawada, and M. Ishida, "The characteristic improvement of Si (111) metal-oxide-semiconductor field-effect transistor by long-time hydrogen annealing," *Japanese Journal of Applied Physics, Part 1 (Regular Papers, Short Notes & Review Papers)*, vol. 43, pp. 6848-53, 2004.

[112] P. Hokyung, M. S. Rahman, C. Man, L. Byoung Hun, C. Rino, C. D. Young, and H. Hyunsang, "Improved interface quality and charge-trapping characteristics of MOSFETs with high-kappa gate dielectric," *IEEE Electron Device Letters*, vol. 26, pp. 725-7, 2005.

[113] J.-S. Lee, Y.-K. Choi, D. Ha, S. Balasubramanian, T.-J. King, and J. Bokor, "Hydrogen annealing effect on DC and low-frequency noise characteristics in CMOS FinFETs," *IEEE Electron Device Letters*, vol. 24, pp. 186-8, 2003.

[114] J. Nara, T. Sasaki, and T. Ohno, "Theory of adsorption and diffusion of Si adatoms on H/Si(100) stepped surface," presented at Elsevier. Journal of Crystal Growth, vol.201-202, May 1999, pp. 77-80. Netherlands., 1999.

[115] S. Jeong and A. Oshiyama, "Complex diffusion mechanisms of a silicon adatom on hydrogenated Si(100) surfaces: on terraces and near steps," presented at Elsevier. Surface Science, vol.433-435, 2 Aug. 1999, pp. 481-5. Netherlands.

[116] H. Moriceau, A. M. Cartier, and B. Aspar, "Hydrogen annealing treatment used to obtain high quality SOI surfaces," presented at 1998 IEEE International SOI

Conference Proceedings (Cat No.98CH36199). IEEE. 1998, pp. 37-8. New York, NY, USA., 1998.

[117] N. Sato and T. Yonehara, "Hydrogen annealed silicon-on-insulator," *Applied Physics Letters*, vol. 65, pp. 1924-6, 1994.

[118] W. W. Mullins, "Theory of thermal grooving," *Journal of Applied Physics*, vol. 28, pp. 333-339, 1957.

[119] Z. R. Xu and R. B. McLellan, "Observation of hydrogen-enhanced thermal grooving," *Scripta Materialia*, vol. 39, pp. 365-9, 1998.

[120] S.-G. Kim, T. M. Roh, J. Kim, I. Y. Park, J. W. Lee, J. G. Koo, I.-H. Bae, and K. I. Cho, "Behavior of trench surface by H₂ annealing for reliable trench gate oxide," *Journal of Crystal Growth*, vol. 255, pp. 123-9, 2003.

[121] S. Matsuda, T. Sato, H. Yoshimura, Y. Takegawa, A. Sudo, I. Mizushima, Y. Tsunashima, and Y. Toyoshima, "Novel corner rounding process for shallow trench isolation utilizing MSTS (Micro-Structure Transformation of Silicon)," presented at International Electron Devices Meeting 1998. Technical Digest (Cat. No.98CH36217). IEEE. 1998, pp. 137-40. Piscataway, NJ, USA., 1998.

[122] T. Sato, N. Aoki, I. Mizushima, and Y. Tsunashima, "A new substrate engineering for the formation of empty space in silicon (ESS) induced by silicon surface migration," presented at International Electron Devices Meeting 1999. Technical Digest (Cat. No.99CH36318). IEEE. 1999, pp. 517-20. Piscataway, NJ, USA., 1999.

[123] H. Kuribayashi, R. Hiruta, R. Shimizu, K. Sudoh, and H. Iwasaki, "Shape transformation of silicon trenches during hydrogen annealing," *Journal of Vacuum Science & Technology A (Vacuum, Surfaces, and Films)*, vol. 21, pp. 1279-83, 2003.

[124] H. Kuribayashi, R. Hiruta, R. Shimizu, K. Sudoh, and H. Iwasaki, "Investigation of shape transformation of silicon trenches during hydrogen annealing," *Japanese Journal of Applied Physics, Part 2 (Letters)*, vol. 43, pp. L468-70, 2004.

[125] M. M. Lee, J. Yao, and M. C. Wu, "Silicon profile transformation and sidewall roughness reduction using hydrogen annealing," presented at 18th IEEE International Conference on Micro Electro Mechanical Systems (IEEE Cat. No.05CH37610). IEEE. 2005, pp. 596-9. Piscataway, NJ, USA., 2005.

[126] M.-C. Lee and M. C. Wu, "3D Silicon Transformation using Hydrogen Annealing," presented at Solid-State Sensor, Actuator, Microsystem Workshop 2004, Hilton Head, 2004.

[127] M. C. Lee and M. C. Wu, "Thermal annealing in hydrogen for 3-D profile transformation on silicon-on-insulator and sidewall roughness reduction," *Journal of Microelectromechanical Systems*, vol. 15, pp. 338-43, 2006.

[128] M. Delfino and T. A. Reifsteck, "Laser activated flow of phosphosilicate glass in integrated circuit devices," *IEEE Electron Device Letters*, vol. EDL-3, pp. 116-18, 1982.

[129] P. Jeuch, J. P. Joly, and J. M. Hode, "P-glass reflow with a tunable CO₂ laser," presented at Laser and Electron Beam Interactions with Solids. Proceedings of the Materials Research Society Annual Meeting. North-Holland. 1982, pp. 603-8. Amsterdam, Netherlands., 1982.

[130] A. Berthold, B. Jakoby, and M. J. Vellekoop, "Wafer-to-wafer fusion bonding of oxidized silicon to silicon at low temperatures," presented at Elsevier. Sensors & Actuators A-Physical, vol.A68, no.1-3, 15 June 1998, pp.410-13. Switzerland.

[131] D. Daly, R. F. Stevens, M. C. Hutley, and N. Davies, "The manufacture of microlenses by melting photoresist," *Measurement Science & Technology*, vol. 1, pp. 759-66, 1990.

[132] H. Yang, C.-K. Chao, C.-P. Lin, and S.-C. Shen, "Micro-ball lens array modeling and fabrication using thermal reflow in two polymer layers," *Journal of Micromechanics and Microengineering*, vol. 14, pp. 277-82, 2004.

[133] H. Yang, C.-K. Chao, M.-K. Wei, and C.-P. Lin, "High fill-factor microlens array mold insert fabrication using a thermal reflow process," *Journal of Micromechanics and Microengineering*, vol. 14, pp. 1197-204, 2004.

[134] E. Perozziello, "http://www.lelandstanfordjunior.com/thermaloxide.html."

[135] J. Yao, M. C. Lee, D. Leuenberger, and M. C. Wu, "Silicon Microtoroidal Resonators with Integrated MEMS Tunable Optical Coupler," presented at IEEE Optical Micro-Electro-Mechanical-System,MA7, Big Sky MT, USA, 2006.

[136] L. Martinez and M. lipson, "High confinement suspended micro-ring resonators in silicon-on-insulator," *Optics Express*, vol. 14, pp. 6259-6263, 2006.

[137] J. Yao, M. C. Lee, D. Leuenberger, and M. C. Wu, "Wavelength- and bandwidth-tunable filters based on MEMS-actuated microdisk resonators," presented at OFCNFOEC 2006. 2006 Optical Fiber Communication Conference and National Fiber Optic Engineers Conference. IEEE. 2006, pp. 3. Piscataway, NJ, USA.

[138] M. C. Lee, S. Mathai, and M. C. Wu, "Dynamic dispersion compensator using MEMS-actuated microdisk resonators," presented at Conference on Lasers and Electro-Optics (CLEO). IEEE. Part vol.2, 2004, pp.3 pp. vol.2. Piscataway, NJ, USA., 2004.

[139] T. J. Kippenberg, S. M. Spillane, and K. J. Vahala, "Kerr-nonlinearity optical parametric oscillation in an ultrahigh-Q toroid microcavity," *Physical Review Letters*, vol. 93, pp. 083904/1-4, 2004.

[140] I. M. White, N. M. Hanumegowda, and X. Fan, "Subfemtomole detection of small molecules with microsphere sensors," *Optics Letters*, vol. 30, pp. 3189-91, 2005.

[141] M. Weisser, G. Tovar, S. Mittler Neher, W. Knoll, F. Brosinger, H. Freimuth, M. Lacher, and W. Ehrfeld, "Specific bio-recognition reactions observed with an integrated Mach-Zehnder interferometer," *Biosensors & Bioelectronics*, vol. 14, pp. 405-11, 1999.

[142] M. W. Foster, D. J. Ferrel, and R. A. Lieberman, "Surface plasmon resonance biosensor miniaturization," presented at Proceedings of the SPIE - The International Society for Optical Engineering, vol.2293, 1994, pp. 122-31. USA.

[143] X. Dong, P. Shum, N. Q. Ngo, C. Zhao, J. Yang, and C. C. Chan, "A bandwidth-tunable FBG filter with fixed center wavelength," *Microwave and Optical Technology Letters*, vol. 41, pp. 22-8, 2004.

[144] Q. Yu, P. Zhongqi, Y. Lian-Shan, and A. E. Willner, "Chromatic dispersion monitoring technique using sideband optical filtering and clock phase-shift detection," *Journal of Lightwave Technology*, vol. 20, pp. 2267-71, 2002.

[145] J. A. McCaulley, T. V. M. Donnelly, M. Vernon, and I. Taha, "Temperature dependence of the near-infrared refractive index of silicon, gallium arsenide, and indium phosphide," *Physical Review B-Condensed Matter*, vol. 49, pp. 7408-17, 1994.

[146] B. Zhang, D. Leuenberger, M.-C. M. Lee, S. Hu, M. Haghi, A. E. Willner, and M. C. Wu, "Error-Free Data Transmission Through a Tunable-Bandwidth Filter Based on MEMS-actuated Microdisk Resonator," presented at CLEO 2006, Long Beach, CA, USA, 2006.

[147] I. Moerman, G. Vermeire, M. D'Hondt, W. Vanderbauwhede, J. Blondelle, G. Coudenys, P. Van Daele, and P. Demeester, "III-V semiconductor waveguiding devices using adiabatic tapers," *Microelectronics Journal*, vol. 25, pp. 675-90, 1994.

[148] K. Kasaya, O. Mitomi, M. Naganuma, Y. Kondo, and Y. Noguchi, "A simple laterally tapered waveguide for low-loss coupling to single-mode fibers," *IEEE Photonics Technology Letters*, vol. 5, pp. 345-7, 1993.

[149] V. R. Almeida, R. R. Panepucci, and M. Lipson, "Nanotaper for compact mode conversion," *Optics Letters*, vol. 28, pp. 1302-4, 2003.

[150] E. Goutain, J. C. Renaud, M. Krakowski, D. Rondi, R. Blondeau, and D. Decoster, "30 GHz bandwidth, 1.55 μm MQW-DFB laser diode based on a new modulation scheme," *Electronics Letters*, vol. 32, pp. 896, 1996.